



Measurement of the differential cross section for top quark pair production in pp collisions at $\sqrt{s} = 8$ TeV

The CMS Collaboration*

Abstract

The normalized differential cross section for top quark pair ($t\bar{t}$) production is measured in pp collisions at a centre-of-mass energy of 8 TeV at the CERN LHC using the CMS detector in data corresponding to an integrated luminosity of 19.7 fb^{-1} . The measurements are performed in the lepton+jets (e/μ +jets) and in the dilepton (e^+e^- , $\mu^+\mu^-$, and $e^\pm\mu^\mp$) decay channels. The $t\bar{t}$ cross section is measured as a function of the kinematic properties of the charged leptons, the jets associated to b quarks, the top quarks, and the $t\bar{t}$ system. The data are compared with several predictions from perturbative QCD up to approximate next-to-next-to-leading-order precision. No significant deviations are observed relative to the standard model predictions.

Published in the European Physical Journal C as doi:10.1140/epjc/s10052-015-3709-x.

arXiv:1505.04480v2 [hep-ex] 25 Nov 2015

1 Introduction

Understanding the production and properties of top quarks is fundamental for testing the quality of the standard model (SM) and for searching for new physical phenomena beyond its scope. The large top quark data samples produced in proton-proton (pp) collisions at the CERN LHC provide access to precision measurements that are crucial for checking the internal consistency of the SM at the LHC energy scale. In particular, measurements of the top quark pair ($t\bar{t}$) production cross section as a function of $t\bar{t}$ kinematic observables are important for comparing with the state-of-the-art quantum chromodynamic (QCD) predictions within the SM, and thereby constrain QCD parameters. In addition, the top quark plays a relevant role in theories beyond the SM, and such differential measurements are therefore expected to be sensitive to new phenomena [1].

Differential $t\bar{t}$ production cross sections have been measured previously at the Fermilab $p\bar{p}$ Tevatron [2, 3], and at the LHC at a centre-of-mass energy $\sqrt{s} = 7$ TeV [4–6]. We present here the first measurement of the normalized differential $t\bar{t}$ production cross section with the CMS detector at $\sqrt{s} = 8$ TeV. The analysis uses data recorded in 2012 corresponding to an integrated luminosity of $19.7 \pm 0.5 \text{ fb}^{-1}$, which is about a factor of four larger than the sample used in the measurement performed by the CMS Collaboration at 7 TeV [5]. The analysis largely follows the procedures of Ref. [5] and benefits from the increase in statistical precision together with improvements in kinematic reconstruction algorithms and extended systematic studies, leading to a significant reduction of the total uncertainties.

The measurements are performed in ℓ +jets channels ($\ell = e$ or μ), which contain a single isolated charged lepton and at least four jets in the final state, and in dilepton channels, with two oppositely charged leptons (e^+e^- , $\mu^+\mu^-$, $e^\pm\mu^\mp$) and at least two jets. The $t\bar{t}$ cross section is determined as a function of the kinematic properties of the top quarks and of the $t\bar{t}$ system, as well as of the leptons and jets associated with bottom (b) quarks (b jets) from top quark decays.

The kinematic properties of top quarks are obtained through kinematic-fitting and reconstruction algorithms. The normalized differential $t\bar{t}$ cross section is determined by counting the number of $t\bar{t}$ signal events in each bin of a given observable, correcting for detector effects and acceptance, and dividing by the measured total inclusive $t\bar{t}$ event rate. The latter is evaluated by integrating over all bins in each observable.

The results for directly measured quantities, such as kinematic properties of leptons and b jets, are presented in a fiducial phase space defined by the kinematic and geometric acceptance of all selected final-state objects. This avoids extrapolating the measured cross section into regions that are not experimentally accessible. In addition, the top quark and $t\bar{t}$ distributions are determined in the full phase space, in order to facilitate the comparison with higher-order perturbative QCD calculations. The results are compared to several predictions obtained with the leading-order (LO) MADGRAPH [7] generator interfaced to PYTHIA [8] for parton evolution and hadronization, the next-to-leading-order (NLO) generators POWHEG [9–11], interfaced to both PYTHIA and HERWIG [12], and MC@NLO [13] interfaced to HERWIG, and the latest NLO calculations with next-to-next-to-leading-logarithm (NNLL) corrections [14, 15], and approximate next-to-next-to-leading-order (NNLO) predictions [16]. The approximate NNLO predictions can be computed with the DIFFTOP [17] program.

This document is structured as follows. A brief description of the CMS detector is provided in Section 2. Details of the event simulation are given in Section 3, and event reconstruction and selection are discussed in Section 4. The estimated systematic uncertainties on the measurements of the cross section are described in Section 5. The results of the measurement are

discussed in Section 6, followed by a summary in Section 7.

2 CMS detector

The central feature of the CMS apparatus is a superconducting solenoid of 13 m length and 6 m inner diameter, which provides an axial magnetic field of 3.8 T. Within the field volume are a silicon-pixel and strip tracker, a lead tungstate crystal electromagnetic calorimeter (ECAL), and a brass and scintillator hadron calorimeter (HCAL), each composed of a barrel and two endcap sections. Charged particle trajectories are measured by the inner tracking system, covering a pseudorapidity range of $|\eta| < 2.5$. The ECAL and the HCAL surround the tracking volume, providing high-resolution energy and direction measurements of electrons, photons, and hadronic jets up to $|\eta| < 3$. Muons are measured in gas-ionization detectors embedded in the steel flux return yoke outside the solenoid covering the region $|\eta| < 2.4$. Extensive forward calorimetry complements the coverage provided by the barrel and endcap detectors up to $|\eta| < 5.2$. The detector is nearly hermetic, allowing for energy balance measurements in the plane transverse to the beam directions. A two-tier trigger system selects the pp collisions for use in the analysis. A more detailed description of the CMS detector, together with a definition of the coordinate system and the relevant kinematic variables, can be found in Ref. [18].

3 Event simulation and theoretical calculations

Event generators, interfaced with a detailed detector simulation, are used to model experimental effects, such as consequences of event reconstruction and choice of selection criteria, as well as detector resolution. The $t\bar{t}$ sample is simulated using the LO MADGRAPH event generator (v. 5.1.5.11), which implements the relevant matrix elements with up to three additional partons. The MADSPIN [19] package is used to incorporate spin correlation effects with matrix elements for up to three additional partons. The value of the top quark mass is fixed to $m_t = 172.5$ GeV and the proton structure is described by the parton distribution functions (PDF) CTEQ6L1 [20]. The generated events are subsequently processed with PYTHIA (v. 6.426, referred to as PYTHIA6 in the following) for parton showering and hadronization, and the MLM prescription [21] is used for matching of matrix-element jets to parton showers. The CMS detector response is simulated using GEANT4 (v. 9.4) [22].

In addition to the MADGRAPH prediction, calculations obtained with the NLO generators MC@NLO (v. 3.41) and POWHEG (v. 1.0 r1380) are compared to the results presented in Section 6. While POWHEG and MC@NLO are formally equivalent up to the NLO accuracy, they differ in the techniques used to avoid double counting of radiative corrections that can arise from interfacing with the parton showering generators. Two POWHEG samples are used: one is processed through PYTHIA6 and the other through HERWIG (v. 6.520, referred to as HERWIG6 in the following) for the subsequent parton showering and hadronization. The parton showering in PYTHIA6 is based on a transverse-momentum-ordered evolution scale, whereas in HERWIG6 it is angular-ordered. The events generated with MC@NLO are interfaced with HERWIG6. The HERWIG6 AUET2 tune [23] is used to model the underlying event in the POWHEG+HERWIG6 sample, while the default tune is used in the MC@NLO+HERWIG6 sample. The proton structure is described by the PDF sets CT10 [24] and CTEQ6M [20] for POWHEG and MC@NLO, respectively. In addition, the latest available NLO+NNLL [14, 15] and approximate NNLO QCD predictions [16] are also used to compare with the data. The NNLO MSTW2008 [25] PDF set is used for both the NLO+NNLL and the approximate NNLO calculations.

Standard model background samples are simulated with MADGRAPH (without the MADSPIN

package), POWHEG, or PYTHIA6, depending on the process. The main background contributions originate from the production of W and Z/γ^* bosons with additional jets (referred to as W +jets and Z +jets, respectively, in the following), single top quark (s -, t -, and tW channels), diboson (WW , WZ , and ZZ), $t\bar{t}$ production in association with a Z , W , or γ boson (referred to as $t\bar{t} + Z/W/\gamma$ in the following), and QCD multijet events. The W +jets, Z +jets, and $t\bar{t} + Z/W/\gamma$ samples are simulated with MADGRAPH with up to two additional partons in the final state. The POWHEG generator is used for simulating single top quark production, while PYTHIA6 is used to simulate diboson and QCD multijet events. Parton showering and hadronization are also simulated with PYTHIA6 in all the background samples. The PYTHIA6 Z2* tune [26] is used to characterize the underlying event in both the $t\bar{t}$ and the background samples.

For comparison with the measured distributions, the event yields in the simulated samples are normalized to an integrated luminosity of 19.7 fb^{-1} , according to their predicted cross sections. These are taken from NNLO (W +jets [27, 28] and Z +jets [27]), NLO+NNLL (single top quark s -, t -, and tW channels [16]), NLO (diboson [29], $t\bar{t} + W$ [30], and $t\bar{t} + Z$ [31]), and LO (QCD multijet [8]) calculations. The predicted cross section for the $t\bar{t} + \gamma$ sample is obtained by scaling the LO cross section obtained with the WHIZARD event generator [32] by an NLO/LO correction K -factor [33]. Correction factors described in Sections 4 and 5, and subsequently referred to as scale factors, are applied when needed to improve the description of the data by the simulation. The $t\bar{t}$ simulation is normalized to the data to present the expected rates in the figures in Section 4.

4 Event reconstruction and selection

The event selection is similar to that described in Ref. [5] for the measurement of normalized differential $t\bar{t}$ cross sections at $\sqrt{s} = 7 \text{ TeV}$, and is based on the final-state topology of $t\bar{t}$ events. The top quark decays almost exclusively into a W boson and a b quark, and only the subsequent decays of one or two of the W bosons into a charged lepton (electron or muon) and a neutrino are considered. These signatures imply the presence of isolated leptons with high transverse momentum p_T , large p_T imbalance caused by the neutrinos that escape detection, and highly energetic jets. The identification of b jets through b -tagging techniques is used to increase the purity of the selected sample. The event selection in each channel is optimized to maximize the content of $t\bar{t}$ signal events and background rejection.

4.1 Lepton, jet, and missing transverse energy reconstruction

Events are reconstructed using a particle-flow technique [34, 35], which combines signals from all subdetectors to enhance the reconstruction and identification of individual particles observed in pp collisions. Charged hadrons from pileup events, i.e. those originating from additional pp interactions within the same bunch crossing, are subtracted on an event-by-event basis. Subsequently, the remaining neutral-hadron component from pileup is accounted for through jet energy corrections [36].

Electron candidates are reconstructed from a combination of the track momentum at the main interaction vertex, the corresponding energy deposition in the ECAL, and the energy sum of all bremsstrahlung photons attached to the track [37]. The candidates are required to have $p_T > 33 \text{ GeV}$ within the pseudorapidity interval $|\eta| < 2.1$ for the ℓ +jets channels, while electron candidates in the dilepton channels are required to have $p_T > 20 \text{ GeV}$ and $|\eta| < 2.4$. As an additional quality criterion, a relative isolation $I_{\text{rel}}(0.3) < 0.10$ in the ℓ +jets channels and $I_{\text{rel}}(0.3) < 0.15$ in the dilepton channels is required, where $I_{\text{rel}}(x)$ is defined as the sum of the p_T of all neutral and charged reconstructed particle candidates inside a cone of $\Delta R \equiv$

$\sqrt{(\Delta\eta)^2 + (\Delta\phi)^2} < x$ around the electron (excluding the electron itself) in η - ϕ space, divided by the p_T of the electron.

Muon candidates are reconstructed using the track information from the silicon tracker and the muon system. They are required to have $p_T > 33$ GeV and $|\eta| < 2.1$ in the ℓ +jets channels, while in the dilepton channels the corresponding selection requires $p_T > 20$ GeV and $|\eta| < 2.4$. Isolated muon candidates are selected if they fulfill $I_{\text{rel}}(0.4) < 0.12$ and $I_{\text{rel}}(0.3) < 0.15$ in the ℓ +jets and dilepton channels, respectively. The same definition of relative isolation described above is also used for muon candidates.

Jets are reconstructed by clustering the particle-flow candidates [38] using the anti- k_T clustering algorithm with a distance parameter of $R = 0.5$ [39]. Electrons and muons passing less stringent selections on lepton kinematic quantities and isolation, relative to the ones specified above, are identified but excluded from clustering. A jet is selected if it has $p_T > 30$ GeV and $|\eta| < 2.4$ for both the ℓ +jets and dilepton channels. Jets originating from b quarks are identified through a ‘‘combined secondary vertex’’ algorithm [40], which provides a b-tagging discriminant by combining secondary vertices and track-based lifetime information. The chosen working point in the ℓ +jets channels has an efficiency for tagging a b jet of $\approx 60\%$, while the probability to misidentify light-flavour jets as b jets (mistag rate) is only $\approx 1.5\%$. In the dilepton channels, the working point is selected to provide b-tagging efficiency and mistag rate of ≈ 80 – 85% and $\approx 10\%$, respectively [40]. These requirements are chosen to reduce the background contribution in the corresponding channels while keeping a large fraction of the $t\bar{t}$ signal.

The missing transverse energy \cancel{E}_T is defined as the magnitude of the imbalance in the transverse momentum $\vec{\cancel{p}}_T$ in the event, which is the negative of the vectorial sum of the momenta in the transverse plane of all the particles reconstructed with the particle-flow algorithm [41]. To mitigate the effect of contributions from pileup on the resolution in \cancel{E}_T , we use a multivariate correction where the input is separated into components that originate from the primary and other collision vertices [42]. This correction improves the \cancel{E}_T resolution by $\approx 5\%$.

4.2 Event selection

Events in the ℓ +jets channels that are triggered by the presence of a single electron (muon) with $p_T > 27$ GeV ($p_T > 24$ GeV, $|\eta| < 2.1$), are selected if they contain exactly one reconstructed lepton fulfilling the requirements described in Section 4.1. Events are rejected if there are additional electron candidates with $p_T > 20$ GeV, $|\eta| < 2.5$, and $I_{\text{rel}}(0.3) < 0.15$, or additional muon candidates with $p_T > 10$ GeV, $|\eta| < 2.5$, and $I_{\text{rel}}(0.4) < 0.2$. Additionally, an event must contain at least four reconstructed jets satisfying the criteria described in Section 4.1. To suppress background contribution mainly from W +jets events, at least two of these jets are required to be tagged as b jets, and at least two must not be tagged as b jets, as they are used to reconstruct $W \rightarrow q\bar{q}'$ decays. In the dilepton channels, events are triggered using combinations of two leptons with p_T thresholds of 8 and 17 GeV, and are selected if they contain at least two isolated leptons of opposite electric charge and at least two jets. At least one of the jets is required to be b-tagged. In events with more than two leptons, we choose the lepton pair with opposite charge and largest value in the sum of their scalar p_T . Events with an invariant mass of the lepton pair smaller than 20 GeV are removed to suppress events from decays of heavy-flavour resonances and low-mass Drell–Yan processes. Backgrounds from Z +jets processes in the e^+e^- and $\mu^+\mu^-$ channels are also suppressed by requiring the dilepton invariant mass to be outside a Z boson mass window of 91 ± 15 GeV, and to have $\cancel{E}_T > 40$ GeV.

After these selection steps, several basic distributions in ℓ +jets and dilepton events are shown in Figs. 1 and 2, respectively. The hatched regions correspond to the shape uncertainties for the

signal and background (cf. Section 5), and are dominated by the former. The data are reasonably well described by the simulation, as shown in the lower part of each plot, where the ratio of data to simulation is presented to better indicate the level of agreement between data and the default $t\bar{t}$ signal (MADGRAPH+PYTHIA6) and background samples used in the analysis. For both channels, however, data tend to have lower p_T values than predicted by the simulation. It has been verified that the results presented in Section 6 are not affected by these remaining differences between data and simulation. A better data-to-simulation agreement in the lepton and jet p_T distributions is obtained by scaling the top quark p_T spectrum in simulation to match the data. However, the impact on the measurement of the cross sections is negligible.

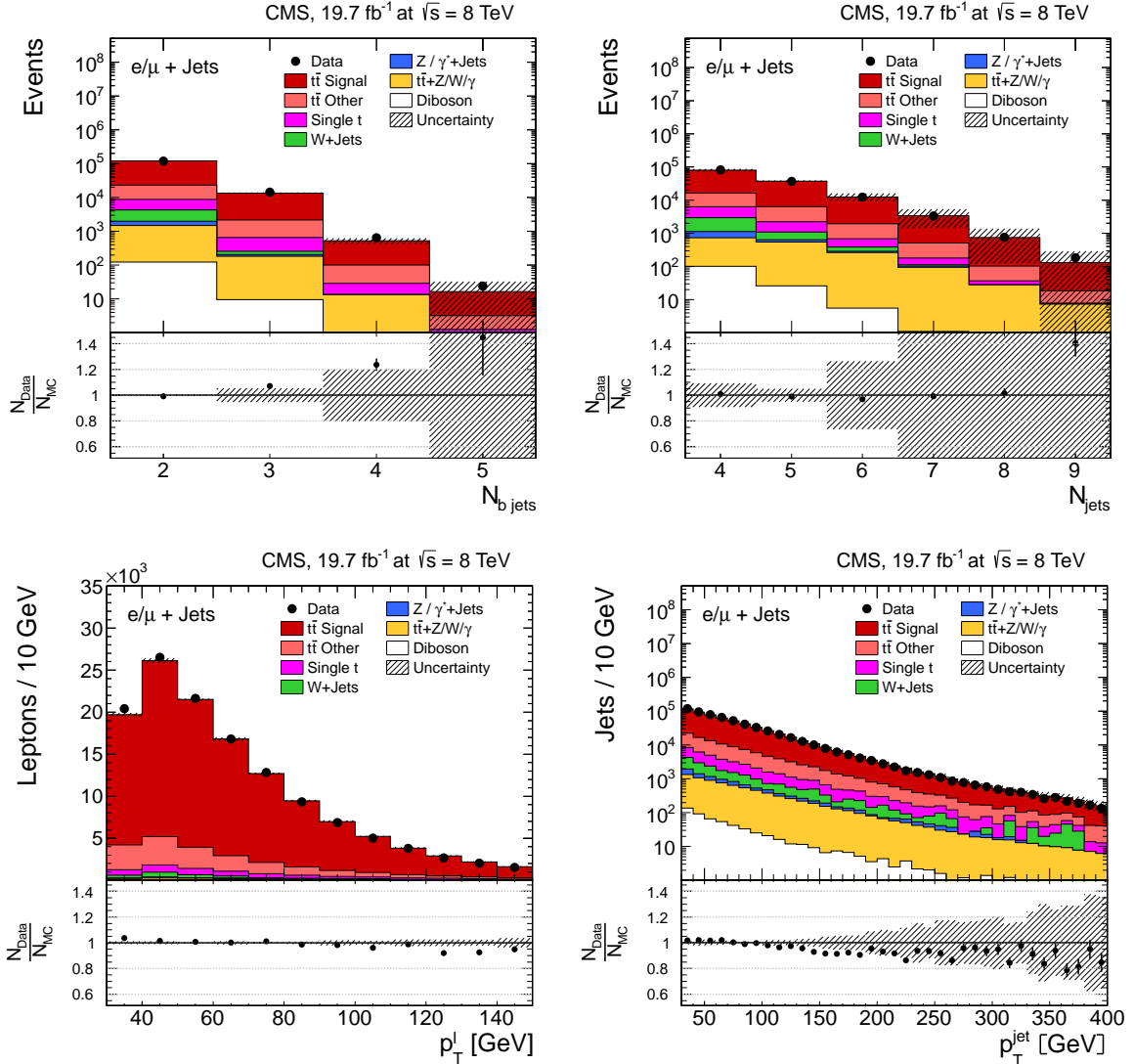


Figure 1: Kinematic distributions after event selection and before the kinematic reconstruction of the $t\bar{t}$ system in the ℓ +jets channels: the multiplicity in the reconstructed number of b-tagged jets (top left), the multiplicity in the reconstructed number of jets (top right), the p_T of the selected isolated leptons (bottom left), and the p_T of all reconstructed jets (bottom right). The QCD multijet background is negligible and not shown. The hatched regions correspond to the shape uncertainties for the signal and backgrounds (cf. Section 5). The lower part of each plot shows the ratio of data to the predictions.

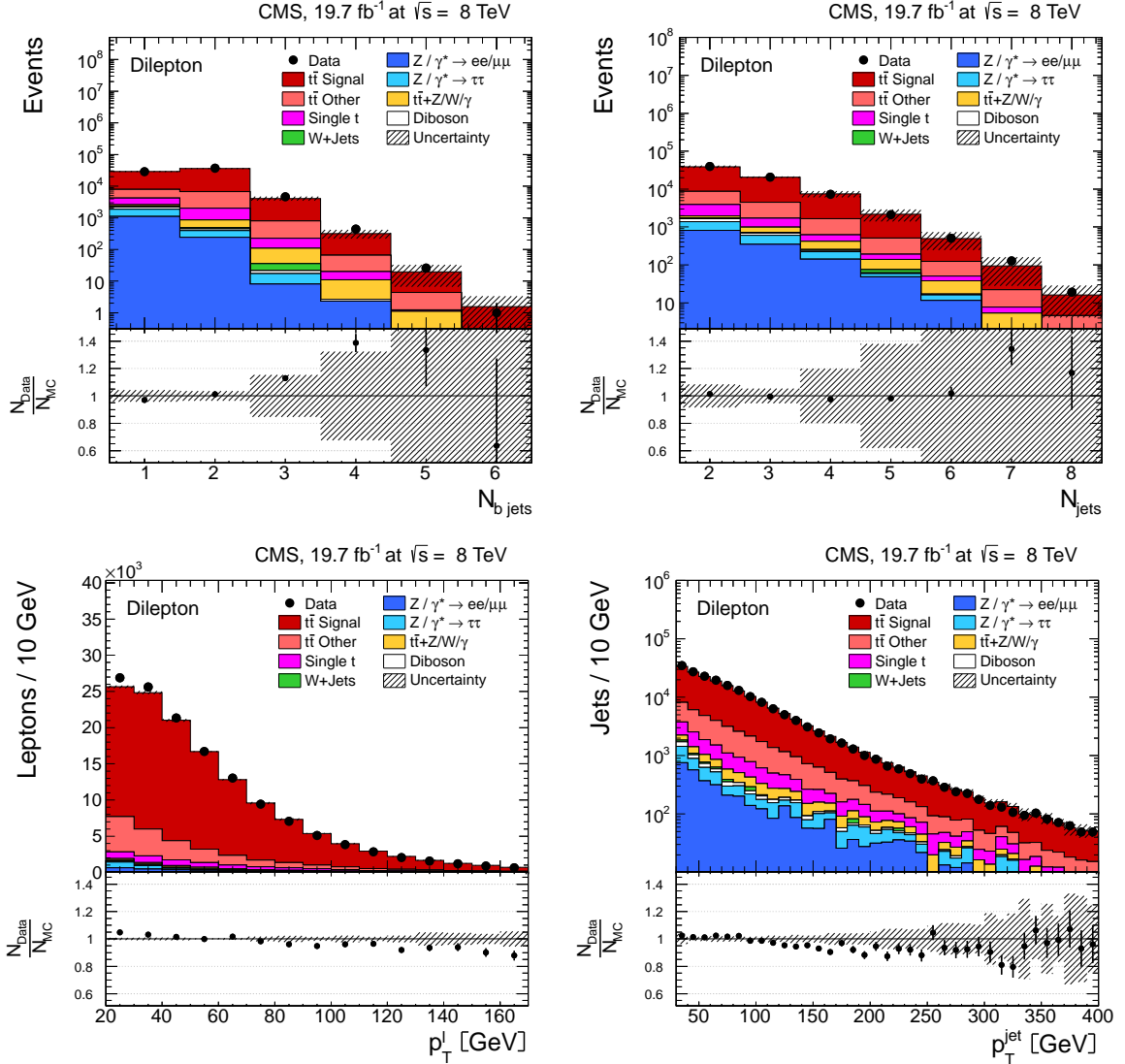


Figure 2: Kinematic distributions after event selection and before the kinematic reconstruction of the $t\bar{t}$ system for the dilepton channels: the multiplicity in the reconstructed number of b -tagged jets (top left), the multiplicity in the number of reconstructed jets (top right), the p_T of the selected isolated leptons (bottom left), and the p_T of the reconstructed jets (bottom right). The QCD multijet background is negligible and not shown. The Z/γ^* +jets background is determined from data [5, 43]. The hatched regions correspond to the shape uncertainties for the signal and backgrounds (cf. Section 5). The lower part of each plot shows the ratio of data to the predictions.

4.3 Kinematic reconstruction of the $t\bar{t}$ system

The kinematic properties of the top quark pair are determined from the four-momenta of all final-state objects through kinematic reconstruction algorithms. These algorithms are improved versions of those described in Ref. [5].

In the ℓ +jets channels, a constrained kinematic fitting algorithm is applied [5, 44] to the four-momenta of the selected lepton and up to five leading jets, and the \cancel{p}_T representing the transverse momentum of the neutrino, which are changed according to their resolutions. The fit is constrained to reconstruct two W bosons, each with a mass of 80.4 GeV. In addition, the reconstructed top quark and antiquark masses are required to be equal. To reduce the number of permutations in the association of jets to quarks, only b-tagged jets are considered as b quarks, and only untagged jets are considered as light quarks. In events with several combinatorial solutions, only the one with the minimum χ^2 in the fit is accepted. The main improvement relative to the method described in Ref. [5] is the increase in the number of correct assignments of b jets to b quarks. This is achieved by applying the kinematic fit twice, sequentially, in each event. In the first fit, the top quark mass is fixed to a value of 172.5 GeV. The jet combination that provides the minimum χ^2 in the fit is then used as input to the second kinematic fit, in which the top quark mass is not fixed, and the solution to this fit is retained. A further improvement in the method is to require the χ^2 -probability of the second kinematic fit to be $>2\%$. This criterion is chosen to optimize the fraction of correctly reconstructed signal events, without increasing significantly the statistical uncertainty in the data. The efficiency of this requirement is about 87% for signal events with the correct jet assignment. As a result, the number of correctly reconstructed events is increased by almost a factor of two relative to the method used in Ref. [5], and effects from migration of events across bins, which are relevant for the measurements of the cross section, are reduced. It has been checked that any possible bias in the results that could be introduced by fixing the top quark mass to a specific value in the first kinematic fit is within the assigned systematic uncertainty on the dependence of the measurement on the top quark mass (cf. Section 5.2).

The dilepton channels use an algebraic kinematic reconstruction method [5, 45]. The only unknowns are the three-momenta of the two neutrinos, which are reconstructed imposing the following kinematic constraints: p_T conservation in the event; the W bosons, and top quark and antiquark masses. In contrast to the method of Ref. [5], the top quark mass is fixed to a value of 172.5 GeV. Each suitable pair of b jet candidates in the event, and both possible assignments of these two jets to the two selected leptons, are considered in the kinematic reconstruction. Combinations with two b-tagged jets are preferred to using single b-tagged jets. In the new method, events are reconstructed 100 times, each time randomly smearing the measured energies and directions of the reconstructed lepton and b jet candidates by their respective detector resolutions. This smearing recovers events that yielded no solution of the equations for the neutrino momenta, because of measurement fluctuations. The equations for the neutrino momenta can have up to four solutions. For a given smearing, the solution is identified by the one yielding the smallest invariant mass of the $t\bar{t}$ system. For each solution, a weight is calculated based on the expected true lepton-b-jet invariant mass spectrum. The weights are summed over the 100 reconstruction attempts, and the kinematic quantities associated to the top quark and antiquark are calculated as a weighted average. Finally, the two jet and lepton-jet assignments that yield the maximum sum of weights are chosen for analysis. It has been checked that any bias introduced through the use of the lepton-b-jet and $t\bar{t}$ invariant masses is negligible. This method yields on average a reconstruction efficiency of $\approx 94\%$, which is 6% higher than the one described in Ref. [5], and reduces systematic migration effects.

Distributions of the top quark or antiquark and $t\bar{t}$ kinematic observables (the transverse momenta p_T^t , $p_T^{\bar{t}}$, and the rapidities y_t and $y_{\bar{t}}$) are presented in Figs. 3 and 4 for the ℓ +jets and dilepton channels, respectively. The hatched regions correspond to the shape uncertainties for the signal and background (cf. Section 5), and are dominated by the former. The lower panel in each plot also shows the ratio of data relative to the simulated signal and background samples.

In general, the data are reasonably well described by the simulation within the uncertainties. For both channels, the measured p_T distributions, in particular p_T^t , are somewhat softer than the simulated distributions: the data lie above the simulation for $p_T^t < 60(65)$ GeV in the ℓ +jets (dilepton) channels, while they lie below for $p_T^t > 200$ GeV. This pattern was also observed at 7 TeV [5]. To ensure that the results presented in Section 6 are not affected by such small remaining differences between data and simulation, the analysis has been repeated in different kinematic regions, with different selection requirements, and after scaling the top quark p_T spectrum in simulation to match the data. However, the impact on the measurement of the cross sections is negligible.

Following the event selection described in Section 4.2 and the kinematic reconstruction of the $t\bar{t}$ system, the main contributions to the background in the ℓ +jets channels arise from $t\bar{t}$ decays into channel other than ℓ +jets (including $t\bar{t}$ decays into τ leptons originating from the primary interaction) and single top quark events. The contribution from W+jets and QCD multijet events are well suppressed after the b-tagging requirement, while other $t\bar{t}$ events are somewhat reduced after the χ^2 -probability requirement. A total of 24 927 events are found in the e+jets channel and 26 843 events in the μ +jets channel. The contribution from $t\bar{t}$ signal to the final event sample is 89.0%. The remaining fraction of events contains 7.3% $t\bar{t}$ decays other than the ℓ +jets channels, 2.4% single top quark events, 0.9% W+jets and $t\bar{t} + Z/W/\gamma$ events, and negligible fractions of Z+jets, diboson, and QCD multijet events. All background contributions are determined from simulation.

In the dilepton channels, 10 678 events are found in the e^+e^- channel, 14 403 in the $\mu^+\mu^-$ channel, and 39 640 in the $e^\pm\mu^\mp$ channel. Only $t\bar{t}$ events containing at least two leptons (electrons or muons) from W decays in the final state are considered as signal, and constitute 79.0% of the final event sample. All other $t\bar{t}$ candidate events, specifically those originating from decays via τ leptons, are considered as background and amount to 13.3% of the final event sample. The fraction of Z+jets events is found to be 2.4%. This background, which is dominant to the e^+e^- and $\mu^+\mu^-$ channels, is estimated from data using the number of events observed within the Z-peak region (which is removed from the candidate sample), and a correction needed for non-Z+jets backgrounds in this same control region is obtained from data in the $e^\pm\mu^\mp$ channel [5, 43]. Other sources of background, including single top quark production (3.4%), $t\bar{t} + Z/W/\gamma$ production (1%), the contribution arising from misidentified or genuine leptons within jets (0.6%), or diboson events (0.3%), are estimated from simulation.

5 Systematic uncertainties

The measurement is affected by systematic uncertainties that originate from detector effects and from theoretical assumptions. Each source of systematic uncertainty is assessed individually by changing the corresponding efficiency, resolution, or scale by its uncertainty, using a prescription similar to the one followed in Ref. [5]. For each change made, the measured normalized differential cross section is recalculated, and the difference of the changed result relative to its nominal value in each bin is taken as the systematic uncertainty. The overall uncertainty on the measurement is obtained by adding all the contributions in quadrature, and is

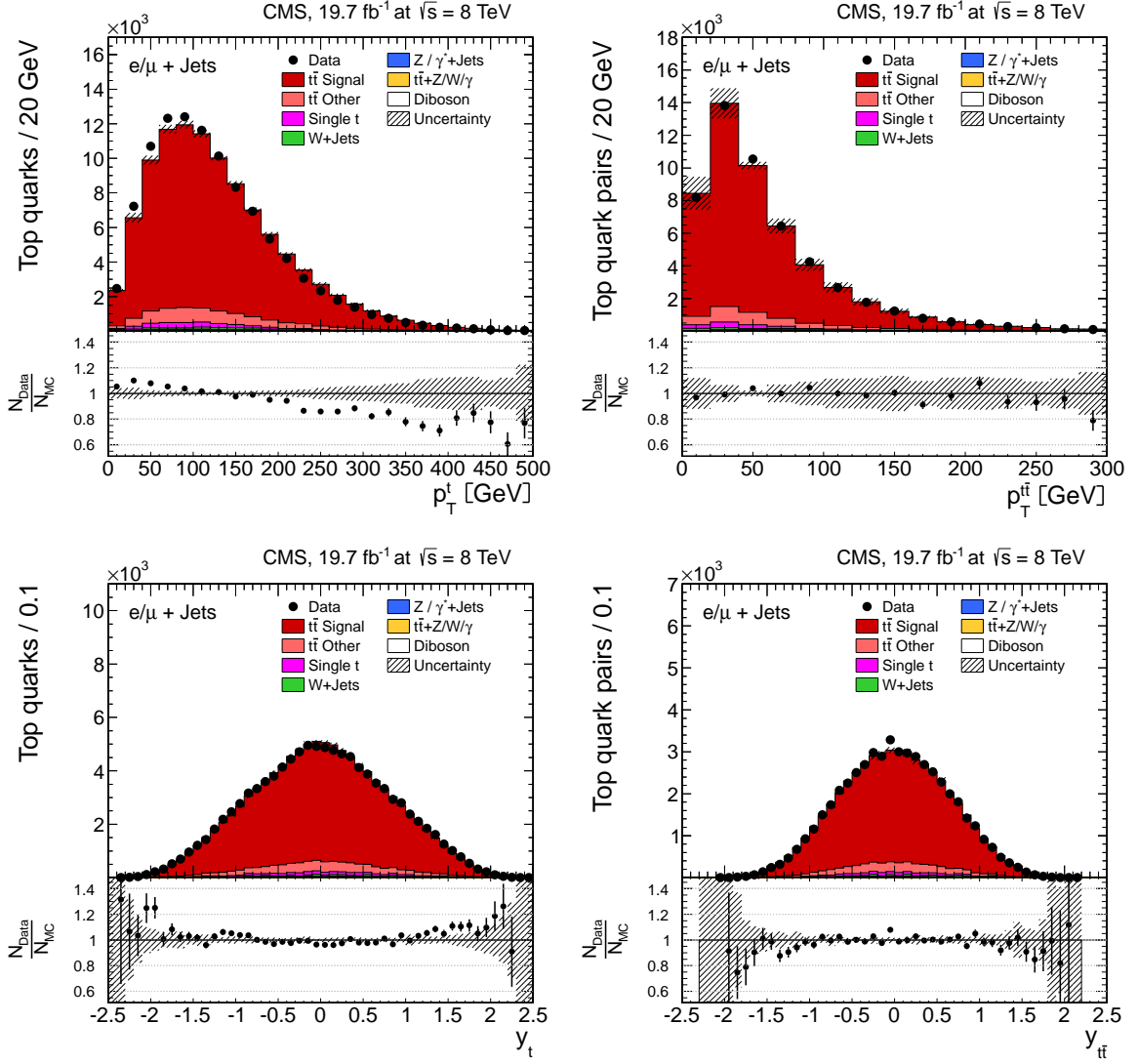


Figure 3: Distribution of top quark or antiquark (left) and $t\bar{t}$ (right) quantities as obtained from the kinematic reconstruction in the ℓ +jets channels. The top row shows the p_T , and the bottom row shows the rapidities. The QCD multijet background is negligible and not shown. The hatched regions correspond to the shape uncertainties for the signal and backgrounds (cf. Section 5). The lower part of each plot shows the ratio of data to the predictions.

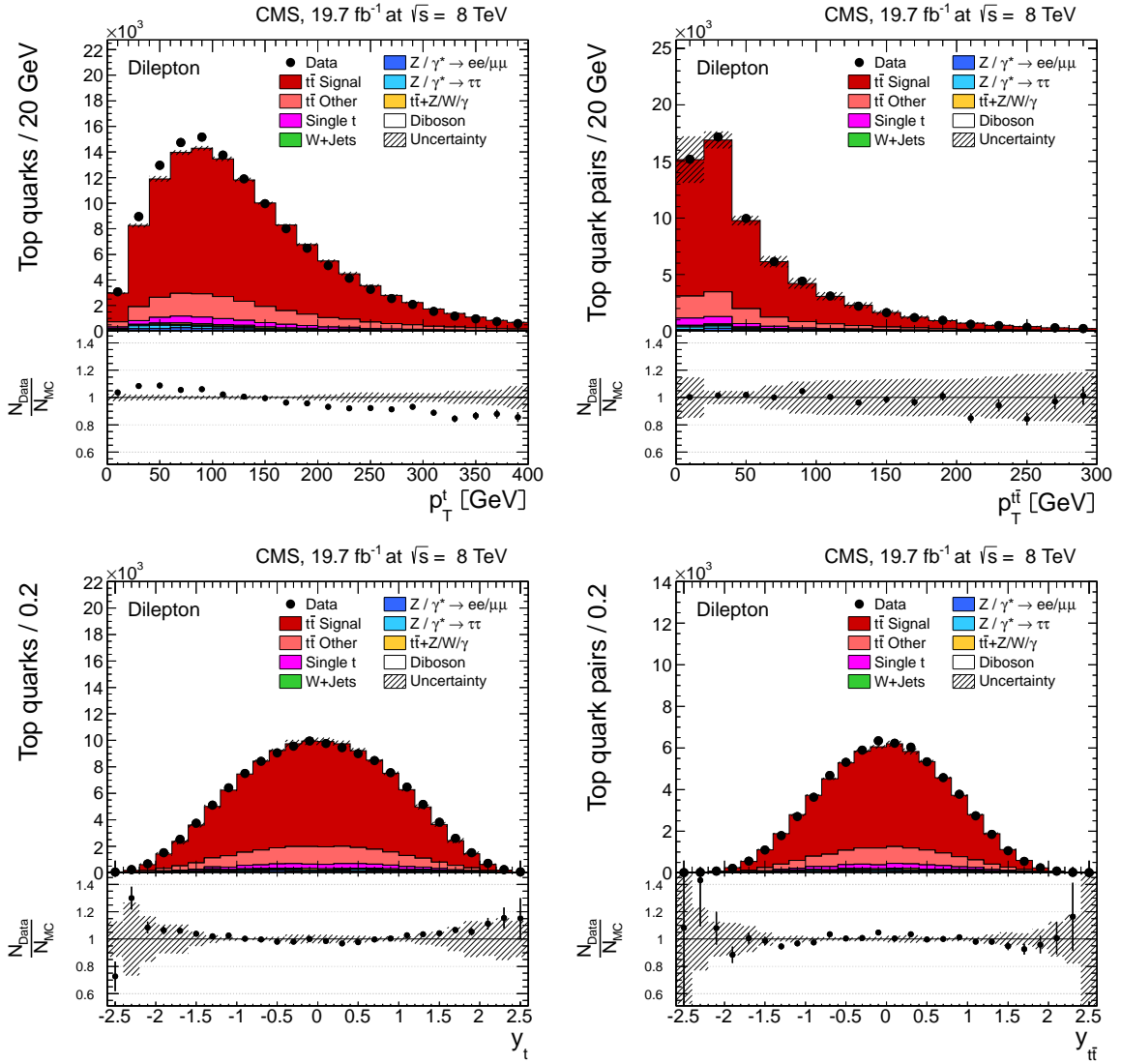


Figure 4: Distribution of top quark or antiquark (left) and $t\bar{t}$ (right) quantities as obtained from the kinematic reconstruction in the dilepton channels. The top row shows the p_T , and the bottom row shows the rapidities. The QCD multijet background is negligible and not shown. The Z/γ^* +jets background is determined from data [5, 43]. The hatched regions correspond to the shape uncertainties for the signal and backgrounds (cf. Section 5). The lower part of each plot shows the ratio of data to the predictions.

of the order of 3–10%, depending on the observable and the bin. A detailed description of this is given in Sections 5.1 and 5.2. The typical representative values of the systematic uncertainties in the normalized differential cross sections are summarized in Table 1.

5.1 Experimental uncertainties

The efficiencies of the single-electron and single-muon triggers in the ℓ +jets channels are determined using the “tag-and-probe” method of Ref. [46] using Z boson event samples. Scale factors close to unity within a few percent are extracted to account for the observed dependence on the η and p_T of the lepton. The lepton identification and isolation efficiencies for the ℓ +jets channels obtained with the tag-and-probe method agree well between data and simulation, so that the applied corrections are very close to unity. The systematic uncertainties are determined by shape-dependent changes in trigger and selection efficiencies by their uncertainties. Lepton trigger efficiencies in the dilepton channels are measured using triggers that are only weakly correlated to the dilepton triggers used in the analysis. A dependence on η of a few percent is observed, and scale factors are extracted. The lepton identification and isolation uncertainties in the dilepton channels are also determined using the tag-and-probe method, and are again found to be described very well by the simulation for both electrons and muons. The overall difference between data and simulation in bins of η and p_T is estimated to be $<2\%$ for electrons, and scale factors for muons are found to be close to unity within 1.0%.

The uncertainty due to the limited knowledge of the jet energy scale is determined by changes implemented in jet energy in bins of p_T and η [38]. The uncertainty due to the limited accuracy of the jet energy resolution (JER) is determined by changing the simulated JER by $\pm 1\sigma$ in different η regions [38].

The uncertainty in b-tagging efficiency is determined by taking the maximum change in the shape of p_T and η b jet distributions obtained by changing the scale factors. This is achieved by dividing the b jet distributions in p_T and η into two bins at the median of the respective distributions. These correspond to $p_T = 65$ GeV, and $|\eta| = 0.7$ and 0.75 for the ℓ +jets and dilepton channels, respectively. The b-tagging scale factors for b jets in the first bin are scaled up by half of the uncertainties quoted in Ref. [40], while those in the second bin are scaled down, and vice versa, so that a maximum variation is assumed and the difference between the scale factors in the two bins reflects the full uncertainty. The changes are made separately in the p_T and η distributions, and independently for heavy-flavour (b and c) and light (s, u, d, and gluon) jets, assuming that they are all uncorrelated.

The uncertainty in background normalization is determined by changing the background yields. In the ℓ +jets channels, the background normalization for the diboson, QCD multijet, W+jets, and Z+jets samples is conservatively varied by $\pm 50\%$ [5], since these backgrounds, being very small, are determined from simulation rather than from data. The normalization of the $t\bar{t}$ +Z/W/ γ samples is changed by $\pm 30\%$. For the single top quark sample, the uncertainty is covered by changing the normalization by $\pm 30\%$, and the kinematic scales of the event process (renormalization and factorization scales) as described in Section 5.2. In the e^+e^- and $\mu^+\mu^-$ channels, the dominant background from Z+jets determined from data [5, 43] is changed in normalization by $\pm 30\%$. In addition, changes in the background contributions from single top quark, diboson, QCD multijet, $t\bar{t}$ +Z/W/ γ , and W+jets events of $\pm 30\%$ are used in dilepton channels [5].

The kinematic reconstruction of top quarks is well described by the simulation, and the resulting uncertainties are small. In the case of the ℓ +jets analysis, the uncertainty of the kinematic fit is included in the changes in jet energy scales and resolutions, and in the uncertainty on the

dependence on the top quark mass (cf. Section 5.2). In the dilepton analysis, the bin-to-bin uncertainty is determined from the small remaining difference in efficiency between simulation and data.

The pileup model estimates the mean number of additional pp interactions to be about 20 events per bunch crossing for the analyzed data. This estimate is based on the total inelastic proton-proton cross section, which is determined to be 69.4 mb following the measurement described in Ref. [47]. The systematic uncertainty is determined by changing this cross section within its uncertainty of $\pm 5\%$.

5.2 Uncertainties in modelling

The impact of theoretical assumptions on the measurement is determined, as indicated previously, by repeating the analysis and replacing the standard MADGRAPH $t\bar{t}$ simulation by dedicated simulation samples with altered parameters.

The uncertainty in modelling of the hard-production process is assessed through changes in the renormalization and factorization scales in the MADGRAPH sample by factors of two and 0.5 relative to their common nominal value, which is set to the Q of the hard process. In MADGRAPH, Q is defined by $Q^2 = m_t^2 + \Sigma p_T^2$, where the sum is over all additional final state partons in the matrix element. The impact of the choice of the scale that separates the description of jet production through matrix elements (ME) or parton shower (PS) in MADGRAPH is studied by changing its reference value of 20 GeV to 40 GeV and to 10 GeV. In the ℓ +jets channels, changes in the renormalization and factorization scales are also applied to single top quark events to determine an uncertainty on the shape of this background contribution. The dependence of the measurement on the top quark mass is also estimated from dedicated MADGRAPH simulation samples in which the top quark mass is changed by ± 1 GeV relative to the value used in the default simulation. The uncertainty from hadronization and parton showering is assessed by comparing the results obtained from samples simulated with POWHEG and MC@NLO interfaced with PYTHIA6 and HERWIG6, respectively. The uncertainty from the choice of PDF is determined by reweighting the sample of simulated $t\bar{t}$ signal events according to the 52 CT10 PDF error sets [24], at a 90% confidence level. The maximum variation is taken as uncertainty. As mentioned in Sections 4.2 and 4.3, the effect of scaling the top quark p_T spectrum in simulation to match the data has negligible impact on the measured cross sections, therefore no systematic uncertainty is taken into account for this effect.

6 Normalized differential cross sections

The normalized $t\bar{t}$ cross section in each bin i of each observable X is determined as a function of the kinematic properties of the leptons, the lepton pair, the b jets, the b jet system, the top quarks, and the $t\bar{t}$ system through the relation [5]:

$$\frac{1}{\sigma} \frac{d\sigma_i}{dX} = \frac{1}{\sum_i x_i} \frac{x_i}{\Delta_i^X} \quad (1)$$

where x_i represents the number of signal events measured in data in bin i after background subtraction and corrected for detector efficiencies, acceptances, and migrations, and Δ_i^X is the bin width. The differential cross section is normalized by the sum of x_i over all bins, as indicated in Eq. (1). The integrated luminosity is omitted, as it cancels in the ratio. Because of the normalization, sources of systematic uncertainty that are correlated across all bins of the measurement, e.g. the uncertainty in the integrated luminosity, also cancel. The contribution to the

Table 1: Breakdown of typical systematic uncertainties for the normalized differential cross sections. The uncertainty in the jet-parton matching threshold is indicated as “ME-PS threshold”; “PS” refers to “parton shower”. The medians of the distribution of uncertainties over all bins of the measurement are quoted. For the ℓ +jets channels, the background from Z+jets is negligible and included in the “Background (all other)” category.

Source	Relative systematic uncertainty (%)			
	Lepton and b jet observables		Top quark and $t\bar{t}$ observables	
	ℓ +jets	dileptons	ℓ +jets	dileptons
Trigger eff. & lepton selec.	0.1	0.1	0.1	0.1
Jet energy scale	2.3	0.4	1.6	0.8
Jet energy resolution	0.4	0.2	0.5	0.3
Background (Z+jets)	—	0.2	—	0.1
Background (all other)	0.9	0.4	0.7	0.4
b tagging	0.7	0.1	0.6	0.2
Kinematic reconstruction	—	<0.1	—	<0.1
Pileup	0.2	0.1	0.3	0.1
Fact./renorm. scale	1.1	0.7	1.8	1.2
ME-PS threshold	0.8	0.5	1.3	0.8
Hadronization & PS	2.7	1.4	1.9	1.1
Top quark mass	1.5	0.6	1.0	0.7
PDF choice	0.1	0.2	0.1	0.5

background from other $t\bar{t}$ decays is taken into account, after subtracting all other background components, by correcting the number of signal events in data using the expected signal fraction. The expected signal fraction is defined as the ratio of the number of selected $t\bar{t}$ signal events to the total number of selected $t\bar{t}$ events (i.e. signal and all other $t\bar{t}$ events) in simulation. This procedure avoids the dependence on the total inclusive $t\bar{t}$ cross section used in the normalization of the simulated signal sample.

Effects from trigger and detector efficiencies and resolutions leading to the migration of events across bin boundaries, and therefore to statistical correlations among neighbouring bins, are corrected by using a regularized unfolding method [5, 48, 49]. For each measured distribution, a response matrix is defined that accounts for migrations and efficiencies using the simulated MADGRAPH+PYTHIA6 $t\bar{t}$ signal sample. The generalized inverse of the response matrix is used to obtain the unfolded distribution from the measured distribution by applying a χ^2 minimization technique. A smoothing prescription (regularization) is applied to prevent large unphysical fluctuations that can be introduced when directly inverting the response matrix. The strength of the regularization is determined and optimized individually for each distribution using the averaged global correlation method [50]. To keep the bin-to-bin migrations small, the widths of bins in the measurement are chosen according to their purity (ratio of the number of events generated and reconstructed in a particular bin to the total number of events reconstructed in that bin; this quantity is sensitive to migrations into the bin) and stability (ratio of the number of events generated and reconstructed in a particular bin to the number of events generated in that bin; this is sensitive to migrations out of the bin). The purity and stability of the bins in this analysis are typically 60% or larger, mainly due to the improvements in the kinematic reconstruction methods discussed in Section 4.3.

The performance of the unfolding procedure is tested for possible biases from the choice of the input model (the MADGRAPH+PYTHIA6 $t\bar{t}$ signal simulation). It is verified that, either by reweighting the signal simulation or injecting a resonant $t\bar{t}$ peak into the simulation of the sig-

nal, the unfolding procedure based on the nominal response matrices still recovers these altered shapes within statistical uncertainties. Moreover, $t\bar{t}$ samples simulated with POWHEG+PYTHIA6 and MC@NLO+HERWIG6 are used to obtain the response matrices applied in the unfolding when determining the systematic uncertainties of the model (cf. Section 5.2). Therefore, possible effects from the unfolding procedure are already taken into account in the systematic uncertainties. The unfolded results are found to be consistent with those obtained using other regularization techniques [49].

The measurement of the normalized differential cross sections proceeds as follows. For each kinematic distribution, the event yields in the separate channels are added together, the background is subtracted, and the unfolding is performed. It is verified that the measurements in separate channels yield results consistent within their uncertainties. The systematic uncertainties in each bin are determined from the changes in the combined cross sections. This requires the full analysis to be repeated for every systematic change, and the difference relative to the nominal combined value is taken as the systematic uncertainty for each bin of each observable. This method therefore takes into account the correlation among systematic uncertainties in different channels and bins.

The normalized differential cross sections of leptons and b jets are unfolded to the particle level and determined in a fiducial phase space defined by the kinematic and geometric region in which the final-state leptons and jets are produced within the detector acceptance (cf. Section 6.1). This minimizes model uncertainties from the extrapolation of the measurement outside of the experimentally well-described regions of phase space. In addition, the top quark and $t\bar{t}$ -system quantities are unfolded to the parton level and presented in the full phase space (cf. Section 6.2) to provide easier comparisons with recent QCD calculations. The measurements are compared to predictions from MADGRAPH+PYTHIA6, POWHEG+PYTHIA6, POWHEG+HERWIG6, and MC@NLO+HERWIG6. The top quark and $t\bar{t}$ results are also compared to the latest calculations at NLO+NNLL [14, 15] and approximate NNLO [16] precision, when available.

In addition to the measurements discussed in Ref. [5], results for the p_T and invariant mass of the b jet pair, the p_T of the top quarks or antiquarks in the $t\bar{t}$ rest frame, the p_T of the highest (*leading*) and second-highest (*trailing*) p_T of the top quark or antiquark, and the difference in the azimuthal angle between the top quark and antiquark are also presented.

All values of normalized differential cross sections, including bin boundaries, are provided in tables in Appendix A.

6.1 Lepton and b jet differential cross sections

The normalized differential $t\bar{t}$ cross section as a function of the lepton and b jet kinematic properties is measured at the particle level, where the objects are defined as follows. Leptons from W boson decays are defined after final-state radiation. A jet is defined at the particle level, following a procedure similar to that described in Section 4.1 for reconstructed jets, by applying the anti- k_T clustering algorithm with a distance parameter of 0.5 to all stable particles (excluding the decay products from W boson decays into $e\nu$, $\mu\nu$, and final states with leptonic τ decays). A jet is defined as a b jet if it contains any of the decay products of a B hadron. Only the two b jets of highest p_T originating from different B hadrons are considered as arising from the top quark decays.

The measurements are presented in a fiducial phase space defined by geometric and kinematic requirements on these particle-level objects as follows. The charged leptons from the W boson

decays must have $|\eta| < 2.1$ and $p_T > 33$ GeV in the ℓ +jets channels, and $|\eta| < 2.4$ and $p_T > 20$ GeV in the dilepton channels. Exactly one and two leptons are required, respectively, in the ℓ +jets and the dilepton channels. At least four jets with $|\eta| < 2.4$ and $p_T > 30$ GeV, two of which are b jets, are required in the ℓ +jets channels. In the dilepton channels, both b jets from the top quark decays must satisfy $|\eta| < 2.4$ and $p_T > 30$ GeV. The fiducial particle-level corrections are determined using simulated $t\bar{t}$ events that fulfill these requirements; all other $t\bar{t}$ events are classified as background and are removed.

Figure 5 presents the normalized differential cross section in the ℓ +jets channels as a function of the lepton transverse momentum p_T^ℓ and pseudorapidity η_ℓ . The distributions of the transverse momentum of the b jets p_T^b and their pseudorapidity η_b are given in Fig. 6, together with the transverse momentum $p_T^{b\bar{b}}$ and invariant mass $m_{b\bar{b}}$ of the b jet pair. Also shown are predictions from MADGRAPH+PYTHIA6, POWHEG+PYTHIA6, POWHEG+HERWIG6, and MC@NLO+HERWIG6. The lower panel in each plot shows the ratio of each of these predictions to data, in order to quantify their level of agreement relative to data.

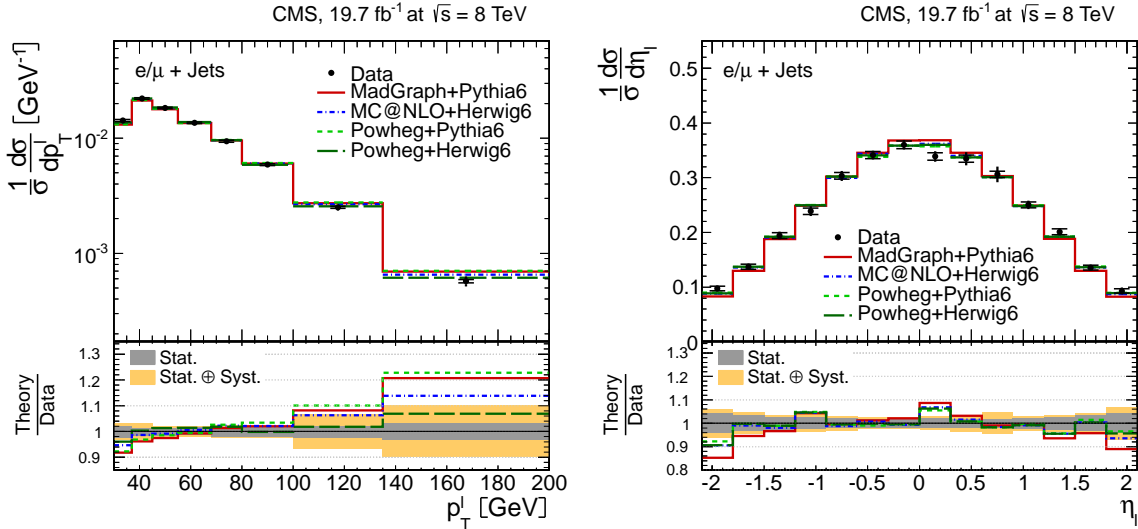


Figure 5: Normalized differential $t\bar{t}$ production cross section in the ℓ +jets channels as a function of the p_T^ℓ (left) and η_ℓ (right) of the charged lepton. The superscript ' ℓ ' refers to both ℓ^+ and ℓ^- . The data points are placed at the midpoint of the bins. The inner (outer) error bars indicate the statistical (combined statistical and systematic) uncertainties. The measurements are compared to predictions from MADGRAPH+PYTHIA6, POWHEG+PYTHIA6, POWHEG+HERWIG6, and MC@NLO+HERWIG6. The lower part of each plot shows the ratio of the predictions to data.

Figure 7 presents the normalized differential cross sections for the dilepton channels: the transverse momentum p_T^ℓ and the pseudorapidity η_ℓ of the leptons, and the transverse momentum $p_T^{\ell^+\ell^-}$ and the invariant mass $m_{\ell^+\ell^-}$ of the lepton pair. The distributions in the transverse momentum of the b jets p_T^b and their pseudorapidity η_b are shown in Fig. 8, together with the transverse momentum $p_T^{b\bar{b}}$ and invariant mass $m_{b\bar{b}}$ of the b jet pair. Predictions from MADGRAPH+PYTHIA6, POWHEG+PYTHIA6, POWHEG+HERWIG6, and MC@NLO+HERWIG6 are also presented for comparison.

In general, none of the examined predictions provides an accurate description of data for all measured lepton and b jet distributions. A steeper p_T spectrum is observed in data for the lepton and the b jet distributions compared to the predictions in both decay channels, which

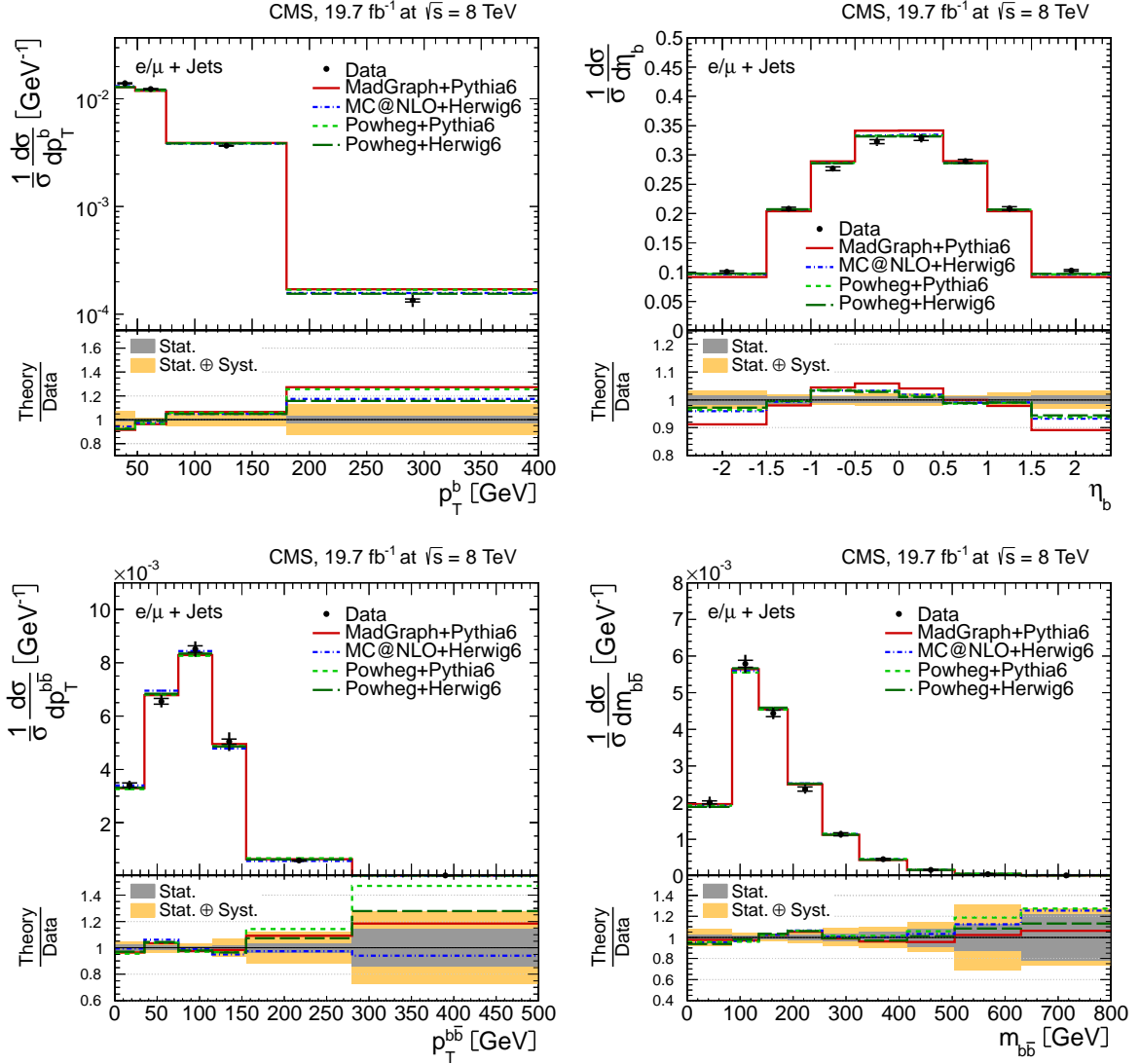


Figure 6: Normalized differential $t\bar{t}$ production cross section in the ℓ +jets channels as a function of the p_T^b (top left) and η_b (top right) of the b jets, and the $p_T^{b\bar{b}}$ (bottom left) and $m_{b\bar{b}}$ (bottom right) of the b jet pair. The superscript 'b' refers to both b and \bar{b} jets. The data points are placed at the midpoint of the bins. The inner (outer) error bars indicate the statistical (combined statistical and systematic) uncertainties. The measurements are compared to predictions from MADGRAPH+PYTHIA6, POWHEG+PYTHIA6, POWHEG+HERWIG6, and MC@NLO+HERWIG6. The lower part of each plot shows the ratio of the predictions to data.

is best described by POWHEG+HERWIG6. The lepton p_T in data is above the predictions for $p_T^\ell < 40$ GeV, while it is below for $p_T^\ell > 100$ GeV. A similar behaviour is observed for $p_T^{\ell^+\ell^-}$, p_T^b , and $p_T^{b\bar{b}}$. The $m_{\ell^+\ell^-}$ distribution in data is below all predictions for $m_{\ell^+\ell^-} > 30$ GeV. Worse agreement is found for POWHEG+PYTHIA6. The η distributions in data are described by the predictions within the experimental uncertainties. The η_b distributions are slightly less central in data than in the predictions, and are worse described by MADGRAPH+PYTHIA6. The remaining distributions are described by the predictions within experimental uncertainties.

6.2 Top quark and $t\bar{t}$ differential cross sections

The normalized differential $t\bar{t}$ cross section as a function of the kinematic properties of the top quarks and the $t\bar{t}$ system is defined with respect to the top quarks or antiquarks before the decay (parton level) and after QCD radiation, and extrapolated to the full phase space using the MADGRAPH+PYTHIA6 prediction for the ℓ +jets and dilepton channels.

In Figs. 9 to 11, the following distributions are presented for the ℓ +jets channels: the transverse momentum p_T^t and the rapidity y_t of the top quarks or antiquarks, the transverse momentum $p_T^{t^*}$ of the top quarks or antiquarks in the $t\bar{t}$ rest frame, the difference in the azimuthal angle between the top quark and antiquark $\Delta\phi(t,\bar{t})$, the transverse momentum of the leading (p_T^{t1}) and trailing (p_T^{t2}) top quark or antiquark, and the transverse momentum $p_T^{t\bar{t}}$, the rapidity $y_{t\bar{t}}$, and the invariant mass $m_{t\bar{t}}$ of the $t\bar{t}$ system. The data are compared to predictions from MADGRAPH+PYTHIA6, POWHEG+PYTHIA6, POWHEG+HERWIG6, and MC@NLO+HERWIG6. In addition, the approximate NNLO calculation [16] is also shown for the top quark p_T and rapidity results, while the $m_{t\bar{t}}$ and the $p_T^{t\bar{t}}$ distributions are compared to the NLO+NNLL predictions from Refs. [14] and [15], respectively. Figures 12–14 show the corresponding distributions in the dilepton channels. The lower panel in each plot also shows the ratio of each prediction relative to data.

In general, the POWHEG+HERWIG6 prediction provides a good description of data for all measured distributions. The shape of the top quark p_T spectrum is softer in data than in the predictions from MADGRAPH+PYTHIA6, POWHEG+PYTHIA6, and MC@NLO+HERWIG6 in both channels. The data lie above the predictions for $p_T^t < 60$ (65) GeV in the ℓ +jets (dilepton) channels, while they lie below for $p_T^t > 200$ GeV. This effect was also observed at 7 TeV [5]. The disagreement between data and predictions in the tail of the distributions is also observed in a measurement by the ATLAS Collaboration [6]. In contrast, the prediction from POWHEG+HERWIG6 and the approximate NNLO calculation provide a better description of the data, as they predict a slightly softer top quark p_T distribution than the three other simulations. The difference between the POWHEG+PYTHIA6 and POWHEG+HERWIG6 distributions is attributed to different treatment of the hardest initial state radiation in PYTHIA6 and HERWIG6. The same pattern is observed for $p_T^{t^*}$, indicating that the softer spectrum in data is not caused by the boost of the $t\bar{t}$ system. It is also present in the p_T^{t1} , and particularly, in the p_T^{t2} distributions. For all these distributions, the POWHEG+HERWIG6 prediction provides a better description of the data. The difference in the shape of the top quark p_T spectrum between data and simulation is observed consistently in the analyses using different event selection requirements or different pileup conditions. The y_t distribution is found to be slightly less central in data than in the predictions, particularly in the case of MADGRAPH+PYTHIA6 and the approximate NNLO calculation, which are more central than the other predictions. On the contrary, $y_{t\bar{t}}$ is more central in data, and it is slightly better described by MADGRAPH+PYTHIA6. The $m_{t\bar{t}}$ distribution in data tends to be lower than the predictions for large $m_{t\bar{t}}$ values, and is better described by MADGRAPH+PYTHIA6 and POWHEG+HERWIG6. The $p_T^{t\bar{t}}$ spectrum is well described by all the

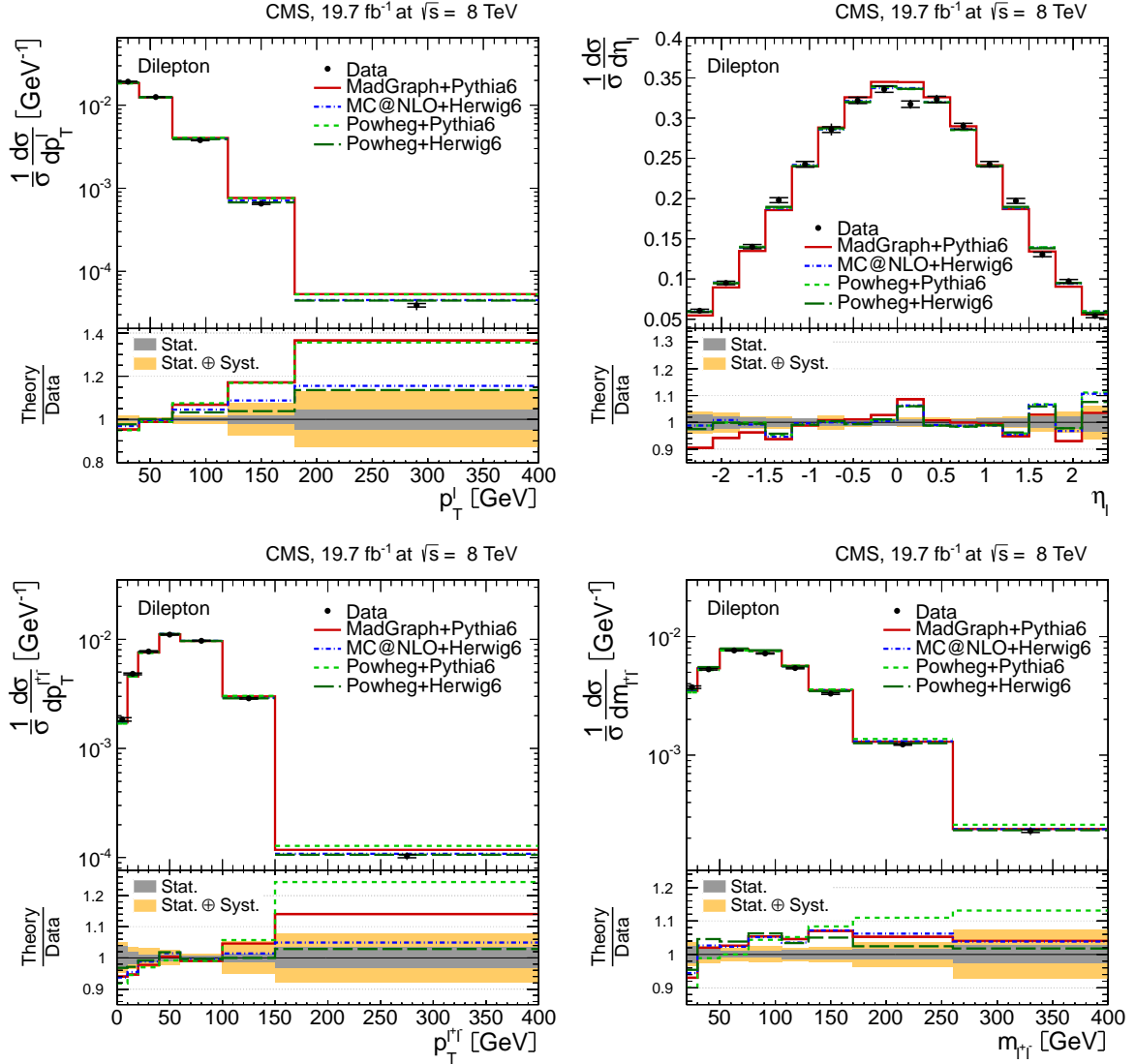


Figure 7: Normalized differential $t\bar{t}$ production cross section in the dilepton channels as a function of the p_T^ℓ (top left) and η_ℓ (top right) of the charged leptons, and the $p_T^{\ell^+\ell^-}$ (bottom left) and $m_{\ell^+\ell^-}$ (bottom right) of the lepton pair. The superscript ' ℓ ' refers to both ℓ^+ and ℓ^- . The data points are placed at the midpoint of the bins. The inner (outer) error bars indicate the statistical (combined statistical and systematic) uncertainties. The measurements are compared to predictions from MADGRAPH+PYTHIA6, POWHEG+PYTHIA6, POWHEG+HERWIG6, and MC@NLO+HERWIG6. The lower part of each plot shows the ratio of the predictions to data.

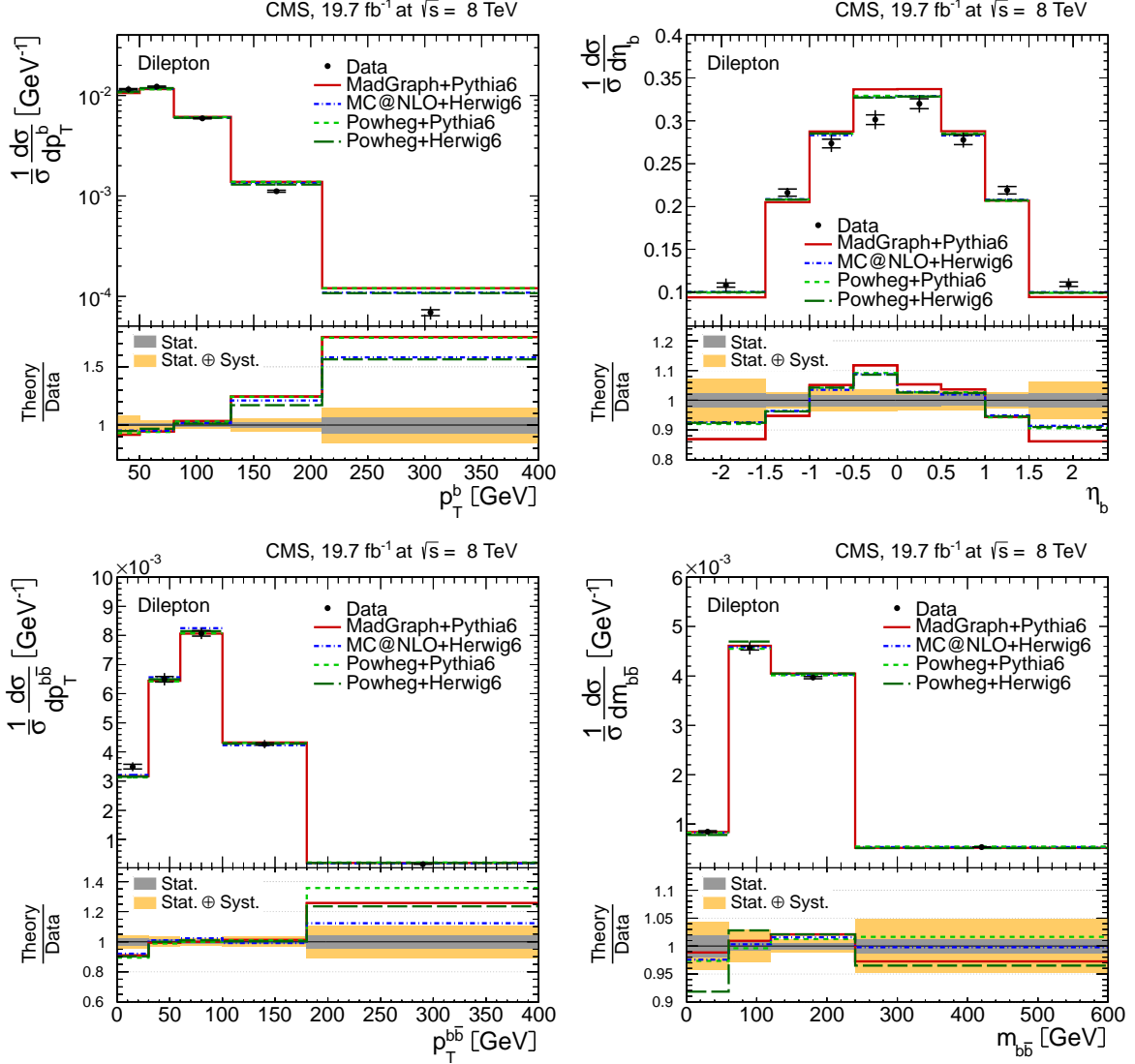


Figure 8: Normalized differential $t\bar{t}$ production cross section in the dilepton channels as a function of the p_T^b (top left) and η_b (top right) of the b jets, and the $p_T^{b\bar{b}}$ (bottom left) and $m_{b\bar{b}}$ (bottom right) of the b jet pair. The superscript 'b' refers to both b and \bar{b} jets. The data points are placed at the midpoint of the bins. The inner (outer) error bars indicate the statistical (combined statistical and systematic) uncertainties. The measurements are compared to predictions from MADGRAPH+PYTHIA6, POWHEG+PYTHIA6, POWHEG+HERWIG6, and MC@NLO+HERWIG6. The lower part of each plot shows the ratio of the predictions to data.

considered predictions, except for the NLO+NNLL calculation, which fails to describe the data for all $p_T^{\text{t}\bar{\text{t}}}$ values.

The results from the ℓ +jets and dilepton channels are compared to each other in Figs. 15 to 17. This is only feasible for the top quark and $\text{t}\bar{\text{t}}$ quantities, since they are measured in the same phase space (i.e. the full parton level phase space) for both channels. The results are presented relative to the MADGRAPH+PYTHIA6 prediction to highlight the level of agreement between data and the default $\text{t}\bar{\text{t}}$ simulation. To facilitate the comparison of measurements that are performed using different size and number of bins, a horizontal bin-centre correction is applied to all data points from both channels. In each bin, the measured data points are presented at the horizontal position in the bin where the predicted bin-averaged cross section equals the cross section of the unbinned MADGRAPH+PYTHIA6 calculation (cf. [51]), which is common for both channels. The data are also compared to the predictions from POWHEG+PYTHIA6, POWHEG+HERWIG6, MC@NLO+HERWIG6 relative to MADGRAPH+PYTHIA6. The results are consistent between the channels for all quantities, in particular, for all measurements related to the top quark p_T distribution. The softer spectrum in data relative to MADGRAPH+PYTHIA6 is clearly visible.

In addition, a comparison between results obtained at $\sqrt{s} = 7$ [5] and 8 TeV is also performed for both the ℓ +jets and dilepton channels, and presented in Figs. 18 and 19 for p_T^t , y_t , $p_T^{\text{t}\bar{\text{t}}}$, $y_{\text{t}\bar{\text{t}}}$, and $m_{\text{t}\bar{\text{t}}}$. Since the fiducial phase space definition for the normalized differential cross sections is also different for each value of \sqrt{s} , the comparison is again only possible for top quark and $\text{t}\bar{\text{t}}$ quantities. The measurements are presented relative to the corresponding default MADGRAPH+PYTHIA6 predictions at 7 and 8 TeV. A horizontal bin-centre correction with respect to the MADGRAPH+PYTHIA6 predictions is applied to all data points from both channels and \sqrt{s} values. The results are consistent between the channels for all quantities, both at 7 and 8 TeV. The uncertainties in almost all bins of the distributions are reduced for the 8 TeV results relative to 7 TeV, mainly due to the improvements discussed in Section 4.3. The softer p_T^t in data relative to MADGRAPH+PYTHIA6 is also visible at 7 TeV.

7 Summary

First measurements are presented of normalized differential $\text{t}\bar{\text{t}}$ production cross sections in pp collisions at $\sqrt{s} = 8$ TeV. The measurements are performed with the CMS detector in the ℓ +jets ($\ell = e$ or μ) and dilepton (e^+e^- , $\mu^+\mu^-$, and $e^\pm\mu^\mp$) $\text{t}\bar{\text{t}}$ decay channels. The normalized $\text{t}\bar{\text{t}}$ cross section is measured as a function of the transverse momentum, rapidity, and invariant mass of the final-state leptons and b jets in the fiducial phase space, and the top quarks and $\text{t}\bar{\text{t}}$ system in the full phase space. The measurements in the different decay channels are in agreement with each other. In general, the data are in agreement with standard model predictions up to approximate NNLO precision. Among the examined predictions, POWHEG+HERWIG6 provides the best overall description of the data. However, the p_T spectrum in data for leptons, jets, and top quarks is softer than expected, particularly for MADGRAPH+PYTHIA6, POWHEG+PYTHIA6, and MC@NLO+HERWIG6. The calculation at approximate NNLO precision also provides a good description of the top quark p_T spectrum. The $m_{\text{t}\bar{\text{t}}}$ distribution in data tends to be lower than the predictions for large $m_{\text{t}\bar{\text{t}}}$ values. The $p_T^{\text{t}\bar{\text{t}}}$ spectrum is well described by all the considered predictions, except for the NLO+NNLL calculation, which fails to describe the data for all $p_T^{\text{t}\bar{\text{t}}}$ values. The results show the same behaviour as the corresponding CMS measurements at $\sqrt{s} = 7$ TeV.

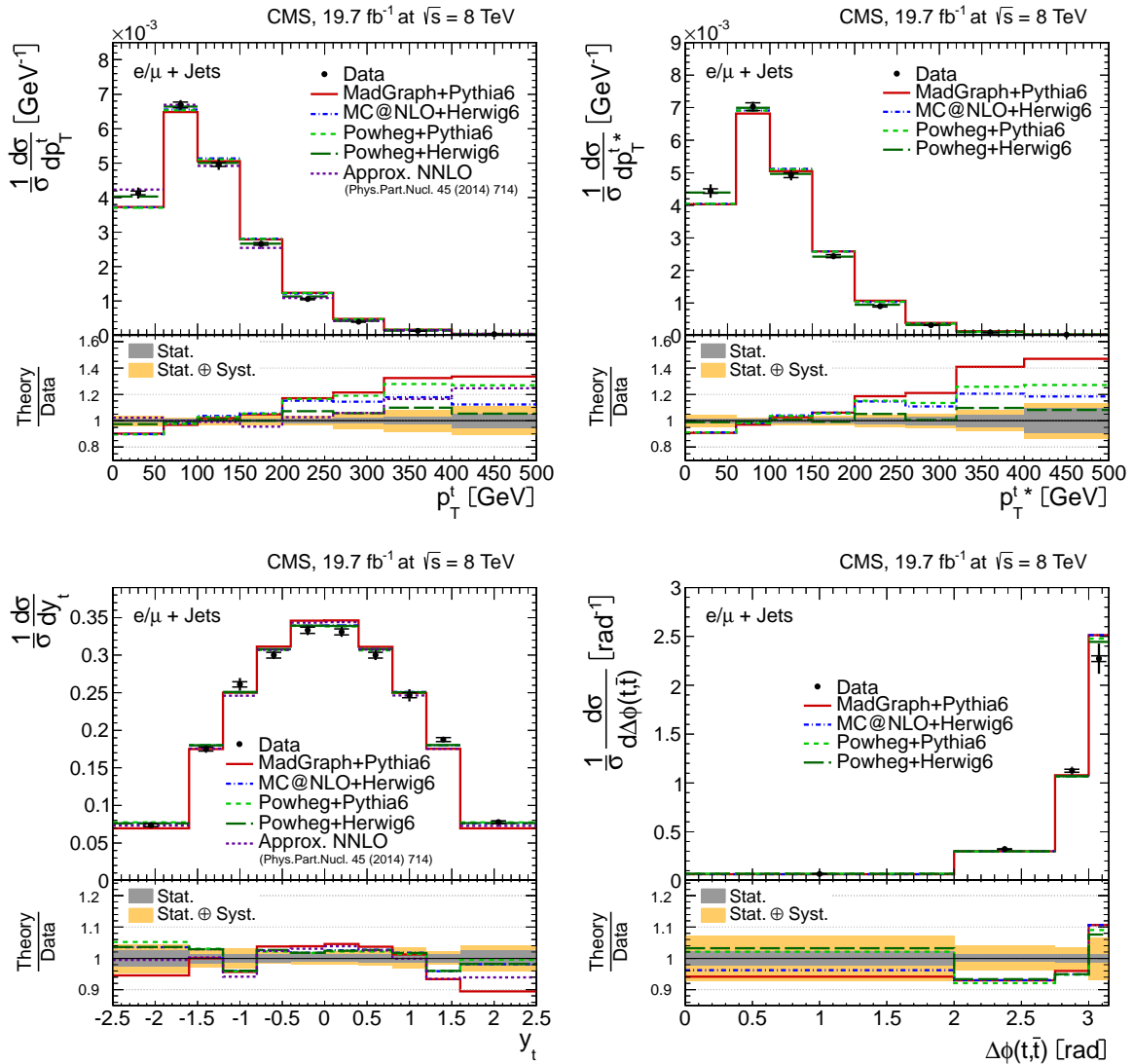


Figure 9: Normalized differential $t\bar{t}$ production cross section in the ℓ +jets channels as a function of the p_T^t (top left), the $t\bar{t}$ rest frame $p_T^{t^*}$ (top right), and the rapidity y_t (bottom left) of the top quarks or antiquarks, and the difference in the azimuthal angle between the top quark and the antiquark $\Delta\phi(t, \bar{t})$ (bottom right). The data points are placed at the midpoint of the bins. The inner (outer) error bars indicate the statistical (combined statistical and systematic) uncertainties. The measurements are compared to predictions from MADGRAPH+PYTHIA6, POWHEG+PYTHIA6, POWHEG+HERWIG6, MC@NLO+HERWIG6, and to approximate NNLO [16] calculations, when available. The lower part of each plot shows the ratio of the predictions to data.

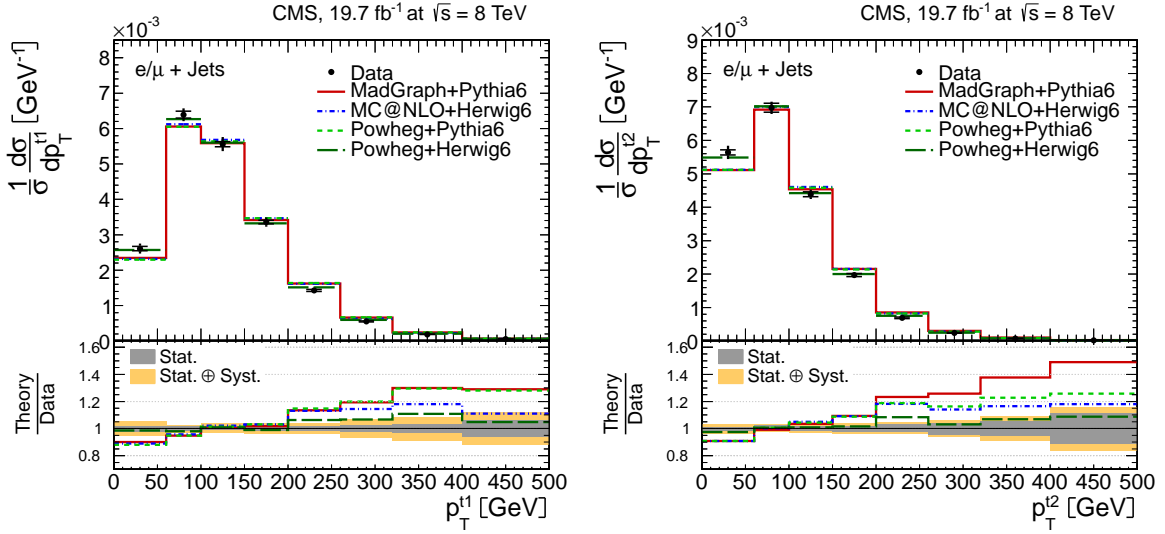


Figure 10: Normalized differential $t\bar{t}$ production cross section in the ℓ +jets channels as a function of the p_T of the leading (left) and trailing (right) top quarks or antiquarks. The data points are placed at the midpoint of the bins. The inner (outer) error bars indicate the statistical (combined statistical and systematic) uncertainties. The measurements are compared to predictions from MADGRAPH+PYTHIA6, POWHEG+PYTHIA6, POWHEG+HERWIG6, and MC@NLO+HERWIG6. The lower part of each plot shows the ratio of the predictions to data.

Acknowledgments

We congratulate our colleagues in the CERN accelerator departments for the excellent performance of the LHC and thank the technical and administrative staffs at CERN and at other CMS institutes for their contributions to the success of the CMS effort. In addition, we gratefully acknowledge the computing centres and personnel of the Worldwide LHC Computing Grid for delivering so effectively the computing infrastructure essential to our analyses. Finally, we acknowledge the enduring support for the construction and operation of the LHC and the CMS detector provided by the following funding agencies: the Austrian Federal Ministry of Science, Research and Economy and the Austrian Science Fund; the Belgian Fonds de la Recherche Scientifique, and Fonds voor Wetenschappelijk Onderzoek; the Brazilian Funding Agencies (CNPq, CAPES, FAPERJ, and FAPESP); the Bulgarian Ministry of Education and Science; CERN; the Chinese Academy of Sciences, Ministry of Science and Technology, and National Natural Science Foundation of China; the Colombian Funding Agency (COLCIENCIAS); the Croatian Ministry of Science, Education and Sport, and the Croatian Science Foundation; the Research Promotion Foundation, Cyprus; the Ministry of Education and Research, Estonian Research Council via IUT23-4 and IUT23-6 and European Regional Development Fund, Estonia; the Academy of Finland, Finnish Ministry of Education and Culture, and Helsinki Institute of Physics; the Institut National de Physique Nucléaire et de Physique des Particules / CNRS, and Commissariat à l'Énergie Atomique et aux Énergies Alternatives / CEA, France; the Bundesministerium für Bildung und Forschung, Deutsche Forschungsgemeinschaft, and Helmholtz-Gemeinschaft Deutscher Forschungszentren, Germany; the General Secretariat for Research and Technology, Greece; the National Scientific Research Foundation, and National Innovation Office, Hungary; the Department of Atomic Energy and the Department of Science and Technology, India; the Institute for Studies in Theoretical Physics and Mathematics, Iran; the Science Foundation, Ireland; the Istituto Nazionale di Fisica Nucleare, Italy;

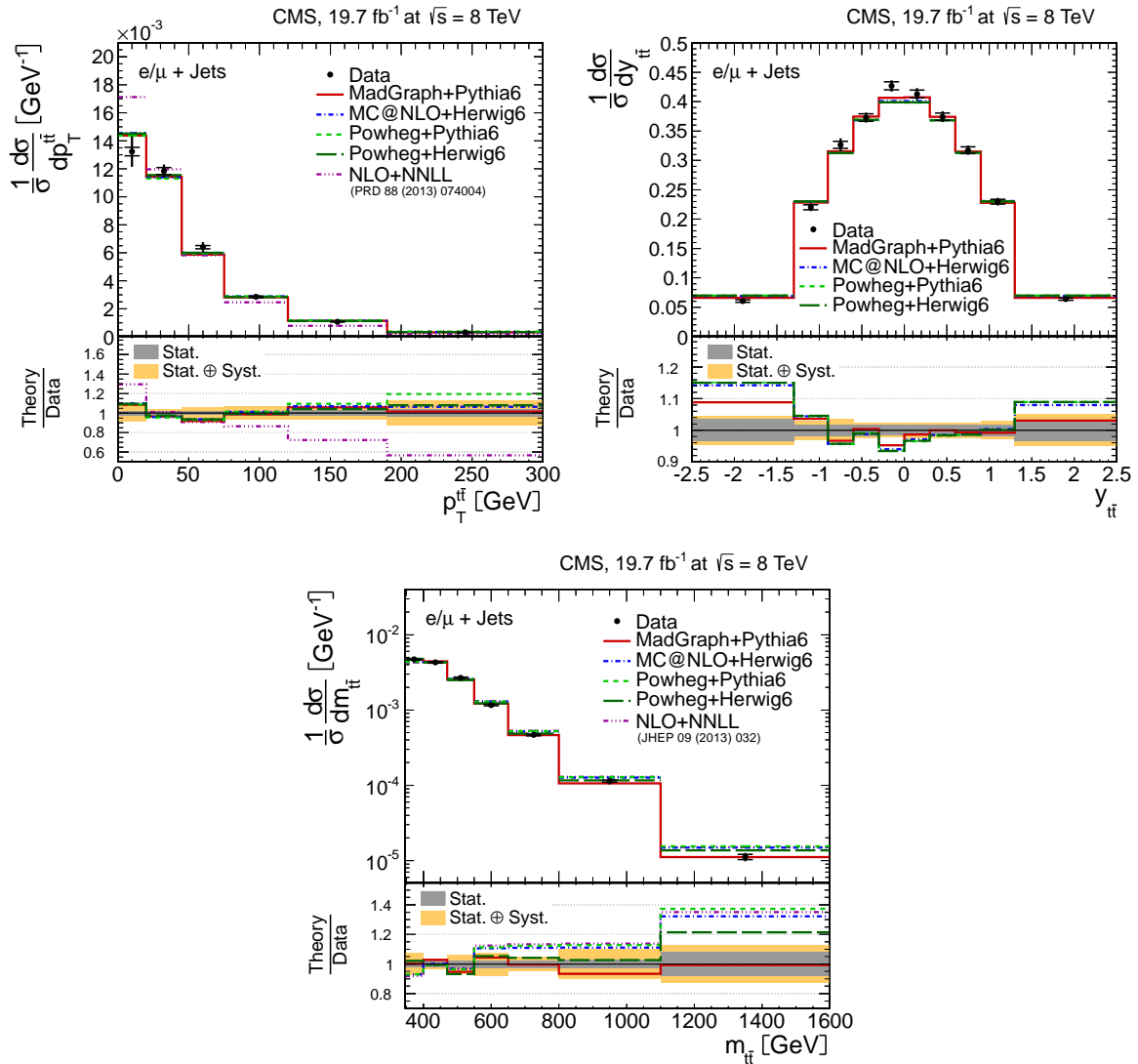


Figure 11: Normalized differential $t\bar{t}$ production cross section in the $\ell + \text{jets}$ channels as a function of the p_T^{tt} (top left), y_{tt} (top right), and m_{tt} (bottom) of the $t\bar{t}$ system. The data points are placed at the midpoint of the bins. The inner (outer) error bars indicate the statistical (combined statistical and systematic) uncertainties. The measurements are compared to predictions from MADGRAPH+PYTHIA6, POWHEG+PYTHIA6, POWHEG+HERWIG6, MC@NLO+HERWIG6, and to NLO+NNLL [14, 15] calculations, when available. The lower part of each plot shows the ratio of the predictions to data.

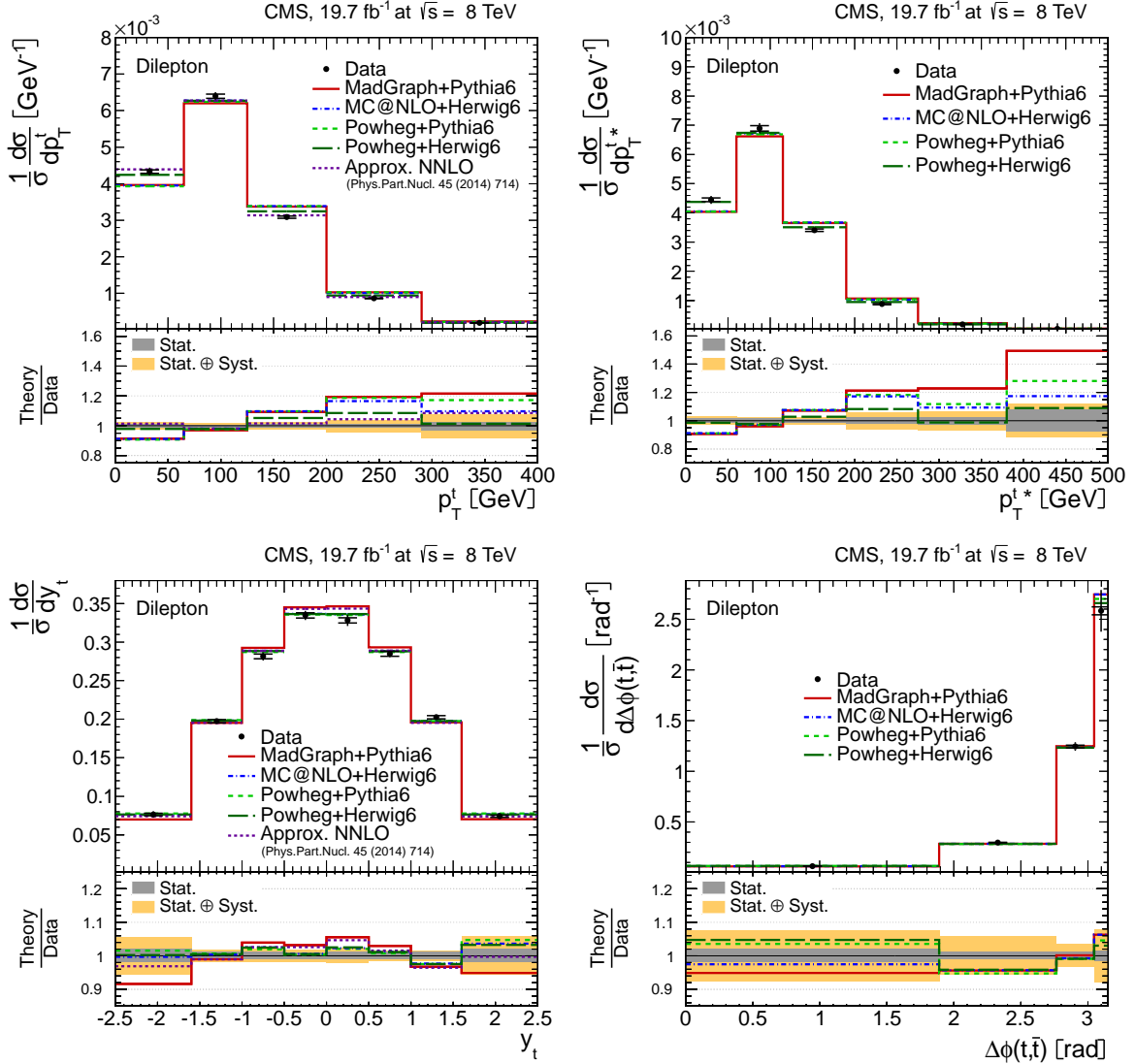


Figure 12: Normalized differential $t\bar{t}$ production cross section in the dilepton channels as a function of the p_T^t (top left), the $t\bar{t}$ rest frame p_T^{t*} (top right), and the rapidity y_t (bottom left) of the top quarks or antiquarks, and the difference in the azimuthal angle between the top quark and the antiquark $\Delta\phi(t, \bar{t})$ (bottom right). The data points are placed at the midpoint of the bins. The inner (outer) error bars indicate the statistical (combined statistical and systematic) uncertainties. The measurements are compared to predictions from MADGRAPH+PYTHIA6, POWHEG+PYTHIA6, POWHEG+HERWIG6, MC@NLO+HERWIG6, and to approximate NNLO [16] calculations, when available. The lower part of each plot shows the ratio of the predictions to data.

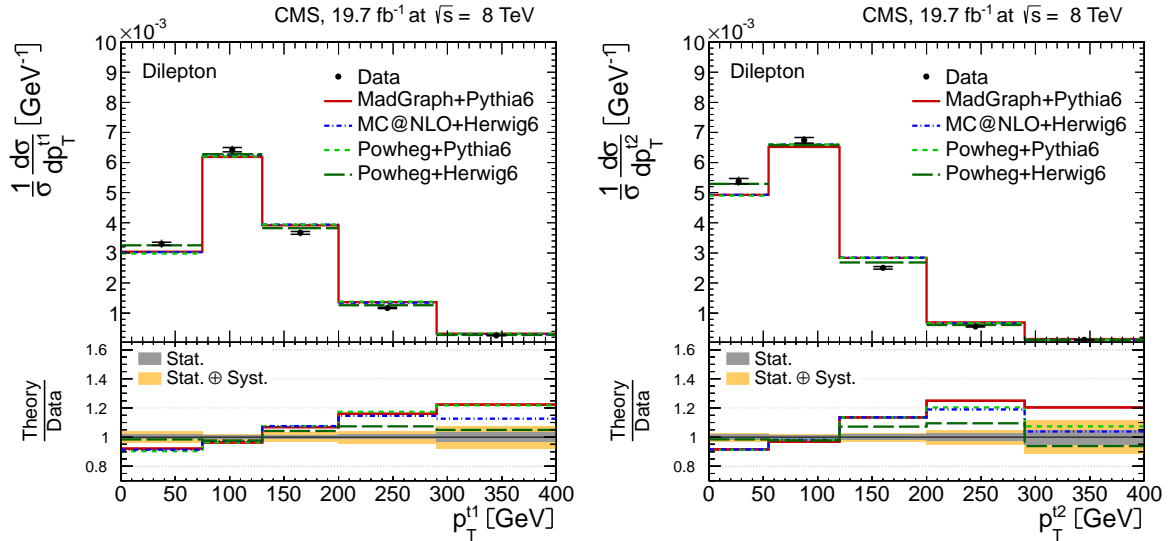


Figure 13: Normalized differential $t\bar{t}$ production cross section in the dilepton channels as a function of the p_T of the leading (left) and trailing (right) top quarks or antiquarks. The data points are placed at the midpoint of the bins. The inner (outer) error bars indicate the statistical (combined statistical and systematic) uncertainties. The measurements are compared to predictions from MADGRAPH+PYTHIA6, POWHEG+PYTHIA6, POWHEG+HERWIG6, and MC@NLO+HERWIG6. The lower part of each plot shows the ratio of the predictions to data.

the Ministry of Science, ICT and Future Planning, and National Research Foundation (NRF), Republic of Korea; the Lithuanian Academy of Sciences; the Ministry of Education, and University of Malaya (Malaysia); the Mexican Funding Agencies (CINVESTAV, CONACYT, SEP, and UASLP-FAI); the Ministry of Business, Innovation and Employment, New Zealand; the Pakistan Atomic Energy Commission; the Ministry of Science and Higher Education and the National Science Centre, Poland; the Fundação para a Ciência e a Tecnologia, Portugal; JINR, Dubna; the Ministry of Education and Science of the Russian Federation, the Federal Agency of Atomic Energy of the Russian Federation, Russian Academy of Sciences, and the Russian Foundation for Basic Research; the Ministry of Education, Science and Technological Development of Serbia; the Secretaría de Estado de Investigación, Desarrollo e Innovación and Programa Consolider-Ingenio 2010, Spain; the Swiss Funding Agencies (ETH Board, ETH Zurich, PSI, SNF, UniZH, Canton Zurich, and SER); the Ministry of Science and Technology, Taipei; the Thailand Center of Excellence in Physics, the Institute for the Promotion of Teaching Science and Technology of Thailand, Special Task Force for Activating Research and the National Science and Technology Development Agency of Thailand; the Scientific and Technical Research Council of Turkey, and Turkish Atomic Energy Authority; the National Academy of Sciences of Ukraine, and State Fund for Fundamental Researches, Ukraine; the Science and Technology Facilities Council, UK; the US Department of Energy, and the US National Science Foundation.

Individuals have received support from the Marie-Curie programme and the European Research Council and EPLANET (European Union); the Leventis Foundation; the A. P. Sloan Foundation; the Alexander von Humboldt Foundation; the Belgian Federal Science Policy Office; the Fonds pour la Formation à la Recherche dans l'Industrie et dans l'Agriculture (FRIA-Belgium); the Agentschap voor Innovatie door Wetenschap en Technologie (IWT-Belgium); the Ministry of Education, Youth and Sports (MEYS) of the Czech Republic; the Council of Science and Industrial Research, India; the HOMING PLUS programme of the Foundation for Polish

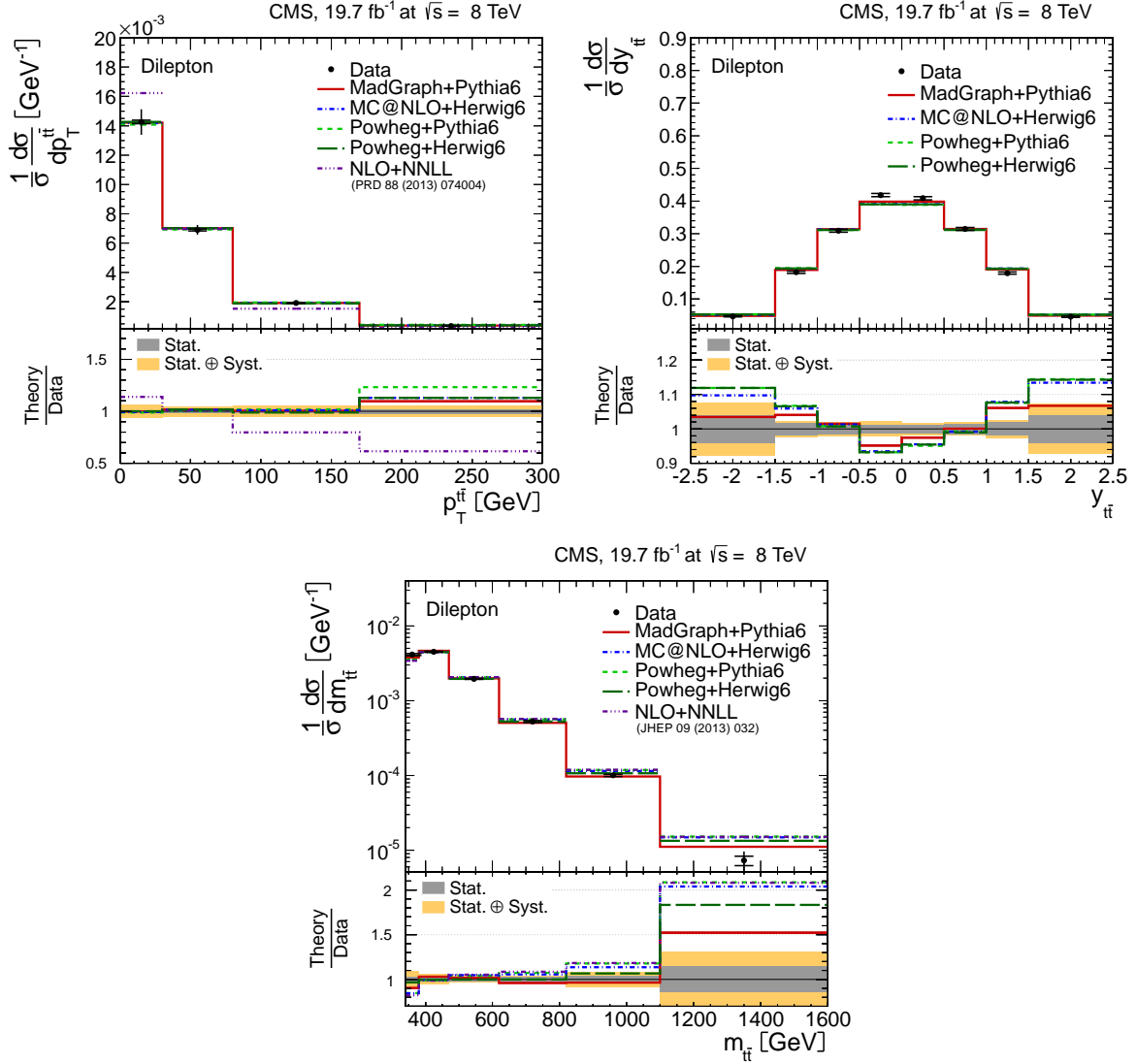


Figure 14: Normalized differential $t\bar{t}$ production cross section in the dilepton channels as a function of the $p_T^{t\bar{t}}$ (top left), $y_{t\bar{t}}$ (top right), and $m_{t\bar{t}}$ (bottom) of the $t\bar{t}$ system. The data points are placed at the midpoint of the bins. The inner (outer) error bars indicate the statistical (combined statistical and systematic) uncertainties. The measurements are compared to predictions from MADGRAPH+PYTHIA6, POWHEG+PYTHIA6, POWHEG+HERWIG6, MC@NLO+HERWIG6, and to NLO+NNLL [14, 15] calculations, when available. The lower part of each plot shows the ratio of the predictions to data.

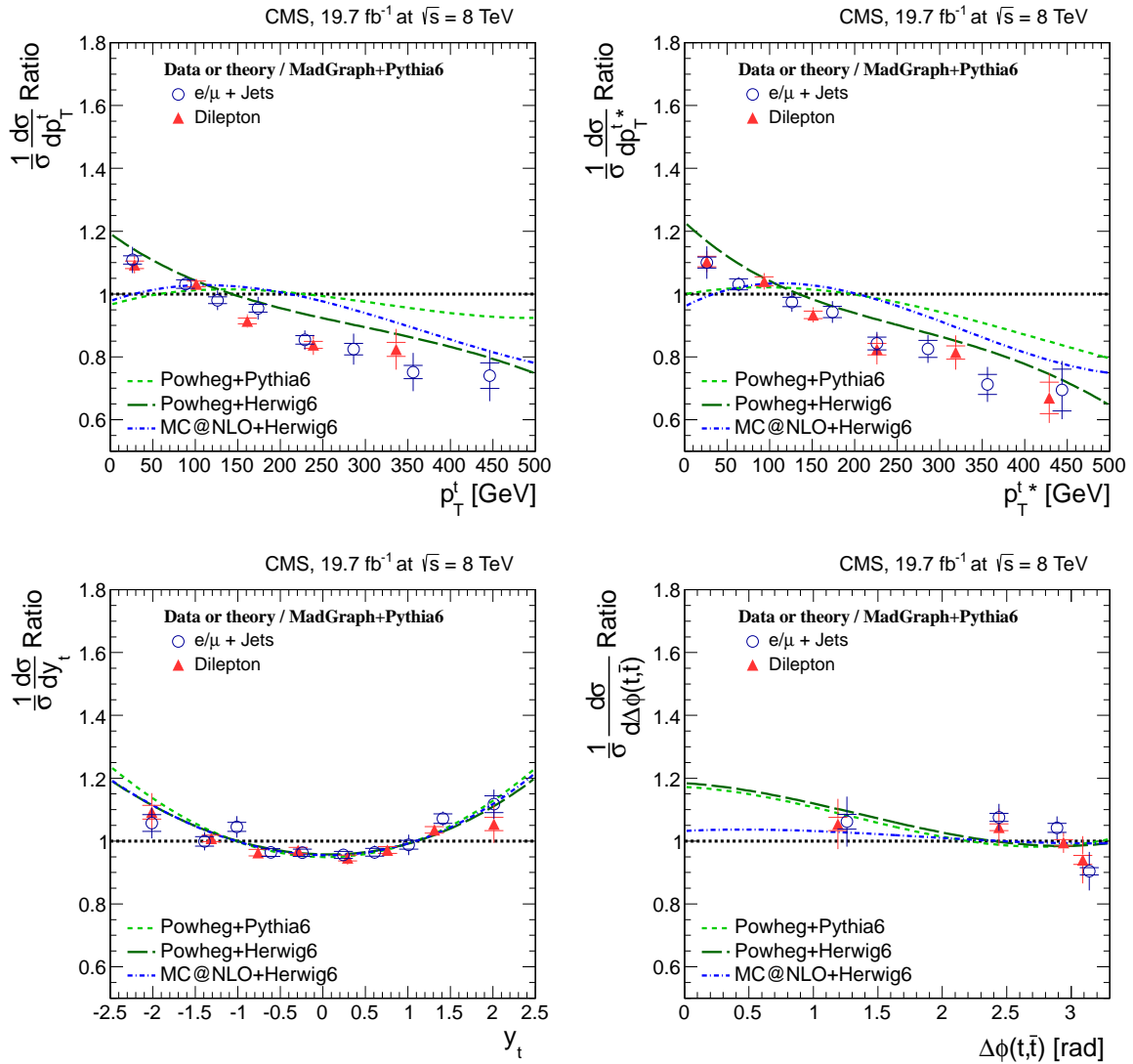


Figure 15: Comparison of normalized differential $t\bar{t}$ production cross section in the dilepton and l +jets channels as a function of the p_T^t (top left), the $t\bar{t}$ rest frame p_T^{t*} (top right), and the rapidity y_t (bottom left) of the top quarks or antiquarks, and the difference in the azimuthal angle between the top quark and the antiquark $\Delta\phi(t, \bar{t})$ (bottom right). The measurements are presented relative to the MADGRAPH+PYTHIA6 prediction. A horizontal bin-centre correction is applied to all data points (cf. Section 6.2). The inner (outer) error bars indicate the statistical (combined statistical and systematic) uncertainties. The predictions from POWHEG+PYTHIA6, POWHEG+HERWIG6, and MC@NLO+HERWIG6, also presented relative to MADGRAPH+PYTHIA6, are shown for comparison.

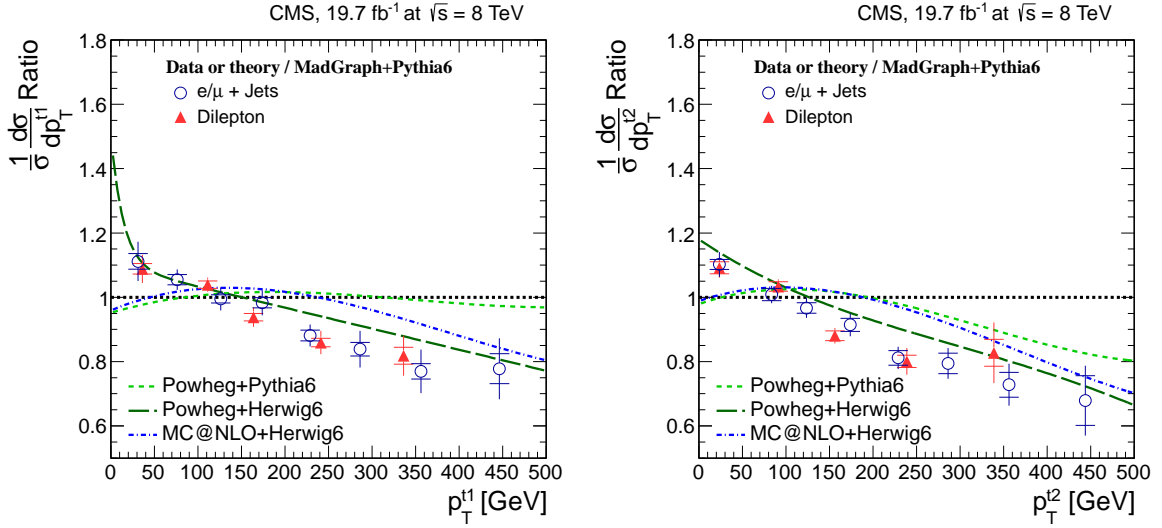


Figure 16: Comparison of normalized differential $t\bar{t}$ production cross section in the dilepton and ℓ +jets channels as a function of the p_T of the leading (left) and trailing (right) top quarks or antiquarks. The measurements are presented relative to the MADGRAPH+PYTHIA6 prediction. A horizontal bin-centre correction is applied to all data points (cf. Section 6.2). The inner (outer) error bars indicate the statistical (combined statistical and systematic) uncertainties. The predictions from POWHEG+PYTHIA6, POWHEG+HERWIG6, and MC@NLO+HERWIG6, also presented relative to MADGRAPH+PYTHIA6, are shown for comparison.

Science, cofinanced from European Union, Regional Development Fund; the Compagnia di San Paolo (Torino); the Consorzio per la Fisica (Trieste); MIUR project 20108T4XTM (Italy); the Thalys and Aristeia programmes cofinanced by EU-ESF and the Greek NSRF; and the National Priorities Research Program by Qatar National Research Fund.

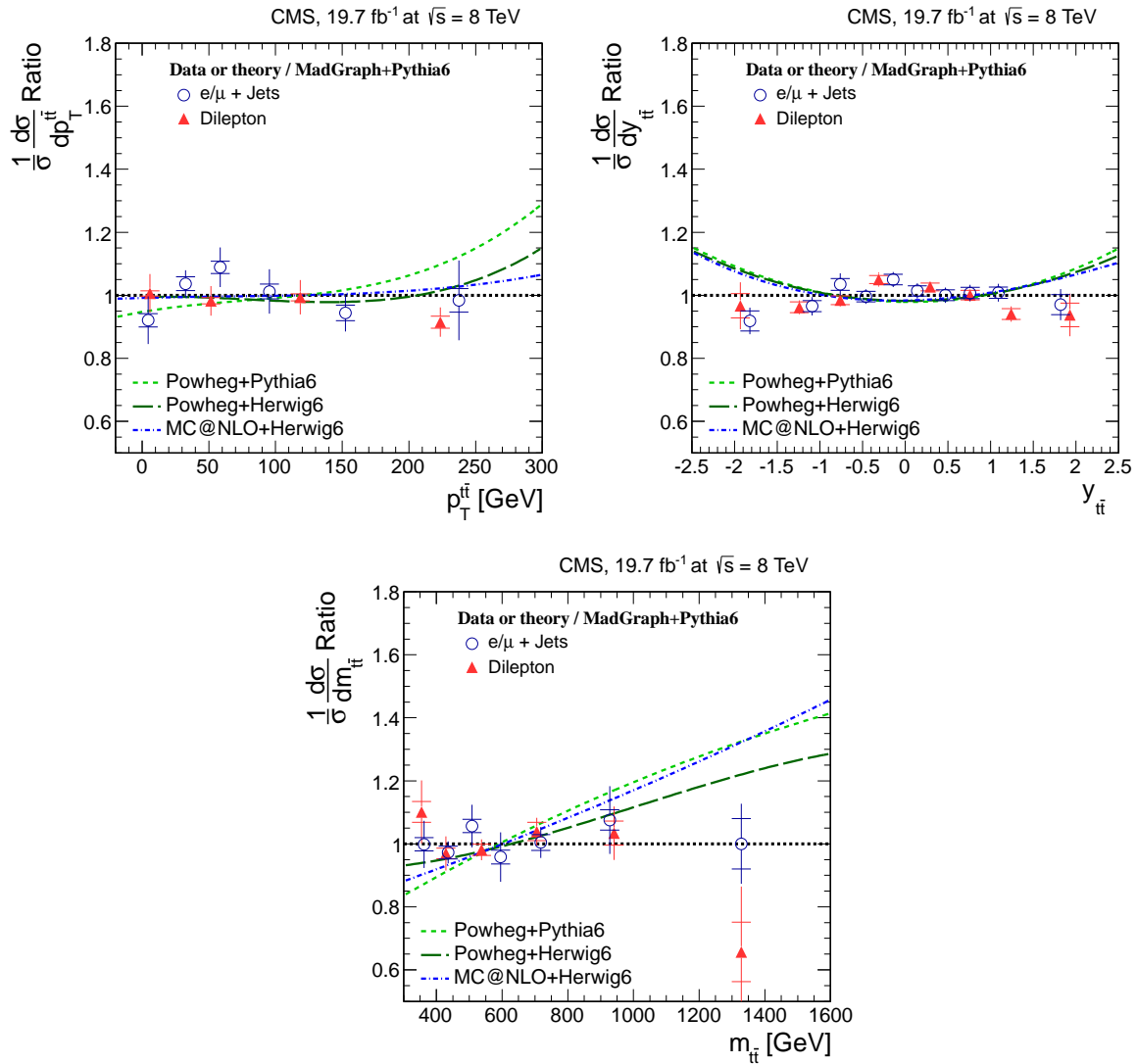


Figure 17: Comparison of normalized differential $t\bar{t}$ production cross section in the dilepton and l +jets channels as a function of the $p_T^{t\bar{t}}$ (top left), $y_{t\bar{t}}$ (top right), and $m_{t\bar{t}}$ (bottom) of the $t\bar{t}$ system. The measurements are presented relative to the MADGRAPH+PYTHIA6 prediction. A horizontal bin-centre correction is applied to all data points (cf. Section 6.2). The inner (outer) error bars indicate the statistical (combined statistical and systematic) uncertainties. The predictions from POWHEG+PYTHIA6, POWHEG+HERWIG6, and MC@NLO+HERWIG6, also presented relative to MADGRAPH+PYTHIA6, are shown for comparison. For better visibility, data points with identical bin centres (cf. Tables A.6 and A.10) are shifted horizontally by a negligible amount.

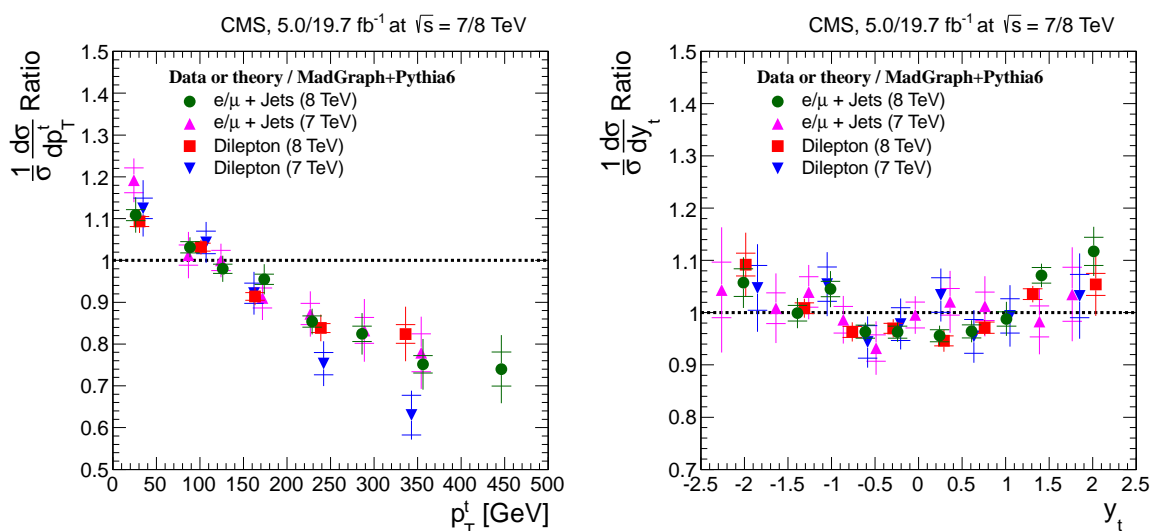


Figure 18: Comparison of normalized differential $t\bar{t}$ production cross section in the dilepton and ℓ +jets channels at 7 TeV [5] and 8 TeV, as a function of the p_T^t (left) and rapidity y_t (right) of the top quarks or antiquarks. The measurements are presented relative to the corresponding MADGRAPH+PYTHIA6 predictions. A horizontal bin-centre correction is applied to all data points (cf. Section 6.2). The inner (outer) error bars indicate the statistical (combined statistical and systematic) uncertainties. For better visibility, data points with identical bin centres (cf. Tables A.6 and A.10) are shifted horizontally by a negligible amount.

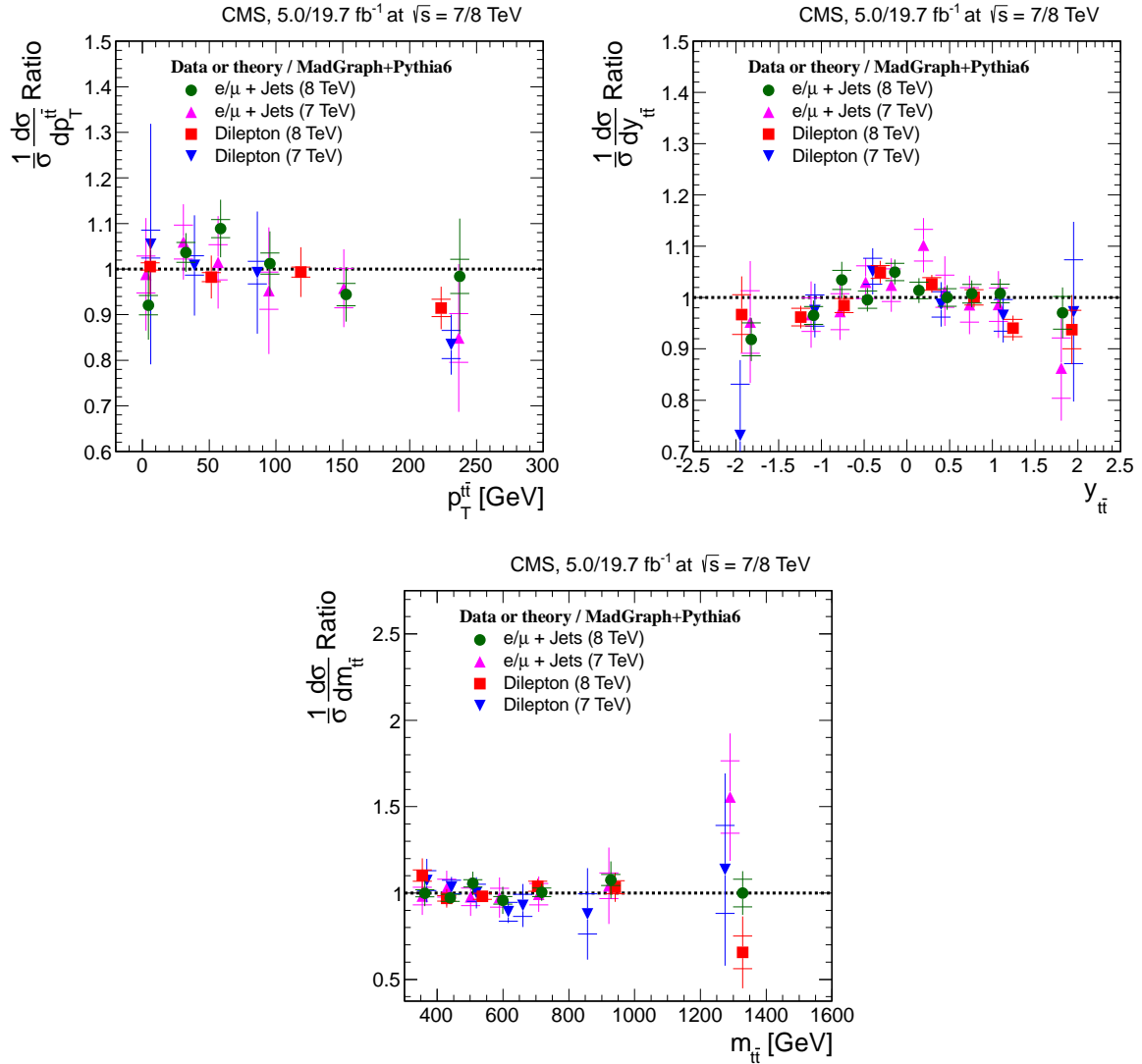


Figure 19: Comparison of normalized differential $t\bar{t}$ production cross section in the dilepton and ℓ +jets channels at 7 TeV [5] and 8 TeV, as a function of the $p_T^{t\bar{t}}$ (top left), $y_{t\bar{t}}$ (top right), and $m_{t\bar{t}}$ (bottom) of the $t\bar{t}$ system. The measurements are presented relative to the corresponding MADGRAPH+PYTHIA6 predictions. A horizontal bin-centre correction is applied to all data points (cf. Section 6.2). The inner (outer) error bars indicate the statistical (combined statistical and systematic) uncertainties. For better visibility, data points with identical bin centres (cf. Tables A.9 and A.12) are shifted horizontally by a negligible amount.

References

- [1] R. Frederix and F. Maltoni, “Top pair invariant mass distribution: a window on new physics”, *JHEP* **01** (2009) 047, doi:10.1088/1126-6708/2009/01/047, arXiv:0712.2355.
- [2] CDF Collaboration, “First Measurement of the $t\bar{t}$ Differential Cross Section $d\sigma/dM_{t\bar{t}}$ in $p\bar{p}$ Collisions at $\sqrt{s} = 1.96$ TeV”, *Phys. Rev. Lett.* **102** (2009) 222003, doi:10.1103/PhysRevLett.102.222003, arXiv:0903.2850.
- [3] D0 Collaboration, “Measurement of differential $t\bar{t}$ production cross sections in $p\bar{p}$ collisions”, *Phys. Rev. D* **90** (2014) 092006, doi:10.1103/PhysRevD.90.092006, arXiv:1401.5785.
- [4] ATLAS Collaboration, “Measurements of top quark pair relative differential cross-sections with ATLAS in pp collisions at $\sqrt{s} = 7$ TeV”, *Eur. Phys. J. C* **73** (2013) 2261, doi:10.1140/epjc/s10052-012-2261-1, arXiv:1207.5644.
- [5] CMS Collaboration, “Measurement of differential top-quark pair production cross sections in pp collisions at $\sqrt{s} = 7$ TeV”, *Eur. Phys. J. C* **73** (2013) 2339, doi:10.1140/epjc/s10052-013-2339-4, arXiv:1211.2220.
- [6] ATLAS Collaboration, “Measurements of normalized differential cross-sections for $t\bar{t}$ production in pp collisions at $\sqrt{s} = 7$ TeV using the ATLAS detector”, *Phys. Rev. D* **90** (2014) 072004, doi:10.1103/PhysRevD.90.072004, arXiv:1407.0371.
- [7] J. Alwall et al., “MadGraph v5: going beyond”, *JHEP* **06** (2011) 128, doi:10.1007/JHEP06(2011)128, arXiv:1106.0522.
- [8] T. Sjöstrand, S. Mrenna, and P. Skands, “PYTHIA 6.4 physics and manual”, *JHEP* **05** (2006) 026, doi:10.1088/1126-6708/2006/05/026, arXiv:hep-ph/0603175.
- [9] S. Alioli et al., “NLO single-top production matched with shower in POWHEG: s - and t -channel contributions”, *JHEP* **09** (2009) 111, doi:10.1088/1126-6708/2009/09/111, arXiv:0907.4076.
- [10] S. Alioli et al., “A general framework for implementing NLO calculations in shower Monte Carlo programs: the POWHEG BOX”, *JHEP* **06** (2010) 043, doi:10.1007/JHEP06(2010)043, arXiv:1002.2581.
- [11] E. Re, “Single-top Wt -channel production matched with parton showers using the POWHEG method”, *Eur. Phys. J. C* **71** (2011) 1547, doi:10.1140/epjc/s10052-011-1547-z, arXiv:1009.2450.
- [12] G. Corcella et al., “HERWIG 6.5: An event generator for hadron emission reactions with interfering gluons (including supersymmetric processes)”, *JHEP* **01** (2001) 010, doi:10.1088/1126-6708/2001/01/010, arXiv:hep-ph/0011363.
- [13] S. Frixione and B. R. Webber, “Matching NLO QCD computations and parton shower simulations”, *JHEP* **06** (2002) 29, doi:10.1088/1126-6708/2002/06/029, arXiv:hep-ph/0204244.
- [14] A. Ferroglia, B. D. Pecjak, and L. L. Yang, “Top-quark pair production at high invariant mass: an NNLO soft plus virtual approximation”, *JHEP* **09** (2013) 032, doi:10.1007/JHEP09(2013)032, arXiv:1306.1537.

- [15] H. T. Li et al., “Top quark pair production at small transverse momentum in hadronic collisions”, *Phys. Rev. D* **88** (2013) 074004, doi:10.1103/PhysRevD.88.074004, arXiv:1307.2464.
- [16] N. Kidonakis, “NNLL threshold resummation for top-pair and single-top production”, *Phys. Part. Nuclei* **45** (2014) 714, doi:10.1134/S1063779614040091, arXiv:1210.7813.
- [17] M. Guzzi, K. Lipka, and S.-O. Moch, “Top-quark pair production at hadron colliders: differential cross section and phenomenological applications with DiffTop”, *JHEP* **01** (2015) 082, doi:10.1007/JHEP01(2015)082, arXiv:1406.0386.
- [18] CMS Collaboration, “The CMS experiment at the CERN LHC”, *JINST* **3** (2008) S08004, doi:10.1088/1748-0221/3/08/S08004.
- [19] P. Artoisenet, R. Frederix, O. Mattelaer, and R. Rietkerk, “Automatic spin-entangled decays of heavy resonances in Monte Carlo simulations”, *JHEP* **03** (2013) 015, doi:10.1007/JHEP03(2013)015, arXiv:1212.3460.
- [20] J. Pumplin et al., “New generation of parton distributions with uncertainties from global QCD analysis”, *JHEP* **07** (2002) 012, doi:10.1088/1126-6708/2002/07/012, arXiv:hep-ph/0201195.
- [21] M. L. Mangano, M. Moretti, F. Piccinini, and M. Treccani, “Matching matrix elements and shower evolution for top-quark production in hadronic collisions”, *JHEP* **01** (2007) 013, doi:10.1088/1126-6708/2007/01/013, arXiv:hep-ex/0611129.
- [22] GEANT4 Collaboration, “GEANT4—a simulation toolkit”, *Nucl. Instrum. Meth. A* **506** (2003) 250, doi:10.1016/S0168-9002(03)01368-8.
- [23] ATLAS Collaboration, “ATLAS tunes of PYTHIA 6 and Pythia 8 for MC11”, ATLAS PUB note ATL-PHYS-PUB-2011-009.
- [24] H.-L. Lai et al., “New parton distributions for collider physics”, *Phys. Rev. D* **82** (2010) 074024, doi:10.1103/PhysRevD.82.074024, arXiv:1007.2241.
- [25] A. D. Martin, W. J. Stirling, R. S. Thorne, and G. Watt, “Parton distributions for the LHC”, *Eur. Phys. J. C* **63** (2009) 189, doi:10.1140/epjc/s10052-009-1072-5, arXiv:0901.0002.
- [26] CMS Collaboration, “Measurement of the underlying event activity at the LHC with $\sqrt{s} = 7$ TeV and comparison with $\sqrt{s} = 0.9$ TeV”, *JHEP* **09** (2011) 109, doi:10.1007/JHEP09(2011)109, arXiv:1107.0330.
- [27] K. Melnikov and F. Petriello, “Electroweak gauge boson production at hadron colliders through $\mathcal{O}(\alpha_S^2)$ ”, *Phys. Rev. D* **74** (2006) 114017, doi:10.1103/PhysRevD.74.114017, arXiv:hep-ph/0609070.
- [28] K. Melnikov and F. Petriello, “The W boson production cross section at the LHC through $\mathcal{O}(\alpha_S^2)$ ”, *Phys. Rev. Lett.* **96** (2006) 231803, doi:10.1103/PhysRevLett.96.231803, arXiv:hep-ph/0603182.
- [29] J. M. Campbell, R. K. Ellis, and C. Williams, “Vector boson pair production at the LHC”, *JHEP* **07** (2011) 018, doi:10.1007/JHEP07(2011)018, arXiv:1105.0020.

- [30] J. M. Campbell and R. K. Ellis, “ $t\bar{t}W^\pm$ production and decay at NLO”, *JHEP* **07** (2012) 052, doi:10.1007/JHEP07(2012)052, arXiv:1204.5678.
- [31] M. V. Garzelli, A. Kardos, C. G. Papadopoulos, and Z. Trócsányi, “ $t\bar{t}W^\pm$ and $t\bar{t}Z$ hadroproduction at NLO accuracy in QCD with Parton Shower and Hadronization effects”, *JHEP* **11** (2012) 056, doi:10.1007/JHEP11(2012)056, arXiv:1208.2665.
- [32] W. Kilian, T. Ohl, and J. Reuter, “WHIZARD: Simulating multi-particle processes at LHC and ILC”, *Eur. Phys. J. C* **71** (2011) 1742, doi:10.1140/epjc/s10052-011-1742-y, arXiv:hep-ph/9905386.
- [33] K. Melnikov, M. Schulze, and A. Scharf, “QCD corrections to top quark pair production in association with a photon at hadron colliders”, *Phys. Rev. D* **83** (2011) 074013, doi:10.1103/epjc/PhysRevD.83.074013, arXiv:1102.1967.
- [34] CMS Collaboration, “Particle-flow event reconstruction in CMS and performance for jets, taus, and E_T^{miss} ”, CMS Physics Analysis Summary CMS-PAS-PFT-09-001, 2009.
- [35] CMS Collaboration, “Commissioning of the particle-flow event reconstruction with the first LHC collisions recorded in the CMS detector”, CMS Physics Analysis Summary CMS-PAS-PFT-10-001, 2010.
- [36] M. Cacciari, G. P. Salam, and G. Soyez, “The catchment area of jets”, *JHEP* **04** (2008) 005, doi:10.1088/1126-6708/2008/04/005, arXiv:0802.1188.
- [37] CMS Collaboration, “Performance of electron reconstruction and selection with the CMS detector in proton-proton collisions at $\sqrt{s} = 8$ TeV”, (2015). arXiv:1502.02701. Submitted to *JINST*.
- [38] CMS Collaboration, “Determination of jet energy calibration and transverse momentum resolution in CMS”, *JINST* **6** (2011) P11002, doi:10.1088/1748-0221/6/11/P11002, arXiv:1107.4277.
- [39] M. Cacciari, G. P. Salam, and G. Soyez, “The anti- k_t jet clustering algorithm”, *JHEP* **04** (2008) 063, doi:10.1088/1126-6708/2008/04/063, arXiv:0802.1189.
- [40] CMS Collaboration, “Identification of b-quark jets with the CMS experiment”, *JINST* **8** (2013) P04013, doi:10.1088/1748-0221/8/04/P04013, arXiv:1211.4462.
- [41] CMS Collaboration, “Missing transverse energy performance of the CMS detector”, *JINST* **6** (2011) P09001, doi:10.1088/1748-0221/6/09/P09001, arXiv:1106.5048.
- [42] CMS Collaboration, “Performance of missing transverse energy reconstruction by the CMS experiment in $\sqrt{s} = 8$ TeV pp data”, *JINST* **10** (2015) P02006, doi:10.1088/1748-0221/10/02/P02006, arXiv:1411.0511.
- [43] CMS Collaboration, “Measurement of the $t\bar{t}$ production cross section and the top quark mass in the dilepton channel in pp collisions at $\sqrt{s} = 7$ TeV”, *JHEP* **07** (2011) 049, doi:10.1007/JHEP07(2011)049, arXiv:1105.5661.
- [44] J. d’Hondt et al., “Fitting of event topologies with external kinematic constraints in CMS”, CMS Note 2006-023, 2006.

- [45] D0 Collaboration, "Measurement of the top quark mass using dilepton events", *Phys. Rev. Lett.* **80** (1998) 2063, doi:10.1103/PhysRevLett.80.2063, arXiv:hep-ex/9706014.
- [46] CMS Collaboration, "Measurement of the Drell-Yan cross sections in pp collisions at $\sqrt{s} = 7$ TeV with the CMS experiment", *JHEP* **10** (2011) 007, doi:10.1007/JHEP10(2011)007, arXiv:1108.0566.
- [47] TOTEM Collaboration, "First measurement of the total proton-proton cross section at the LHC energy of $\sqrt{s} = 7$ TeV", *Europhys. Lett.* **96** (2011) 21002, doi:10.1209/0295-5075/96/21002, arXiv:1110.1395.
- [48] A. Hoecker and V. Kartvelishvili, "SVD approach to data unfolding", *Nucl. Instrum. Meth. A* **372** (1996) 469, doi:10.1016/0168-9002(95)01478-0, arXiv:hep-ph/9509307.
- [49] V. Blobel, "An unfolding method for high energy physics experiments", (2002). arXiv:hep-ex/0208022.
- [50] F. James, "Statistical methods in experimental physics". World Scientific, 2nd edition, 2006.
- [51] G. D. Lafferty and T. R. Wyatt, "Where to stick your data points: the treatment of measurements within wide bins", *Nucl. Instrum. Meth. A* **355** (1995) 541, doi:10.1016/0168-9002(94)01112-5.

A Values of the normalized differential cross sections

In Tables A.1 to A.12, the results for the normalized differential distributions are summarized. For each distribution, the result of the measurement, together with the bin range, as well as the statistical, systematic, and total uncertainties, are provided. For the top quark or antiquark and $t\bar{t}$ quantities, the bin centres corrected according to the MADGRAPH+PYTHIA6 prediction (cf. Section 6.2) are also presented.

Table A.1: Normalized differential $t\bar{t}$ cross section in the ℓ +jets channels as a function of the charged lepton transverse momentum (p_T^ℓ) and pseudorapidity (η_ℓ). The superscript ' ℓ ' refers to both ℓ^+ and ℓ^- . The results are presented at particle level in the fiducial phase space. The statistical and systematic uncertainties are added in quadrature to yield the total uncertainty.

p_T^ℓ bin range [GeV]	$1/\sigma \, d\sigma/dp_T^\ell$ [GeV^{-1}]	Stat. [%]	Syst. [%]	Total [%]
[30, 37)	1.43×10^{-2}	2.2	2.4	3.2
[37, 45)	2.21×10^{-2}	1.4	2.8	3.1
[45, 55)	1.83×10^{-2}	1.4	1.7	2.3
[55, 68)	1.36×10^{-2}	1.5	1.4	2.1
[68, 80)	9.42×10^{-3}	2.0	1.5	2.5
[80, 100)	5.89×10^{-3}	1.8	1.2	2.2
[100, 135)	2.51×10^{-3}	2.1	6.3	6.7
[135, 200)	5.73×10^{-4}	3.3	9.5	10.1
η_ℓ bin range	$1/\sigma \, d\sigma/d\eta_\ell$	Stat. [%]	Syst. [%]	Total [%]
[-2.1, -1.8)	9.76×10^{-2}	4.3	4.3	6.0
[-1.8, -1.5)	1.37×10^{-1}	3.3	3.1	4.5
[-1.5, -1.2)	1.94×10^{-1}	2.7	2.4	3.6
[-1.2, -0.9)	2.39×10^{-1}	2.5	2.8	3.7
[-0.9, -0.6)	3.03×10^{-1}	2.0	2.3	3.0
[-0.6, -0.3)	3.41×10^{-1}	1.9	1.4	2.3
[-0.3, 0.0)	3.60×10^{-1}	1.9	1.4	2.4
[0.0, 0.3)	3.39×10^{-1}	2.0	2.0	2.8
[0.3, 0.6)	3.35×10^{-1}	1.9	3.0	3.6
[0.6, 0.9)	3.06×10^{-1}	1.9	4.2	4.6
[0.9, 1.2)	2.25×10^{-1}	2.2	2.2	3.2
[1.2, 1.5)	2.01×10^{-1}	2.6	2.2	3.4
[1.5, 1.8)	1.36×10^{-1}	3.3	2.5	4.2
[1.8, 2.1)	9.31×10^{-2}	4.2	5.6	7.0

Table A.2: Normalized differential $t\bar{t}$ cross section in the ℓ +jets channels as a function of the b jet transverse momentum (p_T^b) and pseudorapidity (η_b), and the transverse momentum ($p_T^{b\bar{b}}$) and the invariant mass ($m_{b\bar{b}}$) of the $b\bar{b}$ system. The superscript ‘b’ refers to both b and \bar{b} jets. The results are presented at particle level in the fiducial phase space. The statistical and systematic uncertainties are added in quadrature to yield the total uncertainty.

p_T^b bin range [GeV]	$1/\sigma d\sigma/dp_T^b$ [GeV $^{-1}$]	Stat. [%]	Syst. [%]	Total [%]
[30, 48)	1.40×10^{-2}	1.2	7.0	7.1
[48, 75)	1.24×10^{-2}	0.9	1.8	2.0
[75, 180)	3.67×10^{-3}	0.7	4.9	5.0
[180, 400)	1.34×10^{-4}	3.3	12.4	12.9
η_b bin range	$1/\sigma d\sigma/d\eta_b$	Stat. [%]	Syst. [%]	Total [%]
[−2.4, −1.5)	1.01×10^{-1}	1.7	2.9	3.3
[−1.5, −1.0)	2.08×10^{-1}	1.3	1.5	2.0
[−1.0, −0.5)	2.77×10^{-1}	1.1	1.2	1.7
[−0.5, 0.0)	3.23×10^{-1}	1.1	2.0	2.2
[0.0, 0.5)	3.28×10^{-1}	1.1	1.9	2.1
[0.5, 1.0)	2.89×10^{-1}	1.1	1.0	1.5
[1.0, 1.5)	2.09×10^{-1}	1.4	2.2	2.6
[1.5, 2.4)	1.03×10^{-1}	1.6	2.8	3.2
$p_T^{b\bar{b}}$ bin range [GeV]	$1/\sigma d\sigma/dp_T^{b\bar{b}}$ [GeV $^{-1}$]	Stat. [%]	Syst. [%]	Total [%]
[0, 35)	3.41×10^{-3}	2.4	4.1	4.7
[35, 75)	6.55×10^{-3}	1.7	3.0	3.5
[75, 115)	8.51×10^{-3}	1.5	3.0	3.4
[115, 155)	5.04×10^{-3}	2.0	6.7	7.0
[155, 280)	5.79×10^{-4}	3.8	11.3	11.9
[280, 500)	0.17×10^{-4}	14.1	23.3	27.2
$m_{b\bar{b}}$ bin range [GeV]	$1/\sigma d\sigma/dm_{b\bar{b}}$ [GeV $^{-1}$]	Stat. [%]	Syst. [%]	Total [%]
[0, 85)	2.00×10^{-3}	1.9	7.6	7.9
[85, 135)	5.79×10^{-3}	1.7	3.9	4.3
[135, 190)	4.44×10^{-3}	2.0	3.0	3.6
[190, 255)	2.37×10^{-3}	2.5	4.6	5.3
[255, 325)	1.13×10^{-3}	3.7	7.6	8.5
[325, 415)	4.50×10^{-4}	4.9	8.6	10.0
[415, 505)	1.57×10^{-4}	8.8	10.9	14.0
[505, 630)	0.47×10^{-4}	12.6	28.4	31.1
[630, 800)	0.12×10^{-4}	21.9	15.4	26.8

Table A.3: Normalized differential $t\bar{t}$ cross section in the dilepton channels as a function of the charged lepton transverse momentum (p_{T}^{ℓ}) and pseudorapidity (η_{ℓ}). The superscript ' ℓ ' refers to both ℓ^+ and ℓ^- . The results are presented at particle level in the fiducial phase space. The statistical and systematic uncertainties are added in quadrature to yield the total uncertainty.

p_{T}^{ℓ} bin range [GeV]	$1/\sigma \text{d}\sigma/\text{d}p_{\text{T}}^{\ell}$ [GeV^{-1}]	Stat. [%]	Syst. [%]	Total [%]
[20, 40)	1.93×10^{-2}	0.5	1.6	1.7
[40, 70)	1.25×10^{-2}	0.5	0.7	0.9
[70, 120)	3.79×10^{-3}	0.8	1.8	2.0
[120, 180)	6.51×10^{-4}	2.0	7.2	7.4
[180, 400)	3.89×10^{-5}	4.6	12.0	12.9
η_{ℓ} bin range	$1/\sigma \text{d}\sigma/\text{d}\eta_{\ell}$	Stat. [%]	Syst. [%]	Total [%]
[-2.4, -2.1)	6.04×10^{-2}	3.0	2.7	4.1
[-2.1, -1.8)	9.49×10^{-2}	2.2	2.9	3.7
[-1.8, -1.5)	1.40×10^{-1}	1.9	1.3	2.3
[-1.5, -1.2)	1.98×10^{-1}	1.5	1.5	2.2
[-1.2, -0.9)	2.43×10^{-1}	1.4	0.6	1.5
[-0.9, -0.6)	2.86×10^{-1}	1.2	2.3	2.6
[-0.6, -0.3)	3.22×10^{-1}	1.2	1.0	1.5
[-0.3, 0.0)	3.36×10^{-1}	1.2	0.7	1.4
[0.0, 0.3)	3.17×10^{-1}	1.2	1.2	1.7
[0.3, 0.6)	3.23×10^{-1}	1.2	1.2	1.7
[0.6, 0.9)	2.90×10^{-1}	1.3	1.1	1.7
[0.9, 1.2)	2.43×10^{-1}	1.4	1.0	1.7
[1.2, 1.5)	1.97×10^{-1}	1.6	1.2	2.0
[1.5, 1.8)	1.30×10^{-1}	2.1	2.6	3.4
[1.8, 2.1)	9.70×10^{-2}	2.3	3.1	3.8
[2.1, 2.4)	5.38×10^{-2}	3.5	5.2	6.3

Table A.4: Normalized differential $t\bar{t}$ cross section in the dilepton channels as a function of the transverse momentum ($p_T^{\ell\ell}$) and the invariant mass ($m_{\ell\ell}$) of the dilepton pair. The superscript ' ℓ ' refers to both ℓ^+ and ℓ^- . The results are presented at particle level in the fiducial phase space. The statistical and systematic uncertainties are added in quadrature to yield the total uncertainty.

$p_T^{\ell\ell}$ bin range [GeV]	$1/\sigma \, d\sigma/dp_T^{\ell\ell}$ [GeV $^{-1}$]	stat. [%]	Syst. [%]	Total [%]
[0, 10)	1.84×10^{-3}	3.7	3.2	4.9
[10, 20)	4.82×10^{-3}	2.0	2.8	3.5
[20, 40)	7.74×10^{-3}	1.2	2.8	3.0
[40, 60)	1.10×10^{-2}	1.0	2.2	2.5
[60, 100)	9.70×10^{-3}	0.7	0.9	1.2
[100, 150)	2.87×10^{-3}	1.3	5.0	5.2
[150, 400)	1.03×10^{-4}	3.4	7.0	7.8
$m_{\ell\ell}$ bin range [GeV]	$1/\sigma \, d\sigma/dm_{\ell\ell}$ [GeV $^{-1}$]	Stat. [%]	Syst. [%]	Total [%]
[20, 30)	3.74×10^{-3}	2.6	2.3	3.5
[30, 50)	5.28×10^{-3}	1.5	2.1	2.6
[50, 76)	7.61×10^{-3}	1.0	1.6	1.9
[76, 106)	7.19×10^{-3}	1.0	2.1	2.4
[106, 130)	5.41×10^{-3}	1.3	1.4	1.9
[130, 170)	3.30×10^{-3}	1.4	1.7	2.2
[170, 260)	1.23×10^{-3}	1.5	3.4	3.7
[260, 400)	2.29×10^{-4}	2.7	6.9	7.4

Table A.5: Normalized differential $t\bar{t}$ cross section in the dilepton channels as a function of the b jet transverse momentum (p_T^b) and pseudorapidity (η_b), and the transverse momentum ($p_T^{b\bar{b}}$) and the invariant mass ($m_{b\bar{b}}$) of the $b\bar{b}$ system. The superscript ‘b’ refers to both b and \bar{b} jets. The results are presented at particle level in the fiducial phase space. The statistical and systematic uncertainties are added in quadrature to yield the total uncertainty.

p_T^b bin range [GeV]	$1/\sigma d\sigma/dp_T^b$ [GeV $^{-1}$]	Stat. [%]	Syst. [%]	Total [%]
[30, 50)	1.16×10^{-2}	1.2	7.7	7.8
[50, 80)	1.23×10^{-2}	1.2	3.8	4.0
[80, 130)	5.94×10^{-3}	1.4	3.4	3.7
[130, 210)	1.11×10^{-3}	2.2	5.1	5.5
[210, 400)	6.88×10^{-5}	6.8	13.5	15.1
η_b bin range	$1/\sigma d\sigma/d\eta_b$	Stat. [%]	Syst. [%]	Total [%]
[−2.4, −1.5)	1.08×10^{-1}	2.3	6.9	7.3
[−1.5, −1.0)	2.16×10^{-1}	2.0	1.8	2.7
[−1.0, −0.5)	2.74×10^{-1}	1.9	3.2	3.7
[−0.5, 0.0)	3.01×10^{-1}	1.9	3.2	3.7
[0.0, 0.5)	3.20×10^{-1}	1.8	2.6	3.2
[0.5, 1.0)	2.78×10^{-1}	1.9	2.6	3.2
[1.0, 1.5)	2.19×10^{-1}	2.0	1.9	2.7
[1.5, 2.4)	1.09×10^{-1}	2.4	5.8	6.2
$p_T^{b\bar{b}}$ bin range [GeV]	$1/\sigma d\sigma/dp_T^{b\bar{b}}$ [GeV $^{-1}$]	Stat. [%]	Syst. [%]	Total [%]
[0, 30)	3.49×10^{-3}	2.3	3.6	4.3
[30, 60)	6.50×10^{-3}	1.5	2.9	3.3
[60, 100)	8.07×10^{-3}	1.2	2.1	2.4
[100, 180)	4.27×10^{-3}	1.0	3.2	3.4
[180, 400)	1.54×10^{-4}	4.4	9.8	10.7
$m_{b\bar{b}}$ bin range [GeV]	$1/\sigma d\sigma/dm_{b\bar{b}}$ [GeV $^{-1}$]	Stat. [%]	Syst. [%]	Total [%]
[0, 60)	8.48×10^{-4}	1.9	3.9	4.3
[60, 120)	4.57×10^{-3}	0.9	2.7	2.8
[120, 240)	3.97×10^{-3}	0.6	1.0	1.1
[240, 600)	5.35×10^{-4}	1.3	4.6	4.8

Table A.6: Normalized differential $t\bar{t}$ cross section in the ℓ +jets channels as a function of top quark or antiquark observables: the transverse momentum (p_T^t) and the transverse momentum in the $t\bar{t}$ rest frame (p_T^{t*}) of the top quarks or antiquarks. The horizontally-corrected bin centres according to the MADGRAPH+PYTHIA6 prediction (cf. Section 6.2) are also provided. The results are presented at parton level in the full phase space. The statistical and systematic uncertainties are added in quadrature to yield the total uncertainty.

p_T^t bin range [GeV]	Bin centre [GeV]	$1/\sigma d\sigma/dp_T^t$ [GeV^{-1}]	Stat. [%]	Syst. [%]	Total [%]
[0, 60)	26.25	4.14×10^{-3}	1.2	3.6	3.8
[60, 100)	88.75	6.69×10^{-3}	1.3	1.7	2.1
[100, 150)	126.25	4.96×10^{-3}	1.1	3.0	3.2
[150, 200)	173.75	2.66×10^{-3}	1.3	3.5	3.7
[200, 260)	228.75	1.06×10^{-3}	1.6	3.2	3.6
[260, 320)	286.25	3.99×10^{-4}	2.2	5.6	6.0
[320, 400)	356.25	1.30×10^{-4}	2.8	7.6	8.1
[400, 500)	446.25	0.37×10^{-4}	5.5	9.5	10.9
p_T^{t*} bin range [GeV]	Bin centre [GeV]	$1/\sigma d\sigma/dp_T^{t*}$ [GeV^{-1}]	Stat. [%]	Syst. [%]	Total [%]
[0, 60)	26.25	4.44×10^{-3}	1.6	4.4	4.7
[60, 100)	63.75	7.03×10^{-3}	1.7	1.4	2.2
[100, 150)	126.25	4.93×10^{-3}	1.5	2.9	3.2
[150, 200)	173.75	2.44×10^{-3}	1.9	3.2	3.7
[200, 260)	226.25	9.00×10^{-4}	2.4	3.8	4.4
[260, 320)	286.25	3.21×10^{-4}	3.3	4.2	5.4
[320, 400)	356.25	0.94×10^{-4}	4.5	6.3	7.8
[400, 500)	443.75	0.25×10^{-4}	9.6	9.3	13.4

Table A.7: Normalized differential $t\bar{t}$ cross section in the ℓ +jets channels as a function of top quark or antiquark observables: the rapidity (y_t) of the top quarks or antiquarks, and the difference in the azimuthal angle between the top quark and antiquark ($\Delta\phi(t,\bar{t})$). The horizontally-corrected bin centres according to the MADGRAPH+PYTHIA6 prediction (cf. Section 6.2) are also provided. The results are presented at parton level in the full phase space. The statistical and systematic uncertainties are added in quadrature to yield the total uncertainty.

y_t bin range	Bin centre	$1/\sigma d\sigma/dy_t$	Stat. [%]	Syst. [%]	Total [%]
$[-2.5, -1.6)$	-2.01	7.36×10^{-2}	2.5	3.8	4.5
$[-1.6, -1.2)$	-1.39	1.75×10^{-1}	1.5	2.4	2.9
$[-1.2, -0.8)$	-1.01	2.61×10^{-1}	1.4	3.0	3.3
$[-0.8, -0.4)$	-0.61	3.00×10^{-1}	1.3	1.3	1.8
$[-0.4, 0.0)$	-0.24	3.33×10^{-1}	1.2	1.5	1.9
$[0.0, 0.4)$	0.24	3.31×10^{-1}	1.2	1.6	2.0
$[0.4, 0.8)$	0.61	3.00×10^{-1}	1.3	1.8	2.2
$[0.8, 1.2)$	1.01	2.47×10^{-1}	1.4	3.0	3.3
$[1.2, 1.6)$	1.41	1.88×10^{-1}	1.4	1.6	2.1
$[1.6, 2.5)$	2.01	7.77×10^{-2}	2.4	3.4	4.1
$\Delta\phi(t,\bar{t})$ bin range [rad]	Bin centre [rad]	$1/\sigma d\sigma/d\Delta\phi(t,\bar{t})$ [rad $^{-1}$]	Stat. [%]	Syst. [%]	Total [%]
$[0.00, 2.00)$	1.26	6.83×10^{-2}	2.2	7.0	7.3
$[2.00, 2.75)$	2.44	3.22×10^{-1}	1.2	3.8	4.0
$[2.75, 3.00)$	2.89	1.13	1.4	3.2	3.5
$[3.00, 3.15)$	3.14	2.27	1.3	6.6	6.8

Table A.8: Normalized differential $t\bar{t}$ cross section in the ℓ +jets channels as a function of the p_T of the leading (p_T^{t1}) and trailing (p_T^{t2}) top quarks or antiquarks. The horizontally-corrected bin centres according to the MADGRAPH+PYTHIA6 prediction (cf. Section 6.2) are also provided. The results are presented at parton level in the full phase space. The statistical and systematic uncertainties are added in quadrature to yield the total uncertainty.

p_T^{t1} bin range [GeV]	Bin centre [GeV]	$1/\sigma d\sigma/dp_T^{t1}$ [GeV $^{-1}$]	Stat. [%]	Syst. [%]	Total [%]
[0, 60)	31.25	2.61×10^{-3}	2.2	5.0	5.4
[60, 100)	76.25	6.39×10^{-3}	1.5	2.3	2.8
[100, 150)	126.25	5.56×10^{-3}	1.3	3.3	3.6
[150, 200)	173.75	3.36×10^{-3}	1.6	3.6	3.9
[200, 260)	228.75	1.43×10^{-3}	1.9	3.4	3.9
[260, 320)	286.25	5.56×10^{-4}	2.5	6.3	6.8
[320, 400)	356.25	1.87×10^{-4}	3.1	8.2	8.8
[400, 500)	446.25	0.56×10^{-4}	6.0	10.5	12.1
p_T^{t2} bin range [GeV]	Bin centre [GeV]	$1/\sigma d\sigma/dp_T^{t2}$ [GeV $^{-1}$]	Stat. [%]	Syst. [%]	Total [%]
[0, 60)	23.75	5.64×10^{-3}	1.4	3.2	3.5
[60, 100)	83.75	6.98×10^{-3}	1.9	1.8	2.6
[100, 150)	123.75	4.39×10^{-3}	1.7	2.6	3.1
[150, 200)	173.75	1.97×10^{-3}	2.2	3.2	3.9
[200, 260)	228.75	6.93×10^{-4}	2.8	3.3	4.3
[260, 320)	286.25	2.43×10^{-4}	4.0	4.5	6.0
[320, 400)	356.25	0.75×10^{-4}	5.3	7.3	9.0
[400, 500)	443.75	0.19×10^{-4}	11.4	11.1	16.0

Table A.9: Normalized differential $t\bar{t}$ cross section in the ℓ +jets channels as a function of top quark pair observables: the transverse momentum ($p_T^{t\bar{t}}$), the rapidity ($y_{t\bar{t}}$) and the invariant mass ($m_{t\bar{t}}$) of the $t\bar{t}$ system. The horizontally-corrected bin centres according to the MADGRAPH+PYTHIA6 prediction (cf. Section 6.2) are also provided. The results are presented at parton level in the full phase space. The statistical and systematic uncertainties are added in quadrature to yield the total uncertainty.

$p_T^{t\bar{t}}$ bin range [GeV]	Bin centre [GeV]	$1/\sigma d\sigma/dp_T^{t\bar{t}}$ [GeV $^{-1}$]	Stat. [%]	Syst. [%]	Total [%]
[0, 20)	4.50	1.32×10^{-2}	2.3	7.9	8.2
[20, 45)	32.50	1.18×10^{-2}	2.1	3.4	3.9
[45, 75)	58.50	6.40×10^{-3}	1.8	5.5	5.8
[75, 120)	95.50	2.84×10^{-3}	2.3	6.6	7.0
[120, 190)	152.50	1.07×10^{-3}	2.6	5.7	6.2
[190, 300)	237.50	3.06×10^{-4}	3.8	12.2	12.8
$y_{t\bar{t}}$ bin range	Bin centre	$1/\sigma d\sigma/dy_{t\bar{t}}$	Stat. [%]	Syst. [%]	Total [%]
[−2.5, −1.3)	−1.82	6.07×10^{-2}	3.5	2.9	4.5
[−1.3, −0.9)	−1.09	2.20×10^{-1}	1.8	2.3	3.0
[−0.9, −0.6)	−0.76	3.27×10^{-1}	1.8	2.9	3.4
[−0.6, −0.3)	−0.46	3.73×10^{-1}	1.7	1.6	2.3
[−0.3, 0.0)	−0.14	4.27×10^{-1}	1.6	1.6	2.2
[0.0, 0.3)	0.14	4.13×10^{-1}	1.6	1.9	2.4
[0.3, 0.6)	0.47	3.74×10^{-1}	1.7	1.7	2.4
[0.6, 0.9)	0.76	3.17×10^{-1}	1.8	1.7	2.5
[0.9, 1.3)	1.09	2.30×10^{-1}	1.8	2.2	2.8
[1.3, 2.5)	1.82	6.41×10^{-2}	3.3	3.8	5.1
$m_{t\bar{t}}$ bin range [GeV]	Bin centre [GeV]	$1/\sigma d\sigma/dm_{t\bar{t}}$ [GeV $^{-1}$]	Stat. [%]	Syst. [%]	Total [%]
[345, 400)	362.50	4.69×10^{-3}	2.1	7.1	7.5
[400, 470)	435.50	4.30×10^{-3}	2.1	2.9	3.6
[470, 550)	508.50	2.67×10^{-3}	2.0	6.1	6.4
[550, 650)	595.50	1.17×10^{-3}	2.3	7.3	7.7
[650, 800)	717.50	4.66×10^{-4}	2.5	4.2	4.9
[800, 1100)	927.50	1.14×10^{-4}	3.0	9.5	10.0
[1100, 1600)	1328.50	0.11×10^{-4}	8.0	9.8	12.7

Table A.10: Normalized differential $t\bar{t}$ cross section in the dilepton channels as a function of top quark or antiquark observables: the transverse momentum (p_T^t), the transverse momentum in the $t\bar{t}$ rest frame (p_T^{t*}), and the rapidity (y_t) of the top quarks or antiquarks, and the difference in the azimuthal angle between the top quark and antiquark ($\Delta\phi(t,\bar{t})$). The horizontally-corrected bin centres according to the MADGRAPH+PYTHIA6 prediction (cf. Section 6.2) are also provided. The results are presented at parton level in the full phase space. The statistical and systematic uncertainties are added in quadrature to yield the total uncertainty.

p_T^t bin range [GeV]	Bin centre [GeV]	$1/\sigma d\sigma/dp_T^t$ [GeV $^{-1}$]	Stat. [%]	Syst. [%]	Total [%]
[0, 65)	28.75	4.33×10^{-3}	1.1	2.3	2.5
[65, 125)	101.25	6.40×10^{-3}	0.9	1.4	1.7
[125, 200)	161.25	3.08×10^{-3}	1.0	2.1	2.3
[200, 290)	238.75	8.62×10^{-4}	1.3	3.6	3.8
[290, 400)	336.25	1.88×10^{-4}	2.7	7.4	7.9
p_T^{t*} bin range [GeV]	Bin centre [GeV]	$1/\sigma d\sigma/dp_T^{t*}$ [GeV $^{-1}$]	Stat. [%]	Syst. [%]	Total [%]
[0, 60)	26.25	4.45×10^{-3}	1.5	2.7	3.1
[60, 115)	93.75	6.89×10^{-3}	1.4	2.1	2.5
[115, 190)	151.25	3.41×10^{-3}	1.3	2.2	2.6
[190, 275)	226.25	8.78×10^{-4}	2.2	5.5	5.9
[275, 380)	318.75	1.87×10^{-4}	2.6	6.2	6.7
[380, 500)	428.75	2.91×10^{-5}	7.5	9.1	11.8
y_t bin range	Bin centre	$1/\sigma d\sigma/dy_t$	Stat. [%]	Syst. [%]	Total [%]
[-2.5, -1.6)	-2.01	7.63×10^{-2}	2.0	5.3	5.6
[-1.6, -1.0)	-1.31	1.97×10^{-1}	1.0	1.5	1.8
[-1.0, -0.5)	-0.76	2.82×10^{-1}	1.1	1.5	1.9
[-0.5, 0.0)	-0.29	3.35×10^{-1}	1.0	1.5	1.8
[0.0, 0.5)	0.29	3.28×10^{-1}	1.0	1.9	2.2
[0.5, 1.0)	0.76	2.85×10^{-1}	1.1	1.1	1.5
[1.0, 1.6)	1.31	2.03×10^{-1}	1.1	1.1	1.5
[1.6, 2.5)	2.01	7.40×10^{-2}	2.0	5.3	5.7
$\Delta\phi(t,\bar{t})$ bin range [rad]	Bin centre [rad]	$1/\sigma d\sigma/d\Delta\phi(t,\bar{t})$ [rad $^{-1}$]	Stat. [%]	Syst. [%]	Total [%]
[0, 1.89)	1.19	6.40×10^{-2}	2.0	7.3	7.6
[1.89, 2.77)	2.44	2.96×10^{-1}	1.0	5.6	5.7
[2.77, 3.04)	2.94	1.24	1.1	3.2	3.3
[3.04, 3.15)	3.09	2.58	1.5	7.8	8.0

Table A.11: Normalized differential $t\bar{t}$ cross section in the dilepton channels as a function of the p_T of the leading (p_T^{t1}) and trailing (p_T^{t2}) top quarks or antiquarks. The results are presented at parton level in the full phase space. The statistical and systematic uncertainties are added in quadrature to yield the total uncertainty.

p_T^{t1} bin range [GeV]	Bin centre [GeV]	$1/\sigma d\sigma/dp_T^{t1}$ [GeV $^{-1}$]	Stat. [%]	Syst. [%]	Total [%]
[0, 75)	36.25	3.31×10^{-3}	1.5	3.7	4.0
[75, 130)	111.25	6.43×10^{-3}	1.1	1.8	2.1
[130, 200)	163.75	3.67×10^{-3}	1.2	2.9	3.2
[200, 290)	241.25	1.17×10^{-3}	1.5	3.9	4.2
[290, 400)	336.25	2.61×10^{-4}	3.2	6.9	7.6
p_T^{t2} bin range [GeV]	Bin centre [GeV]	$1/\sigma d\sigma/dp_T^{t2}$ [GeV $^{-1}$]	Stat. [%]	Syst. [%]	Total [%]
[0, 55)	23.75	5.38×10^{-3}	1.7	2.2	2.8
[55, 120)	91.25	6.74×10^{-3}	1.4	1.6	2.1
[120, 200)	156.25	2.50×10^{-3}	1.7	2.1	2.7
[200, 290)	238.75	5.58×10^{-4}	2.4	4.6	5.2
[290, 400)	338.75	1.14×10^{-4}	5.1	10.2	11.4

Table A.12: Normalized differential $t\bar{t}$ cross section in the dilepton channels as a function of top quark pair observables: the transverse momentum ($p_T^{t\bar{t}}$), the rapidity ($y_{t\bar{t}}$) and the invariant mass ($m_{t\bar{t}}$) of the $t\bar{t}$ system. The results are presented at parton level in the full phase space. The statistical and systematic uncertainties are added in quadrature to yield the total uncertainty.

$p_T^{t\bar{t}}$ bin range [GeV]	Bin centre [GeV]	$1/\sigma d\sigma/dp_T^{t\bar{t}}$ [GeV $^{-1}$]	Stat. [%]	Syst. [%]	Total [%]
[0, 30)	4.50	1.43×10^{-2}	0.8	6.1	6.1
[30, 80)	51.50	6.90×10^{-3}	1.0	4.7	4.8
[80, 170)	118.50	1.91×10^{-3}	1.1	5.4	5.5
[170, 300)	223.50	3.47×10^{-4}	2.1	4.7	5.1
$y_{t\bar{t}}$ bin range	Bin centre	$1/\sigma d\sigma/dy_{t\bar{t}}$	Stat. [%]	Syst. [%]	Total [%]
[−2.5, −1.5)	−1.93	4.71×10^{-2}	4.0	6.6	7.7
[−1.5, −1.0)	−1.24	1.82×10^{-1}	1.8	1.5	2.3
[−1.0, −0.5)	−0.76	3.09×10^{-1}	1.4	1.5	2.1
[−0.5, 0.0)	−0.31	4.18×10^{-1}	1.2	1.7	2.1
[0.0, 0.5)	0.29	4.09×10^{-1}	1.2	1.2	1.7
[0.5, 1.0)	0.76	3.15×10^{-1}	1.5	1.3	2.0
[1.0, 1.5)	1.24	1.79×10^{-1}	1.8	1.8	2.6
[1.5, 2.5)	1.93	4.59×10^{-2}	4.0	6.0	7.2
$m_{t\bar{t}}$ bin range [GeV]	Bin centre [GeV]	$1/\sigma d\sigma/dm_{t\bar{t}}$ [GeV $^{-1}$]	Stat. [%]	Syst. [%]	Total [%]
[340, 380)	354.50	4.14×10^{-3}	3.0	8.6	9.1
[380, 470)	428.50	4.50×10^{-3}	1.7	5.3	5.6
[470, 620)	537.50	1.95×10^{-3}	1.8	2.9	3.4
[620, 820)	705.50	5.25×10^{-4}	2.8	3.2	4.2
[820, 1100)	940.50	1.00×10^{-4}	3.7	7.3	8.2
[1100, 1600)	1328.50	7.28×10^{-6}	14.4	28.2	31.6

B The CMS Collaboration

Yerevan Physics Institute, Yerevan, Armenia

V. Khachatryan, A.M. Sirunyan, A. Tumasyan

Institut für Hochenergiephysik der OeAW, Wien, Austria

W. Adam, T. Bergauer, M. Dragicevic, J. Erö, M. Friedl, R. Frühwirth¹, V.M. Ghete, C. Hartl, N. Hörmann, J. Hrubec, M. Jeitler¹, W. Kiesenhofer, V. Knünz, M. Krammer¹, I. Krätschmer, D. Liko, I. Mikulec, D. Rabady², B. Rahbaran, H. Rohringer, R. Schöfbeck, J. Strauss, W. Treberer-Treberspurg, W. Waltenberger, C.-E. Wulz¹

National Centre for Particle and High Energy Physics, Minsk, Belarus

V. Mossolov, N. Shumeiko, J. Suarez Gonzalez

Universiteit Antwerpen, Antwerpen, Belgium

S. Alderweireldt, M. Bansal, S. Bansal, T. Cornelis, E.A. De Wolf, X. Janssen, A. Knutsson, S. Luyckx, S. Ochesanu, R. Rougny, M. Van De Klundert, H. Van Haeevermaet, P. Van Mechelen, N. Van Remortel, A. Van Spilbeeck

Vrije Universiteit Brussel, Brussel, Belgium

F. Blekman, S. Blyweert, J. D'Hondt, N. Daci, N. Heracleous, J. Keaveney, S. Lowette, M. Maes, A. Olbrechts, Q. Python, D. Strom, S. Tavernier, W. Van Doninck, P. Van Mulders, G.P. Van Onsem, I. Vilella

Université Libre de Bruxelles, Bruxelles, Belgium

C. Caillol, B. Clerbaux, G. De Lentdecker, D. Dobur, L. Favart, A.P.R. Gay, A. Grebenyuk, A. Léonard, A. Mohammadi, L. Perniè², T. Reis, T. Seva, L. Thomas, C. Vander Velde, P. Vanlaer, J. Wang, F. Zenoni

Ghent University, Ghent, Belgium

V. Adler, K. Beernaert, L. Benucci, A. Cimmino, S. Costantini, S. Crucy, S. Dildick, A. Fagot, G. Garcia, J. Mccartin, A.A. Ocampo Rios, D. Ryckbosch, S. Salva Diblen, M. Sigamani, N. Strobbe, F. Thyssen, M. Tytgat, E. Yazgan, N. Zaganidis

Université Catholique de Louvain, Louvain-la-Neuve, Belgium

S. Basegmez, C. Beluffi³, G. Bruno, R. Castello, A. Caudron, L. Ceard, G.G. Da Silveira, C. Delaere, T. du Pree, D. Favart, L. Forthomme, A. Giammanco⁴, J. Hollar, A. Jafari, P. Jez, M. Komm, V. Lemaître, C. Nuttens, D. Pagano, L. Perrini, A. Pin, K. Piotrkowski, A. Popov⁵, L. Quertenmont, M. Selvaggi, M. Vidal Marono, J.M. Vizan Garcia

Université de Mons, Mons, Belgium

N. Bely, T. Caebergs, E. Daubie, G.H. Hammad

Centro Brasileiro de Pesquisas Físicas, Rio de Janeiro, Brazil

W.L. Aldá Júnior, G.A. Alves, L. Brito, M. Correa Martins Junior, T. Dos Reis Martins, C. Mora Herrera, M.E. Pol

Universidade do Estado do Rio de Janeiro, Rio de Janeiro, Brazil

W. Carvalho, J. Chinellato⁶, A. Custódio, E.M. Da Costa, D. De Jesus Damiao, C. De Oliveira Martins, S. Fonseca De Souza, H. Malbouisson, D. Matos Figueiredo, L. Mundim, H. Nogima, W.L. Prado Da Silva, J. Santaolalla, A. Santoro, A. Sznajder, E.J. Tonelli Manganote⁶, A. Vilela Pereira

Universidade Estadual Paulista ^a, Universidade Federal do ABC ^b, São Paulo, Brazil

C.A. Bernardes^b, S. Dogra^a, T.R. Fernandez Perez Tomei^a, E.M. Gregores^b, P.G. Mercadante^b, S.F. Novaes^a, Sandra S. Padula^a

Institute for Nuclear Research and Nuclear Energy, Sofia, Bulgaria

A. Aleksandrov, V. Genchev², P. Iaydjiev, A. Marinov, S. Piperov, M. Rodozov, G. Sultanov, M. Vutova

University of Sofia, Sofia, Bulgaria

A. Dimitrov, I. Glushkov, R. Hadjiiska, V. Kozhuharov, L. Litov, B. Pavlov, P. Petkov

Institute of High Energy Physics, Beijing, China

J.G. Bian, G.M. Chen, H.S. Chen, M. Chen, R. Du, C.H. Jiang, R. Plestina⁷, F. Romeo, J. Tao, Z. Wang

State Key Laboratory of Nuclear Physics and Technology, Peking University, Beijing, China

C. Asawatangtrakuldee, Y. Ban, Q. Li, S. Liu, Y. Mao, S.J. Qian, D. Wang, W. Zou

Universidad de Los Andes, Bogota, Colombia

C. Avila, L.F. Chaparro Sierra, C. Florez, J.P. Gomez, B. Gomez Moreno, J.C. Sanabria

University of Split, Faculty of Electrical Engineering, Mechanical Engineering and Naval Architecture, Split, Croatia

N. Godinovic, D. Lelas, D. Polic, I. Puljak

University of Split, Faculty of Science, Split, Croatia

Z. Antunovic, M. Kovac

Institute Rudjer Boskovic, Zagreb, Croatia

V. Brigljevic, K. Kadija, J. Luetic, D. Mekterovic, L. Sudic

University of Cyprus, Nicosia, Cyprus

A. Attikis, G. Mavromanolakis, J. Mousa, C. Nicolaou, F. Ptochos, P.A. Razis

Charles University, Prague, Czech Republic

M. Bodlak, M. Finger, M. Finger Jr.⁸

Academy of Scientific Research and Technology of the Arab Republic of Egypt, Egyptian Network of High Energy Physics, Cairo, Egypt

Y. Assran⁹, A. Ellithi Kamel¹⁰, M.A. Mahmoud¹¹, A. Radi^{12,13}

National Institute of Chemical Physics and Biophysics, Tallinn, Estonia

M. Kadastik, M. Murumaa, M. Raidal, A. Tiko

Department of Physics, University of Helsinki, Helsinki, Finland

P. Eerola, G. Fedi, M. Voutilainen

Helsinki Institute of Physics, Helsinki, Finland

J. Härkönen, V. Karimäki, R. Kinnunen, M.J. Kortelainen, T. Lampén, K. Lassila-Perini, S. Lehti, T. Lindén, P. Luukka, T. Mäenpää, T. Peltola, E. Tuominen, J. Tuominiemi, E. Tuovinen, L. Wendland

Lappeenranta University of Technology, Lappeenranta, Finland

J. Talvitie, T. Tuuva

DSM/IRFU, CEA/Saclay, Gif-sur-Yvette, France

M. Besancon, F. Couderc, M. Dejardin, D. Denegri, B. Fabbro, J.L. Faure, C. Favaro, F. Ferri,

S. Ganjour, A. Givernaud, P. Gras, G. Hamel de Monchenault, P. Jarry, E. Locci, J. Malcles, J. Rander, A. Rosowsky, M. Titov

Laboratoire Leprince-Ringuet, Ecole Polytechnique, IN2P3-CNRS, Palaiseau, France

S. Baffioni, F. Beaudette, P. Busson, C. Charlot, T. Dahms, M. Dalchenko, L. Dobrzynski, N. Filipovic, A. Florent, R. Granier de Cassagnac, L. Mastrolorenzo, P. Miné, C. Mironov, I.N. Naranjo, M. Nguyen, C. Ochando, P. Paganini, S. Regnard, R. Salerno, J.B. Sauvan, Y. Sirois, C. Veelken, Y. Yilmaz, A. Zabi

Institut Pluridisciplinaire Hubert Curien, Université de Strasbourg, Université de Haute Alsace Mulhouse, CNRS/IN2P3, Strasbourg, France

J.-L. Agram¹⁴, J. Andrea, A. Aubin, D. Bloch, J.-M. Brom, E.C. Chabert, C. Collard, E. Conte¹⁴, J.-C. Fontaine¹⁴, D. Gelé, U. Goerlach, C. Goetzmann, A.-C. Le Bihan, P. Van Hove

Centre de Calcul de l'Institut National de Physique Nucleaire et de Physique des Particules, CNRS/IN2P3, Villeurbanne, France

S. Gadrat

Université de Lyon, Université Claude Bernard Lyon 1, CNRS-IN2P3, Institut de Physique Nucléaire de Lyon, Villeurbanne, France

S. Beauceron, N. Beaupere, G. Boudoul², E. Bouvier, S. Brochet, C.A. Carrillo Montoya, J. Chasserat, R. Chierici, D. Contardo², P. Depasse, H. El Mamouni, J. Fan, J. Fay, S. Gascon, M. Gouzevitch, B. Ille, T. Kurca, M. Lethuillier, L. Mirabito, S. Perries, J.D. Ruiz Alvarez, D. Sabes, L. Sgandurra, V. Sordini, M. Vander Donckt, P. Verdier, S. Viret, H. Xiao

Institute of High Energy Physics and Informatization, Tbilisi State University, Tbilisi, Georgia

Z. Tsamalaidze⁸

RWTH Aachen University, I. Physikalisches Institut, Aachen, Germany

C. Autermann, S. Beranek, M. Bontenackels, M. Edelhoff, L. Feld, O. Hindrichs, K. Klein, A. Ostapchuk, A. Perieanu, F. Raupach, J. Sammet, S. Schael, H. Weber, B. Wittmer, V. Zhukov⁵

RWTH Aachen University, III. Physikalisches Institut A, Aachen, Germany

M. Ata, M. Brodski, E. Dietz-Laursonn, D. Duchardt, M. Erdmann, R. Fischer, A. Güth, T. Hebbeker, C. Heidemann, K. Hoepfner, D. Klingebiel, S. Knutzen, P. Kreuzer, M. Merschmeyer, A. Meyer, P. Millet, M. Olschewski, K. Padeken, P. Papacz, H. Reithler, S.A. Schmitz, L. Sonnenschein, D. Teyssier, S. Thüer, M. Weber

RWTH Aachen University, III. Physikalisches Institut B, Aachen, Germany

V. Cherepanov, Y. Erdogan, G. Flügge, H. Geenen, M. Geisler, W. Haj Ahmad, A. Heister, F. Hoehle, B. Kargoll, T. Kress, Y. Kuessel, A. Künsken, J. Lingemann², A. Nowack, I.M. Nugent, L. Perchalla, O. Pooth, A. Stahl

Deutsches Elektronen-Synchrotron, Hamburg, Germany

I. Asin, N. Bartosik, J. Behr, W. Behrenhoff, U. Behrens, A.J. Bell, M. Bergholz¹⁵, A. Bethani, K. Borras, A. Burgmeier, A. Cakir, L. Calligaris, A. Campbell, S. Choudhury, F. Costanza, C. Diez Pardos, S. Dooling, T. Dorland, G. Eckerlin, D. Eckstein, T. Eichhorn, G. Flucke, J. Garay Garcia, A. Geiser, P. Gunnellini, J. Hauk, M. Hempel¹⁵, D. Horton, H. Jung, A. Kalogeropoulos, M. Kasemann, P. Katsas, J. Kieseler, C. Kleinwort, D. Krücker, W. Lange, J. Leonard, K. Lipka, A. Lobanov, W. Lohmann¹⁵, B. Lutz, R. Mankel, I. Marfin¹⁵, I.-A. Melzer-Pellmann, A.B. Meyer, G. Mittag, J. Mnich, A. Mussgiller, S. Naumann-Emme, A. Nayak, O. Novgorodova, E. Ntomari, H. Perrey, D. Pitzl, R. Placakyte, A. Raspereza, P.M. Ribeiro Cipriano, B. Roland, E. Ron, M.Ö. Sahin, J. Salfeld-Nebgen, P. Saxena, R. Schmidt¹⁵,

T. Schoerner-Sadenius, M. Schröder, C. Seitz, S. Spannagel, A.D.R. Vargas Trevino, R. Walsh, C. Wissing

University of Hamburg, Hamburg, Germany

M. Aldaya Martin, V. Blobel, M. Centis Vignali, A.R. Draeger, J. Erfle, E. Garutti, K. Goebel, M. Görner, J. Haller, M. Hoffmann, R.S. Höing, H. Kirschenmann, R. Klanner, R. Kogler, J. Lange, T. Lapsien, T. Lenz, I. Marchesini, J. Ott, T. Peiffer, N. Pietsch, J. Poehlsen, T. Poehlsen, D. Rathjens, C. Sander, H. Schettler, P. Schleper, E. Schlieckau, A. Schmidt, M. Seidel, V. Sola, H. Stadie, G. Steinbrück, D. Troendle, E. Usai, L. Vanelderen, A. Vanhoefer

Institut für Experimentelle Kernphysik, Karlsruhe, Germany

C. Barth, C. Baus, J. Berger, C. Böser, E. Butz, T. Chwalek, W. De Boer, A. Descroix, A. Dierlamm, M. Feindt, F. Frensch, M. Giffels, F. Hartmann², T. Hauth², U. Husemann, I. Katkov⁵, A. Kornmayer², E. Kuznetsova, P. Lobelle Pardo, M.U. Mozer, Th. Müller, A. Nürnberg, G. Quast, K. Rabbertz, F. Ratnikov, S. Röcker, H.J. Simonis, F.M. Stober, R. Ulrich, J. Wagner-Kuhr, S. Wayand, T. Weiler, R. Wolf

Institute of Nuclear and Particle Physics (INPP), NCSR Demokritos, Aghia Paraskevi, Greece

G. Anagnostou, G. Daskalakis, T. Geralis, V.A. Giakoumopoulou, A. Kyriakis, D. Loukas, A. Markou, C. Markou, A. Psallidas, I. Topsis-Giotis

University of Athens, Athens, Greece

A. Agapitos, S. Kesisoglou, A. Panagiotou, N. Saoulidou, E. Stiliaris

University of Ioánnina, Ioánnina, Greece

X. Aslanoglou, I. Evangelou, G. Flouris, C. Foudas, P. Kokkas, N. Manthos, I. Papadopoulos, E. Paradas

Wigner Research Centre for Physics, Budapest, Hungary

G. Bencze, C. Hajdu, P. Hidas, D. Horvath¹⁶, F. Sikler, V. Veszpremi, G. Vesztergombi¹⁷, A.J. Zsigmond

Institute of Nuclear Research ATOMKI, Debrecen, Hungary

N. Beni, S. Czellar, J. Karancsi¹⁸, J. Molnar, J. Palinkas, Z. Szillasi

University of Debrecen, Debrecen, Hungary

A. Makovec, P. Raics, Z.L. Trocsanyi, B. Ujvari

National Institute of Science Education and Research, Bhubaneswar, India

S.K. Swain

Panjab University, Chandigarh, India

S.B. Beri, V. Bhatnagar, R. Gupta, U. Bhawandeep, A.K. Kalsi, M. Kaur, R. Kumar, M. Mittal, N. Nishu, J.B. Singh

University of Delhi, Delhi, India

Ashok Kumar, Arun Kumar, S. Ahuja, A. Bhardwaj, B.C. Choudhary, A. Kumar, S. Malhotra, M. Naimuddin, K. Ranjan, V. Sharma

Saha Institute of Nuclear Physics, Kolkata, India

S. Banerjee, S. Bhattacharya, K. Chatterjee, S. Dutta, B. Gomber, Sa. Jain, Sh. Jain, R. Khurana, A. Modak, S. Mukherjee, D. Roy, S. Sarkar, M. Sharan

Bhabha Atomic Research Centre, Mumbai, India

A. Abdulsalam, D. Dutta, S. Kailas, V. Kumar, A.K. Mohanty², L.M. Pant, P. Shukla, A. Topkar

Tata Institute of Fundamental Research, Mumbai, India

T. Aziz, S. Banerjee, S. Bhowmik¹⁹, R.M. Chatterjee, R.K. Dewanjee, S. Dugad, S. Ganguly, S. Ghosh, M. Guchait, A. Gurtu²⁰, G. Kole, S. Kumar, M. Maity¹⁹, G. Majumder, K. Mazumdar, G.B. Mohanty, B. Parida, K. Sudhakar, N. Wickramage²¹

Institute for Research in Fundamental Sciences (IPM), Tehran, Iran

H. Bakhshiansohi, H. Behnamian, S.M. Etesami²², A. Fahim²³, R. Goldouzian, M. Khakzad, M. Mohammadi Najafabadi, M. Naseri, S. Paktinat Mehdiabadi, F. Rezaei Hosseinabadi, B. Safarzadeh²⁴, M. Zeinali

University College Dublin, Dublin, Ireland

M. Felcini, M. Grunewald

INFN Sezione di Bari ^a, Università di Bari ^b, Politecnico di Bari ^c, Bari, Italy

M. Abbrescia^{a,b}, C. Calabria^{a,b}, S.S. Chhibra^{a,b}, A. Colaleo^a, D. Creanza^{a,c}, N. De Filippis^{a,c}, M. De Palma^{a,b}, L. Fiore^a, G. Iaselli^{a,c}, G. Maggi^{a,c}, M. Maggi^a, S. My^{a,c}, S. Nuzzo^{a,b}, A. Pompili^{a,b}, G. Pugliese^{a,c}, R. Radogna^{a,b,2}, G. Selvaggi^{a,b}, A. Sharma, L. Silvestris^{a,2}, R. Venditti^{a,b}

INFN Sezione di Bologna ^a, Università di Bologna ^b, Bologna, Italy

G. Abbiendi^a, A.C. Benvenuti^a, D. Bonacorsi^{a,b}, S. Braibant-Giacomelli^{a,b}, L. Brigliadori^{a,b}, R. Campanini^{a,b}, P. Capiluppi^{a,b}, A. Castro^{a,b}, F.R. Cavallo^a, G. Codispoti^{a,b}, M. Cuffiani^{a,b}, G.M. Dallavalle^a, F. Fabbri^a, A. Fanfani^{a,b}, D. Fasanella^{a,b}, P. Giacomelli^a, C. Grandi^a, L. Guiducci^{a,b}, S. Marcellini^a, G. Masetti^a, A. Montanari^a, F.L. Navarria^{a,b}, A. Perrotta^a, F. Primavera^{a,b}, A.M. Rossi^{a,b}, T. Rovelli^{a,b}, G.P. Siroli^{a,b}, N. Tosi^{a,b}, R. Travaglini^{a,b}

INFN Sezione di Catania ^a, Università di Catania ^b, CSFNSM ^c, Catania, Italy

S. Albergo^{a,b}, G. Cappello^a, M. Chiorboli^{a,b}, S. Costa^{a,b}, F. Giordano^{a,2}, R. Potenza^{a,b}, A. Tricomi^{a,b}, C. Tuve^{a,b}

INFN Sezione di Firenze ^a, Università di Firenze ^b, Firenze, Italy

G. Barbagli^a, V. Ciulli^{a,b}, C. Civinini^a, R. D'Alessandro^{a,b}, E. Focardi^{a,b}, E. Gallo^a, S. Gozzi^{a,b}, V. Gori^{a,b,2}, P. Lenzi^{a,b}, M. Meschini^a, S. Paoletti^a, G. Sguazzoni^a, A. Tropiano^{a,b}

INFN Laboratori Nazionali di Frascati, Frascati, Italy

L. Benussi, S. Bianco, F. Fabbri, D. Piccolo

INFN Sezione di Genova ^a, Università di Genova ^b, Genova, Italy

R. Ferretti^{a,b}, F. Ferro^a, M. Lo Vetere^{a,b}, E. Robutti^a, S. Tosi^{a,b}

INFN Sezione di Milano-Bicocca ^a, Università di Milano-Bicocca ^b, Milano, Italy

M.E. Dinardo^{a,b}, S. Fiorendi^{a,b}, S. Gennai^{a,2}, R. Gerosa^{a,b,2}, A. Ghezzi^{a,b}, P. Govoni^{a,b}, M.T. Lucchini^{a,b,2}, S. Malvezzi^a, R.A. Manzoni^{a,b}, A. Martelli^{a,b}, B. Marzocchi^{a,b}, D. Menasce^a, L. Moroni^a, M. Paganoni^{a,b}, D. Pedrini^a, S. Ragazzi^{a,b}, N. Redaelli^a, T. Tabarelli de Fatis^{a,b}

INFN Sezione di Napoli ^a, Università di Napoli 'Federico II' ^b, Napoli, Italy, Università della Basilicata ^c, Potenza, Italy, Università G. Marconi ^d, Roma, Italy

S. Buontempo^a, N. Cavallo^{a,c}, S. Di Guida^{a,d,2}, F. Fabozzi^{a,c}, A.O.M. Iorio^{a,b}, L. Lista^a, S. Meola^{a,d,2}, M. Merola^a, P. Paolucci^{a,2}

INFN Sezione di Padova ^a, Università di Padova ^b, Padova, Italy, Università di Trento ^c, Trento, Italy

P. Azzi^a, N. Bacchetta^a, D. Bisello^{a,b}, A. Branca^{a,b}, R. Carlin^{a,b}, P. Checchia^a, M. Dall'Osso^{a,b}, T. Dorigo^a, M. Galanti^{a,b}, U. Gasparini^{a,b}, P. Giubileo^{a,b}, A. Gozzelino^a, S. Lacaprara^a, M. Margoni^{a,b}, A.T. Meneguzzo^{a,b}, M. Passaseo^a, J. Pazzini^{a,b}, M. Pegoraro^a, N. Pozzobon^{a,b},

P. Ronchese^{a,b}, F. Simonetto^{a,b}, E. Torassa^a, M. Tosi^{a,b}, A. Triossi^a, P. Zotto^{a,b}, A. Zucchetta^{a,b}, G. Zumerle^{a,b}

INFN Sezione di Pavia^a, Università di Pavia^b, Pavia, Italy

M. Gabusi^{a,b}, S.P. Ratti^{a,b}, V. Re^a, C. Riccardi^{a,b}, P. Salvini^a, P. Vitulo^{a,b}

INFN Sezione di Perugia^a, Università di Perugia^b, Perugia, Italy

M. Biasini^{a,b}, G.M. Bilei^a, D. Ciangottini^{a,b}, L. Fanò^{a,b}, P. Lariccia^{a,b}, G. Mantovani^{a,b}, M. Menichelli^a, A. Saha^a, A. Santocchia^{a,b}, A. Spiezia^{a,b,2}

INFN Sezione di Pisa^a, Università di Pisa^b, Scuola Normale Superiore di Pisa^c, Pisa, Italy

K. Androsov^{a,25}, P. Azzurri^a, G. Bagliesi^a, J. Bernardini^a, T. Boccali^a, G. Broccolo^{a,c}, R. Castaldi^a, M.A. Ciocci^{a,25}, R. Dell'Orso^a, S. Donato^{a,c}, F. Fiori^{a,c}, L. Foà^{a,c}, A. Giassi^a, M.T. Grippo^{a,25}, F. Ligabue^{a,c}, T. Lomtadze^a, L. Martini^{a,b}, A. Messineo^{a,b}, C.S. Moon^{a,26}, F. Palla^{a,2}, A. Rizzi^{a,b}, A. Savoy-Navarro^{a,27}, A.T. Serban^a, P. Spagnolo^a, P. Squillacioti^{a,25}, R. Tenchini^a, G. Tonelli^{a,b}, A. Venturi^a, P.G. Verdini^a, C. Vernieri^{a,c,2}

INFN Sezione di Roma^a, Università di Roma^b, Roma, Italy

L. Barone^{a,b}, F. Cavallari^a, G. D'imperio^{a,b}, D. Del Re^{a,b}, M. Diemoz^a, C. Jorda^a, E. Longo^{a,b}, F. Margaroli^{a,b}, P. Meridiani^a, F. Micheli^{a,b,2}, S. Nourbakhsh^{a,b}, G. Organtini^{a,b}, R. Paramatti^a, S. Rahatlou^{a,b}, C. Rovelli^a, F. Santanastasio^{a,b}, L. Soffi^{a,b,2}, P. Traczyk^{a,b}

INFN Sezione di Torino^a, Università di Torino^b, Torino, Italy, Università del Piemonte Orientale^c, Novara, Italy

N. Amapane^{a,b}, R. Arcidiacono^{a,c}, S. Argiro^{a,b}, M. Arneodo^{a,c}, R. Bellan^{a,b}, C. Biino^a, N. Cartiglia^a, S. Casasso^{a,b,2}, M. Costa^{a,b}, A. Degano^{a,b}, N. Demaria^a, L. Finco^{a,b}, C. Mariotti^a, S. Maselli^a, G. Mazza^a, E. Migliore^{a,b}, V. Monaco^{a,b}, M. Musich^a, M.M. Obertino^{a,c,2}, G. Ortona^{a,b}, L. Pacher^{a,b}, N. Pastrone^a, M. Pelliccioni^a, G.L. Pinna Angioni^{a,b}, A. Potenza^{a,b}, A. Romero^{a,b}, M. Ruspa^{a,c}, R. Sacchi^{a,b}, A. Solano^{a,b}, A. Staiano^a

INFN Sezione di Trieste^a, Università di Trieste^b, Trieste, Italy

S. Belforte^a, V. Candelise^{a,b}, M. Casarsa^a, F. Cossutti^a, G. Della Ricca^{a,b}, B. Gobbo^a, C. La Licata^{a,b}, M. Marone^{a,b}, A. Schizzi^{a,b}, T. Umer^{a,b}, A. Zanetti^a

Kangwon National University, Chunchon, Korea

S. Chang, A. Kropivnitskaya, S.K. Nam

Kyungpook National University, Daegu, Korea

D.H. Kim, G.N. Kim, M.S. Kim, D.J. Kong, S. Lee, Y.D. Oh, H. Park, A. Sakharov, D.C. Son

Chonbuk National University, Jeonju, Korea

T.J. Kim

Chonnam National University, Institute for Universe and Elementary Particles, Kwangju, Korea

J.Y. Kim, S. Song

Korea University, Seoul, Korea

S. Choi, D. Gyun, B. Hong, M. Jo, H. Kim, Y. Kim, B. Lee, K.S. Lee, S.K. Park, Y. Roh

University of Seoul, Seoul, Korea

M. Choi, J.H. Kim, I.C. Park, G. Ryu, M.S. Ryu

Sungkyunkwan University, Suwon, Korea

Y. Choi, Y.K. Choi, J. Goh, D. Kim, E. Kwon, J. Lee, H. Seo, I. Yu

Vilnius University, Vilnius, Lithuania

A. Juodagalvis

National Centre for Particle Physics, Universiti Malaya, Kuala Lumpur, Malaysia

J.R. Komaragiri, M.A.B. Md Ali

Centro de Investigacion y de Estudios Avanzados del IPN, Mexico City, Mexico

E. Casimiro Linares, H. Castilla-Valdez, E. De La Cruz-Burelo, I. Heredia-de La Cruz²⁸,
A. Hernandez-Almada, R. Lopez-Fernandez, A. Sanchez-Hernandez

Universidad Iberoamericana, Mexico City, Mexico

S. Carrillo Moreno, F. Vazquez Valencia

Benemerita Universidad Autonoma de Puebla, Puebla, Mexico

I. Pedraza, H.A. Salazar Ibarguen

Universidad Autónoma de San Luis Potosí, San Luis Potosí, Mexico

A. Morelos Pineda

University of Auckland, Auckland, New Zealand

D. Krofcheck

University of Canterbury, Christchurch, New Zealand

P.H. Butler, S. Reucroft

National Centre for Physics, Quaid-I-Azam University, Islamabad, Pakistan

A. Ahmad, M. Ahmad, Q. Hassan, H.R. Hoorani, W.A. Khan, T. Khurshid, M. Shoaib

National Centre for Nuclear Research, Swierk, Poland

H. Bialkowska, M. Bluj, B. Boimska, T. Frueboes, M. Górski, M. Kazana, K. Nawrocki,
K. Romanowska-Rybinska, M. Szleper, P. Zalewski

Institute of Experimental Physics, Faculty of Physics, University of Warsaw, Warsaw, Poland

G. Brona, K. Bunkowski, M. Cwiok, W. Dominik, K. Doroba, A. Kalinowski, M. Konecki,
J. Krolikowski, M. Misiura, M. Olszewski, W. Wolszczak

Laboratório de Instrumentação e Física Experimental de Partículas, Lisboa, Portugal

P. Bargassa, C. Beirão Da Cruz E Silva, P. Faccioli, P.G. Ferreira Parracho, M. Gallinaro, L. Lloret
Iglesias, F. Nguyen, J. Rodrigues Antunes, J. Seixas, J. Varela, P. Vischia

Joint Institute for Nuclear Research, Dubna, Russia

P. Bunin, M. Gavrilenko, I. Golutvin, A. Kamenev, V. Karjavin, V. Konoplyanikov, V. Korenkov,
A. Lanev, A. Malakhov, V. Matveev²⁹, V.V. Mitsyn, P. Moisezenz, V. Palichik, V. Perelygin,
S. Shmatov, V. Smirnov, E. Tikhonenko, A. Zarubin

Petersburg Nuclear Physics Institute, Gatchina (St. Petersburg), Russia

V. Golovtsov, Y. Ivanov, V. Kim³⁰, P. Levchenko, V. Murzin, V. Oreshkin, I. Smirnov, V. Sulimov,
L. Uvarov, S. Vavilov, A. Vorobyev, An. Vorobyev

Institute for Nuclear Research, Moscow, Russia

Yu. Andreev, A. Dermenev, S. Gninenko, N. Golubev, M. Kirsanov, N. Krasnikov, A. Pashenkov,
D. Tlisov, A. Toropin

Institute for Theoretical and Experimental Physics, Moscow, Russia

V. Epshteyn, V. Gavrilov, N. Lychkovskaya, V. Popov, I. Pozdnyakov, G. Safronov, S. Semenov,
A. Spiridonov, V. Stolin, E. Vlasov, A. Zhokin

P.N. Lebedev Physical Institute, Moscow, Russia

V. Andreev, M. Azarkin, I. Dremin, M. Kirakosyan, A. Leonidov, G. Mesyats, S.V. Rusakov, A. Vinogradov

Skobeltsyn Institute of Nuclear Physics, Lomonosov Moscow State University, Moscow, Russia

A. Belyaev, E. Boos, V. Bunichev, M. Dubinin³¹, L. Dudko, A. Ershov, A. Gribushin, V. Klyukhin, I. Lokhtin, S. Obraztsov, M. Perfilov, S. Petrushanko, V. Savrin

State Research Center of Russian Federation, Institute for High Energy Physics, Protvino, Russia

I. Azhgirey, I. Bayshev, S. Bitioukov, V. Kachanov, A. Kalinin, D. Konstantinov, V. Krychkin, V. Petrov, R. Ryutin, A. Sobol, L. Tourtchanovitch, S. Troshin, N. Tyurin, A. Uzunian, A. Volkov

University of Belgrade, Faculty of Physics and Vinca Institute of Nuclear Sciences, Belgrade, Serbia

P. Adzic³², M. Ekmedzic, J. Milosevic, V. Rekovic

Centro de Investigaciones Energéticas Medioambientales y Tecnológicas (CIEMAT), Madrid, Spain

J. Alcaraz Maestre, C. Battilana, E. Calvo, M. Cerrada, M. Chamizo Llatas, N. Colino, B. De La Cruz, A. Delgado Peris, D. Domínguez Vázquez, A. Escalante Del Valle, C. Fernandez Bedoya, J.P. Fernández Ramos, J. Flix, M.C. Fouz, P. Garcia-Abia, O. Gonzalez Lopez, S. Goy Lopez, J.M. Hernandez, M.I. Josa, E. Navarro De Martino, A. Pérez-Calero Yzquierdo, J. Puerta Pelayo, A. Quintario Olmeda, I. Redondo, L. Romero, M.S. Soares

Universidad Autónoma de Madrid, Madrid, Spain

C. Albajar, J.F. de Trocóniz, M. Missiroli, D. Moran

Universidad de Oviedo, Oviedo, Spain

H. Brun, J. Cuevas, J. Fernandez Menendez, S. Folgueras, I. Gonzalez Caballero

Instituto de Física de Cantabria (IFCA), CSIC-Universidad de Cantabria, Santander, Spain

J.A. Brochero Cifuentes, I.J. Cabrillo, A. Calderon, J. Duarte Campderros, M. Fernandez, G. Gomez, A. Graziano, A. Lopez Virto, J. Marco, R. Marco, C. Martinez Rivero, F. Matorras, F.J. Munoz Sanchez, J. Piedra Gomez, T. Rodrigo, A.Y. Rodríguez-Marrero, A. Ruiz-Jimeno, L. Scodellaro, I. Vila, R. Vilar Cortabitarte

CERN, European Organization for Nuclear Research, Geneva, Switzerland

D. Abbaneo, E. Auffray, G. Auzinger, M. Bachtis, P. Baillon, A.H. Ball, D. Barney, A. Benaglia, J. Bendavid, L. Benhabib, J.F. Benitez, C. Bernet⁷, G. Bianchi, P. Bloch, A. Bocci, A. Bonato, O. Bondu, C. Botta, H. Breuker, T. Camporesi, G. Cerminara, S. Colafranceschi³³, M. D'Alfonso, D. d'Enterria, A. Dabrowski, A. David, F. De Guio, A. De Roeck, S. De Visscher, E. Di Marco, M. Dobson, M. Dordevic, B. Dorney, N. Dupont-Sagorin, A. Elliott-Peisert, J. Eugster, G. Franzoni, W. Funk, D. Gigi, K. Gill, D. Giordano, M. Girone, F. Glege, R. Guida, S. Gundacker, M. Guthoff, J. Hammer, M. Hansen, P. Harris, J. Hegeman, V. Innocente, P. Janot, K. Kousouris, K. Krajczar, P. Lecoq, C. Lourenço, N. Magini, L. Malgeri, M. Mannelli, J. Marrouche, L. Masetti, F. Meijers, S. Mersi, E. Meschi, F. Moortgat, S. Morovic, M. Mulders, P. Musella, L. Orsini, L. Pape, E. Perez, L. Perrozzi, A. Petrilli, G. Petrucciani, A. Pfeiffer, M. Pierini, M. Pimiä, D. Piparo, M. Plagge, A. Racz, G. Rolandi³⁴, M. Rovere, H. Sakulin, C. Schäfer, C. Schwick, A. Sharma, P. Siegrist, P. Silva, M. Simon, P. Sphicas³⁵, D. Spiga, J. Steggemann, B. Stieger, M. Stoye, Y. Takahashi, D. Treille, A. Tsiros, G.I. Veres¹⁷, N. Wardle, H.K. Wöhri, H. Wollny, W.D. Zeuner

Paul Scherrer Institut, Villigen, Switzerland

W. Bertl, K. Deiters, W. Erdmann, R. Horisberger, Q. Ingram, H.C. Kaestli, D. Kotlinski, U. Langenegger, D. Renker, T. Rohe

Institute for Particle Physics, ETH Zurich, Zurich, Switzerland

F. Bachmair, L. Bäni, L. Bianchini, M.A. Buchmann, B. Casal, N. Chanon, G. Dissertori, M. Dittmar, M. Donegà, M. Dünser, P. Eller, C. Grab, D. Hits, J. Hoss, W. Luster, M. Mangano, A.C. Marini, P. Martinez Ruiz del Arbol, M. Masciovecchio, D. Meister, N. Mohr, C. Nägeli³⁶, F. Nessi-Tedaldi, F. Pandolfi, F. Pauss, M. Peruzzi, M. Quittnat, L. Rebane, M. Rossini, A. Starodumov³⁷, M. Takahashi, K. Theofilatos, R. Wallny, H.A. Weber

Universität Zürich, Zurich, Switzerland

C. Amsler³⁸, M.F. Canelli, V. Chiochia, A. De Cosa, A. Hinzmann, T. Hreus, B. Kilminster, C. Lange, B. Millan Mejias, J. Ngadiuba, P. Robmann, F.J. Ronga, S. Taroni, M. Verzetti, Y. Yang

National Central University, Chung-Li, Taiwan

M. Cardaci, K.H. Chen, C. Ferro, C.M. Kuo, W. Lin, Y.J. Lu, R. Volpe, S.S. Yu

National Taiwan University (NTU), Taipei, Taiwan

P. Chang, Y.H. Chang, Y.W. Chang, Y. Chao, K.F. Chen, P.H. Chen, C. Dietz, U. Grundler, W.-S. Hou, K.Y. Kao, Y.J. Lei, Y.F. Liu, R.-S. Lu, D. Majumder, E. Petrakou, Y.M. Tzeng, R. Wilken

Chulalongkorn University, Faculty of Science, Department of Physics, Bangkok, Thailand

B. Asavapibhop, G. Singh, N. Srimanobhas, N. Suwonjandee

Cukurova University, Adana, Turkey

A. Adiguzel, M.N. Bakirci³⁹, S. Cerci⁴⁰, C. Dozen, I. Dumanoglu, E. Eskut, S. Girgis, G. Gokbulut, E. Gurpinar, I. Hos, E.E. Kangal, A. Kayis Topaksu, G. Onengut⁴¹, K. Ozdemir, S. Ozturk³⁹, A. Polatoz, D. Sunar Cerci⁴⁰, B. Tali⁴⁰, H. Topakli³⁹, M. Vergili

Middle East Technical University, Physics Department, Ankara, Turkey

I.V. Akin, B. Bilin, S. Bilmis, H. Gamsizkan⁴², B. Isildak⁴³, G. Karapinar⁴⁴, K. Ocalan⁴⁵, S. Sekmen, U.E. Surat, M. Yalvac, M. Zeyrek

Bogazici University, Istanbul, Turkey

E.A. Albayrak⁴⁶, E. Gülmez, M. Kaya⁴⁷, O. Kaya⁴⁸, T. Yetkin⁴⁹

Istanbul Technical University, Istanbul, Turkey

K. Cankocak, F.I. Vardarli

National Scientific Center, Kharkov Institute of Physics and Technology, Kharkov, Ukraine

L. Levchuk, P. Sorokin

University of Bristol, Bristol, United Kingdom

J.J. Brooke, E. Clement, D. Cussans, H. Flacher, J. Goldstein, M. Grimes, G.P. Heath, H.F. Heath, J. Jacob, L. Kreczko, C. Lucas, Z. Meng, D.M. Newbold⁵⁰, S. Paramesvaran, A. Poll, T. Sakuma, S. Senkin, V.J. Smith, T. Williams

Rutherford Appleton Laboratory, Didcot, United Kingdom

K.W. Bell, A. Belyaev⁵¹, C. Brew, R.M. Brown, D.J.A. Cockerill, J.A. Coughlan, K. Harder, S. Harper, E. Olaiya, D. Petyt, C.H. Shepherd-Themistocleous, A. Thea, I.R. Tomalin, W.J. Womersley, S.D. Worm

Imperial College, London, United Kingdom

M. Baber, R. Bainbridge, O. Buchmuller, D. Burton, D. Colling, N. Cripps, M. Cutajar, P. Dauncey, G. Davies, M. Della Negra, P. Dunne, W. Ferguson, J. Fulcher, D. Futyan, A. Gilbert,

G. Hall, G. Iles, M. Jarvis, G. Karapostoli, M. Kenzie, R. Lane, R. Lucas⁵⁰, L. Lyons, A.-M. Magnan, S. Malik, B. Mathias, J. Nash, A. Nikitenko³⁷, J. Pela, M. Pesaresi, K. Petridis, D.M. Raymond, S. Rogerson, A. Rose, C. Seez, P. Sharp[†], A. Tapper, M. Vazquez Acosta, T. Virdee, S.C. Zenz

Brunel University, Uxbridge, United Kingdom

J.E. Cole, P.R. Hobson, A. Khan, P. Kyberd, D. Leggat, D. Leslie, W. Martin, I.D. Reid, P. Symonds, L. Teodorescu, M. Turner

Baylor University, Waco, USA

J. Dittmann, K. Hatakeyama, A. Kasmi, H. Liu, T. Scarborough

The University of Alabama, Tuscaloosa, USA

O. Charaf, S.I. Cooper, C. Henderson, P. Rumerio

Boston University, Boston, USA

A. Avetisyan, T. Bose, C. Fantasia, P. Lawson, C. Richardson, J. Rohlf, J. St. John, L. Sulak

Brown University, Providence, USA

J. Alimena, E. Berry, S. Bhattacharya, G. Christopher, D. Cutts, Z. Demiragli, N. Dhingra, A. Ferapontov, A. Garabedian, U. Heintz, G. Kukartsev, E. Laird, G. Landsberg, M. Luk, M. Narain, M. Segala, T. Sinthuprasith, T. Speer, J. Swanson

University of California, Davis, Davis, USA

R. Breedon, G. Breto, M. Calderon De La Barca Sanchez, S. Chauhan, M. Chertok, J. Conway, R. Conway, P.T. Cox, R. Erbacher, M. Gardner, W. Ko, R. Lander, T. Miceli, M. Mulhearn, D. Pellett, J. Pilot, F. Ricci-Tam, M. Searle, S. Shalhout, J. Smith, M. Squires, D. Stolp, M. Tripathi, S. Wilbur, R. Yohay

University of California, Los Angeles, USA

R. Cousins, P. Everaerts, C. Farrell, J. Hauser, M. Ignatenko, G. Rakness, E. Takasugi, V. Valuev, M. Weber

University of California, Riverside, Riverside, USA

K. Burt, R. Clare, J. Ellison, J.W. Gary, G. Hanson, J. Heilman, M. Ivova Rikova, P. Jandir, E. Kennedy, F. Lacroix, O.R. Long, A. Luthra, M. Malberti, M. Olmedo Negrete, A. Shrinivas, S. Sumowidagdo, S. Wimpenny

University of California, San Diego, La Jolla, USA

J.G. Branson, G.B. Cerati, S. Cittolin, R.T. D'Agnolo, A. Holzner, R. Kelley, D. Klein, J. Letts, I. Macneill, D. Olivito, S. Padhi, C. Palmer, M. Pieri, M. Sani, V. Sharma, S. Simon, E. Sudano, M. Tadel, Y. Tu, A. Vartak, C. Welke, F. Würthwein, A. Yagil

University of California, Santa Barbara, Santa Barbara, USA

D. Barge, J. Bradmiller-Feld, C. Campagnari, T. Danielson, A. Dishaw, V. Dutta, K. Flowers, M. Franco Sevilla, P. Geffert, C. George, F. Golf, L. Gouskos, J. Incandela, C. Justus, N. Mccoll, J. Richman, D. Stuart, W. To, C. West, J. Yoo

California Institute of Technology, Pasadena, USA

A. Apresyan, A. Bornheim, J. Bunn, Y. Chen, J. Duarte, A. Mott, H.B. Newman, C. Pena, C. Rogan, M. Spiropulu, V. Timciuc, J.R. Vlimant, R. Wilkinson, S. Xie, R.Y. Zhu

Carnegie Mellon University, Pittsburgh, USA

V. Azzolini, A. Calamba, B. Carlson, T. Ferguson, Y. Iiyama, M. Paulini, J. Russ, H. Vogel, I. Vorobiev

University of Colorado at Boulder, Boulder, USA

J.P. Cumalat, W.T. Ford, A. Gaz, M. Krohn, E. Luiggi Lopez, U. Nauenberg, J.G. Smith, K. Stenson, K.A. Ulmer, S.R. Wagner

Cornell University, Ithaca, USA

J. Alexander, A. Chatterjee, J. Chaves, J. Chu, S. Dittmer, N. Eggert, N. Mirman, G. Nicolas Kaufman, J.R. Patterson, A. Ryd, E. Salvati, L. Skinnari, W. Sun, W.D. Teo, J. Thom, J. Thompson, J. Tucker, Y. Weng, L. Winstrom, P. Wittich

Fairfield University, Fairfield, USA

D. Winn

Fermi National Accelerator Laboratory, Batavia, USA

S. Abdullin, M. Albrow, J. Anderson, G. Apollinari, L.A.T. Bauerdick, A. Beretvas, J. Berryhill, P.C. Bhat, G. Bolla, K. Burkett, J.N. Butler, H.W.K. Cheung, F. Chlebana, S. Cihangir, V.D. Elvira, I. Fisk, J. Freeman, Y. Gao, E. Gottschalk, L. Gray, D. Green, S. Grünendahl, O. Gutsche, J. Hanlon, D. Hare, R.M. Harris, J. Hirschauer, B. Hooberman, S. Jindariani, M. Johnson, U. Joshi, K. Kaadze, B. Klima, B. Kreis, S. Kwan, J. Linacre, D. Lincoln, R. Lipton, T. Liu, J. Lykken, K. Maeshima, J.M. Marraffino, V.I. Martinez Outschoorn, S. Maruyama, D. Mason, P. McBride, P. Merkel, K. Mishra, S. Mrenna, Y. Musienko²⁹, S. Nahn, C. Newman-Holmes, V. O'Dell, O. Prokofyev, E. Sexton-Kennedy, S. Sharma, A. Soha, W.J. Spalding, L. Spiegel, L. Taylor, S. Tkaczyk, N.V. Tran, L. Uplegger, E.W. Vaandering, R. Vidal, A. Whitbeck, J. Whitmore, F. Yang

University of Florida, Gainesville, USA

D. Acosta, P. Avery, P. Bortignon, D. Bourilkov, M. Carver, T. Cheng, D. Curry, S. Das, M. De Gruttola, G.P. Di Giovanni, R.D. Field, M. Fisher, I.K. Furic, J. Hugon, J. Konigsberg, A. Korytov, T. Kypreos, J.F. Low, K. Matchev, P. Milenov⁵², G. Mitselmakher, L. Muniz, A. Rinkevicius, L. Shchutska, M. Snowball, D. Sperka, J. Yelton, M. Zakaria

Florida International University, Miami, USA

S. Hewamanage, S. Linn, P. Markowitz, G. Martinez, J.L. Rodriguez

Florida State University, Tallahassee, USA

T. Adams, A. Askew, J. Bochenek, B. Diamond, J. Haas, S. Hagopian, V. Hagopian, K.F. Johnson, H. Prosper, V. Veeraraghavan, M. Weinberg

Florida Institute of Technology, Melbourne, USA

M.M. Baarmand, M. Hohlmann, H. Kalakhety, F. Yumiceva

University of Illinois at Chicago (UIC), Chicago, USA

M.R. Adams, L. Apanasevich, V.E. Bazterra, D. Berry, R.R. Betts, I. Bucinskaite, R. Cavanaugh, O. Evdokimov, L. Gauthier, C.E. Gerber, D.J. Hofman, S. Khalatyan, P. Kurt, D.H. Moon, C. O'Brien, C. Silkworth, P. Turner, N. Varelas

The University of Iowa, Iowa City, USA

B. Bilki⁵³, W. Clarida, K. Dilsiz, F. Duru, M. Haytmyradov, J.-P. Merlo, H. Mermerkaya⁵⁴, A. Mestvirishvili, A. Moeller, J. Nachtman, H. Ogul, Y. Onel, F. Ozok⁴⁶, A. Penzo, R. Rahmat, S. Sen, P. Tan, E. Tiras, J. Wetzel, K. Yi

Johns Hopkins University, Baltimore, USA

B.A. Barnett, B. Blumenfeld, S. Bolognesi, D. Fehling, A.V. Gritsan, P. Maksimovic, C. Martin, M. Swartz

The University of Kansas, Lawrence, USA

P. Baringer, A. Bean, G. Benelli, C. Bruner, R.P. Kenny III, M. Malek, M. Murray, D. Noonan, S. Sanders, J. Sekaric, R. Stringer, Q. Wang, J.S. Wood

Kansas State University, Manhattan, USA

I. Chakaberia, A. Ivanov, S. Khalil, M. Makouski, Y. Maravin, L.K. Saini, S. Shrestha, N. Skhirtladze, I. Svintradze

Lawrence Livermore National Laboratory, Livermore, USA

J. Gronberg, D. Lange, F. Rebassoo, D. Wright

University of Maryland, College Park, USA

A. Baden, A. Belloni, B. Calvert, S.C. Eno, J.A. Gomez, N.J. Hadley, R.G. Kellogg, T. Kolberg, Y. Lu, M. Marionneau, A.C. Mignerey, K. Pedro, A. Skuja, M.B. Tonjes, S.C. Tonwar

Massachusetts Institute of Technology, Cambridge, USA

A. Apyan, R. Barbieri, G. Bauer, W. Busza, I.A. Cali, M. Chan, L. Di Matteo, G. Gomez Ceballos, M. Goncharov, D. Gulhan, M. Klute, Y.S. Lai, Y.-J. Lee, A. Levin, P.D. Luckey, T. Ma, C. Paus, D. Ralph, C. Roland, G. Roland, G.S.F. Stephans, F. Stöckli, K. Sumorok, D. Velicanu, J. Veverka, B. Wyslouch, M. Yang, M. Zanetti, V. Zhukova

University of Minnesota, Minneapolis, USA

B. Dahmes, A. Gude, S.C. Kao, K. Klapoetke, Y. Kubota, J. Mans, N. Pastika, R. Rusack, A. Singovsky, N. Tambe, J. Turkewitz

University of Mississippi, Oxford, USA

J.G. Acosta, S. Oliveros

University of Nebraska-Lincoln, Lincoln, USA

E. Avdeeva, K. Bloom, S. Bose, D.R. Claes, A. Dominguez, R. Gonzalez Suarez, J. Keller, D. Knowlton, I. Kravchenko, J. Lazo-Flores, S. Malik, F. Meier, G.R. Snow, M. Zvada

State University of New York at Buffalo, Buffalo, USA

J. Dolen, A. Godshalk, I. Iashvili, A. Kharchilava, A. Kumar, S. Rappoccio

Northeastern University, Boston, USA

G. Alverson, E. Barberis, D. Baumgartel, M. Chasco, J. Haley, A. Massironi, D.M. Morse, D. Nash, T. Orimoto, D. Trocino, R.-J. Wang, D. Wood, J. Zhang

Northwestern University, Evanston, USA

K.A. Hahn, A. Kubik, N. Mucia, N. Odell, B. Pollack, A. Pozdnyakov, M. Schmitt, S. Stoynev, K. Sung, M. Velasco, S. Won

University of Notre Dame, Notre Dame, USA

A. Brinkerhoff, K.M. Chan, A. Drozdetskiy, M. Hildreth, C. Jessop, D.J. Karmgard, N. Kellams, K. Lannon, W. Luo, S. Lynch, N. Marinelli, T. Pearson, M. Planer, R. Ruchti, N. Valls, M. Wayne, M. Wolf, A. Woodard

The Ohio State University, Columbus, USA

L. Antonelli, J. Brinson, B. Bylsma, L.S. Durkin, S. Flowers, A. Hart, C. Hill, R. Hughes, K. Kotov, T.Y. Ling, D. Puigh, M. Rodenburg, G. Smith, B.L. Winer, H. Wolfe, H.W. Wulsin

Princeton University, Princeton, USA

O. Driga, P. Elmer, J. Hardenbrook, P. Hebda, A. Hunt, S.A. Koay, P. Lujan, D. Marlow, T. Medvedeva, M. Mooney, J. Olsen, P. Piroué, X. Quan, H. Saka, D. Stickland², C. Tully, J.S. Werner, A. Zuranski

University of Puerto Rico, Mayaguez, USA

E. Brownson, H. Mendez, J.E. Ramirez Vargas

Purdue University, West Lafayette, USA

V.E. Barnes, D. Benedetti, D. Bortoletto, M. De Mattia, L. Gutay, Z. Hu, M.K. Jha, M. Jones, K. Jung, M. Kress, N. Leonardo, D. Lopes Pegna, V. Maroussov, D.H. Miller, N. Neumeister, B.C. Radburn-Smith, X. Shi, I. Shipsey, D. Silvers, A. Svyatkovskiy, F. Wang, W. Xie, L. Xu, H.D. Yoo, J. Zablocki, Y. Zheng

Purdue University Calumet, Hammond, USA

N. Parashar, J. Stupak

Rice University, Houston, USA

A. Adair, B. Akgun, K.M. Ecklund, F.J.M. Geurts, W. Li, B. Michlin, B.P. Padley, R. Redjimi, J. Roberts, J. Zabel

University of Rochester, Rochester, USA

B. Betchart, A. Bodek, R. Covarelli, P. de Barbaro, R. Demina, Y. Eshaq, T. Ferbel, A. Garcia-Bellido, P. Goldenzweig, J. Han, A. Harel, A. Khukhunaishvili, S. Korjenevski, G. Petrillo, D. Vishnevskiy

The Rockefeller University, New York, USA

R. Ciesielski, L. Demortier, K. Goulianos, G. Lungu, C. Mesropian

Rutgers, The State University of New Jersey, Piscataway, USA

S. Arora, A. Barker, J.P. Chou, C. Contreras-Campana, E. Contreras-Campana, D. Duggan, D. Ferencek, Y. Gershtein, R. Gray, E. Halkiadakis, D. Hidas, S. Kaplan, A. Lath, S. Panwalkar, M. Park, R. Patel, S. Salur, S. Schnetzer, S. Somalwar, R. Stone, S. Thomas, P. Thomassen, M. Walker

University of Tennessee, Knoxville, USA

K. Rose, S. Spanier, A. York

Texas A&M University, College Station, USA

O. Bouhali⁵⁵, A. Castaneda Hernandez, R. Eusebi, W. Flanagan, J. Gilmore, T. Kamon⁵⁶, V. Khotilovich, V. Krutelyov, R. Montalvo, I. Osipenkov, Y. Pakhotin, A. Perloff, J. Roe, A. Rose, A. Safonov, I. Suarez, A. Tatarinov

Texas Tech University, Lubbock, USA

N. Akchurin, C. Cowden, J. Damgov, C. Dragoiu, P.R. Duderu, J. Faulkner, K. Kovitanggoon, S. Kunori, S.W. Lee, T. Libeiro, I. Volobouev

Vanderbilt University, Nashville, USA

E. Appelt, A.G. Delannoy, S. Greene, A. Gurrola, W. Johns, C. Maguire, Y. Mao, A. Melo, M. Sharma, P. Sheldon, B. Snook, S. Tuo, J. Velkovska

University of Virginia, Charlottesville, USA

M.W. Arenton, S. Boutle, B. Cox, B. Francis, J. Goodell, R. Hirosky, A. Ledovskoy, H. Li, C. Lin, C. Neu, J. Wood

Wayne State University, Detroit, USA

C. Clarke, R. Harr, P.E. Karchin, C. Kottachchi Kankanamge Don, P. Lamichhane, J. Sturdy

University of Wisconsin, Madison, USA

D.A. Belknap, D. Carlsmith, M. Cepeda, S. Dasu, L. Dodd, S. Duric, E. Friis, R. Hall-Wilton, M. Herndon, A. Hervé, P. Klabbers, A. Lanaro, C. Lazaridis, A. Levine, R. Loveless,

A. Mohapatra, I. Ojalvo, T. Perry, G.A. Pierro, G. Polese, I. Ross, T. Sarangi, A. Savin, W.H. Smith, D. Taylor, P. Verwilligen, C. Vuosalo, N. Woods

†: Deceased

- 1: Also at Vienna University of Technology, Vienna, Austria
- 2: Also at CERN, European Organization for Nuclear Research, Geneva, Switzerland
- 3: Also at Institut Pluridisciplinaire Hubert Curien, Université de Strasbourg, Université de Haute Alsace Mulhouse, CNRS/IN2P3, Strasbourg, France
- 4: Also at National Institute of Chemical Physics and Biophysics, Tallinn, Estonia
- 5: Also at Skobeltsyn Institute of Nuclear Physics, Lomonosov Moscow State University, Moscow, Russia
- 6: Also at Universidade Estadual de Campinas, Campinas, Brazil
- 7: Also at Laboratoire Leprince-Ringuet, Ecole Polytechnique, IN2P3-CNRS, Palaiseau, France
- 8: Also at Joint Institute for Nuclear Research, Dubna, Russia
- 9: Also at Suez University, Suez, Egypt
- 10: Also at Cairo University, Cairo, Egypt
- 11: Also at Fayoum University, El-Fayoum, Egypt
- 12: Also at British University in Egypt, Cairo, Egypt
- 13: Now at Ain Shams University, Cairo, Egypt
- 14: Also at Université de Haute Alsace, Mulhouse, France
- 15: Also at Brandenburg University of Technology, Cottbus, Germany
- 16: Also at Institute of Nuclear Research ATOMKI, Debrecen, Hungary
- 17: Also at Eötvös Loránd University, Budapest, Hungary
- 18: Also at University of Debrecen, Debrecen, Hungary
- 19: Also at University of Visva-Bharati, Santiniketan, India
- 20: Now at King Abdulaziz University, Jeddah, Saudi Arabia
- 21: Also at University of Ruhuna, Matara, Sri Lanka
- 22: Also at Isfahan University of Technology, Isfahan, Iran
- 23: Also at University of Tehran, Department of Engineering Science, Tehran, Iran
- 24: Also at Plasma Physics Research Center, Science and Research Branch, Islamic Azad University, Tehran, Iran
- 25: Also at Università degli Studi di Siena, Siena, Italy
- 26: Also at Centre National de la Recherche Scientifique (CNRS) - IN2P3, Paris, France
- 27: Also at Purdue University, West Lafayette, USA
- 28: Also at Universidad Michoacana de San Nicolas de Hidalgo, Morelia, Mexico
- 29: Also at Institute for Nuclear Research, Moscow, Russia
- 30: Also at St. Petersburg State Polytechnical University, St. Petersburg, Russia
- 31: Also at California Institute of Technology, Pasadena, USA
- 32: Also at Faculty of Physics, University of Belgrade, Belgrade, Serbia
- 33: Also at Facoltà Ingegneria, Università di Roma, Roma, Italy
- 34: Also at Scuola Normale e Sezione dell'INFN, Pisa, Italy
- 35: Also at University of Athens, Athens, Greece
- 36: Also at Paul Scherrer Institut, Villigen, Switzerland
- 37: Also at Institute for Theoretical and Experimental Physics, Moscow, Russia
- 38: Also at Albert Einstein Center for Fundamental Physics, Bern, Switzerland
- 39: Also at Gaziosmanpasa University, Tokat, Turkey
- 40: Also at Adiyaman University, Adiyaman, Turkey
- 41: Also at Cag University, Mersin, Turkey
- 42: Also at Anadolu University, Eskisehir, Turkey
- 43: Also at Ozyegin University, Istanbul, Turkey

- 44: Also at Izmir Institute of Technology, Izmir, Turkey
- 45: Also at Necmettin Erbakan University, Konya, Turkey
- 46: Also at Mimar Sinan University, Istanbul, Istanbul, Turkey
- 47: Also at Marmara University, Istanbul, Turkey
- 48: Also at Kafkas University, Kars, Turkey
- 49: Also at Yildiz Technical University, Istanbul, Turkey
- 50: Also at Rutherford Appleton Laboratory, Didcot, United Kingdom
- 51: Also at School of Physics and Astronomy, University of Southampton, Southampton, United Kingdom
- 52: Also at University of Belgrade, Faculty of Physics and Vinca Institute of Nuclear Sciences, Belgrade, Serbia
- 53: Also at Argonne National Laboratory, Argonne, USA
- 54: Also at Erzincan University, Erzincan, Turkey
- 55: Also at Texas A&M University at Qatar, Doha, Qatar
- 56: Also at Kyungpook National University, Daegu, Korea